Queensland University of Technology

Verification of Patient Position during Intensity Modulated Radiotherapy by Electronic Portal Imaging Devices Using Monte Carlo Techniques

Moh'd Abdelqader Al-Roumi

Submitted to the Science and Engineering Faculty, Queensland University of Technology, in fulfilment of the requirements for the degree of Masters

Science and Engineering Faculty

Queensland University of Technology

2018

Keywords

Radiotherapy

EPID

Monte Carlo

IMRT

Calibration of IMRT images

Position verification

Geometric accuracy

Set-up errors

EGSnrc

BEAMnrc

DOSXYZnrc

Linac modelling

Calibration Phantom

Abstract

Intensity modulated radiotherapy (IMRT) has in recent years become the standard of care for radiotherapy treatments. The high precision of IMRT delivery makes patient set-up accuracy more important than for past procedures. The complexity of delivery techniques and large dose gradients around the target volume make the verification process of patient treatment crucial to the success of treatment. Verification procedures involve imaging the patient prior to treatment to compare the patient set-up with the planned set-up (or reference position) to ensure the maximum coverage of the target volume. The non-uniform intensities of the intensity-modulated beams create a "mask" that hides the patient's anatomy in electronic portal images (EPI) acquired during the delivery of these beams. This imaging difficulty during IMRT is the main concern of this study investigation.

With IMRT treatment it is currently possible to image the patient pre- and post-treatment but not during the treatment field delivery due to the modulations in the fields that mask the patient's anatomy. Previous studies have indicated methods of calibration to remove these intensity modulations. The studies showed that the calibration of images is feasible for measured IMRT portal images, but there were no reference images to compare these results with except the 'day-one' measured reference image that was assumed to be correct. They recommended the comparison of those images with MC reference image to assess the systematic set-up errors of the patient set-up during the treatment course. This study focuses on generating Monte Carlo (MC) IMRT portal images to be used as reference images (after calibration) in the verification process of patient set-up errors during IMRT treatment. Additionally, a proposed imaging procedure to be developed to estimate the set-up errors during IMRT treatment using the calibrated portal images measured and simulated (reference image).

The initial stage of this study investigated the ability of MC code to simulate a simple IMRT field using square fields (5×5, 10×10, 15×15, 20×20, and 25×25 cm^2). The study then developed a simulation of a clinical IMRT field (prostate) and demonstrated the feasibility of simulating these simple and clinical IMRT field using a step-and-shoot delivery technique. A model lung phantom was designed

($30\times30\times40$ cm^3) and simulated, and the image was calculated using DOSXYZnrc. The simulated IMRT EPID images were calculated in a detector at the Gadox screen layer. These images were calibrated using a simple division method, which showed that it was feasible to calibrate simulated images of the simple and clinical IMRT EPID images. The modulations were removed successfully from the simulated IMRT EPID images, and the lung anatomy was visible in these calibrated images.

The study has been extended further to investigate and implement the simulation procedures and calibration method for more patient-like geometry and IMRT treatments plans with multiple fields. The calibration method was applied to both measured and simulated IMRT EPID images (Chapter 5). iView software was used to verify the phantom position and detect any residual errors in the phantom position in the measured images with respect to the MC calibrated IMRT EPID images (reference image). This stage involved five studies (A, B, C, D, and E) using clinical IMRT fields with a number of different humanoid and calibration phantoms. The calibration phantoms in the measurements were slab geometry of a uniform density material (i.e. PMMA, Plastic Water). The calibration phantom in the simulations was a modified humanoid phantom CT dataset (the egsphant file was modified by replacing all materials and their densities in the file with a uniform density material). The results showed that it was feasible to calibrate both measured and simulated EPID images using the simple division method to remove the intensity modulations from the IMRT field EPID images to visualise the bony anatomy within the field. Small set-up errors were detected using the iView of 0.50 ± 0.06 mm horizontally and 0.10 ± 0.00 mm vertically.

The final stage of this study investigated the sensitivity of the method to set-up errors. Errors in translation (1, 2, 5 and 10 mm longitudinally and laterally) and rotation (1° and 2°) were introduced to the phantom measurements. Three methods were used to detect the introduced errors. These methods were visual inspection, maximum linear Pearson correlation (MLPC), and iView software. The visual inspection method showed that translation errors of 5 mm and greater were observable when a reference line was placed on reference bony anatomy in the reference image, and the C-measured image was aligned with the reference image. The MLPC method showed sensitivity to detecting the smallest rotation error of 1°

degree. Both MLPC and iView methods showed enough sensitivity to detect the smallest translation error introduced of 1 mm. The accuracy of detecting 1 mm translation error was comparable to the geometric accuracy ranges by various IGRT technologies such as kV CBCT. Thus, the MLPC method qualifies to be used as a potential tool for patient position verification alongside iView clinical software and other available geometrical verification software.

Finally, it was concluded that the calibrated MC IMRT EPID images were of a quality that allowed visibility of the bone anatomy and the field edge. The bone anatomy was visualised in these images using the simple division method. The quality of these MC calibrated IMRT EPID images qualifies them to be to be potentially suitable for patient position/set-up verification during the IMRT treatment. Set-up errors and random errors as small as 1 mm were detected by different methods using these images as a reference image. These results were validated through introduced errors of 1, 2, 5, and 10 mm translations and rotations of 1° and 2°. These images and verification methods should potentially complement currently available position verification protocols to assist in evaluating the systematic set-up errors using the proposed imaging procedure described in this thesis. Moreover, these MC portal images generated in this study could be used in dose verification pre/post the treatment since they also carry dose distribution information at different depths/layers.

Table of Contents

List of Figures

List of Tables

List of Abbreviations

3-D CRT: Three-dimensional conformal radiotherapy

AIHW: The Australian Institute of Health and Welfare

CM: Component module

CRT: Conformal radiotherapy

CT: Computed tomography

CTV: Clinical target volume

DQE: The detective quantum efficiency

DRR: Digitally reconstructed radiograph

ECUT: Electron cut-off

EGS: Electron-Gamma-Showers

EPID: Electronic portal imaging device

GTV: Gross target volume

HIS: Heimann Information Software

ICRU: The International Commission on Radiological Units and Measurements

IMRT: Intensity modulated radiotherapy

kV: Kilovolt

MC: Monte-Carlo

MCDTK: Monte Carlo DICOM Toolkit

MeV: Mega electron volt

MLC: Multi-leaf collimator

MLPC: The Maximum Linear Pearson Correlation

MV:Megavolt

NTCP: Normal tissue complication probability

OAR: Organs at risk

PCUT: Photon cut-off

PTV: Planning target volume

PW: Plastic water

ROI: Region of interest

SD: Standard deviation

SNR: Signal to noise ratio

TCP: Tumour control probability

WHO: World Health Organization

List of Presentations

1. M. Al-roumi, Bone anatomy information extraction from IMRT EPID images, presented at the ACPSEM QLD branch meeting at Queensland University of Technology, September 2012.

2. M. Al-roumi, K. Biggerstaff, D. Warne, and A. Fielding, Calibration of treatment time intensity modulated EPID images for anatomical imaging. Accepted abstract for oral seminar at the Engineering and Physical Sciences in Medicine (EPSM) Conference 2013, 3rd–7th November 2013, Perth, Australia.

3. M. Al-roumi, K. Biggerstaff, D. Warne and A. Fielding, "Calibration of treatment time intensity modulated EPID images for anatomical imaging". Accepted abstract for poster presentation at the 3rd International Conference on Radiation Medicine (ICRM) 2014, 16th. - 20th. Feb 2014, Riyadh, Saudi Arabia.

Statement of Original Authorship

The work contained in this thesis has not been previously submitted to meet requirements for an award at this or any other higher education institution. To the best of my knowledge and belief, the thesis contains no material previously published or written by another person except where due reference is made.

QUT Verified Signature

Signature:

Date: 16/01/2018

Acknowledgements

Chapter 1: Introduction

Radiotherapy is one of the most commonly used treatments for cancer. Radiotherapy uses ionising radiation to damage the DNA structure of the cancerous cells (tumours). Treatments are planned such that the dose delivered to the tumour volume is maximised and the dose delivered to the surrounding healthy normal tissue and organs at risk (OAR) is minimised. This study focuses on external beam radiotherapy using photon beams.

Generally, successful radiation treatment depends on the accuracy of the dose delivered to the tumour volume. Radiotherapy involves two aspects of accuracy: dosimetric and geometric [1]. Geometric accuracy refers to the target volume and other important anatomy being correctly placed relative to the treatment field, where the patient geometry and the position of the patient are in the reference position defined as part of the planning process. Several factors affect geometric accuracy of the dose delivered to the target volume, including patient alignment or set-up for treatment, patient motion, or the internal anatomy motion of the patient. Geometric accuracy and patient position during intensity modulated radiotherapy (IMRT) treatment is the subject of this study. Dosimetric accuracy refers to the accuracy of the dose delivered to the patient as planned.

Therefore, it is desirable that patient position be checked and verified before, and ideally during treatment [2]. To reduce set-up errors, patient position is often verified by comparing images acquired pre-treatment (i.e. EPID images) with a reference image; typically a digitally reconstructed radiograph (DRR) or a simulator film image with the patient in the planned reference position. Based on this geometrical verification, if there is any significant shift in the patient's anatomy (i.e. bones and tissue) relative to the field edges, then the patient position can be adjusted to match the reference position.

This study focuses on the current limitations of imaging during an IMRT treatment, specifically, that a patient can be imaged before or after treatment, but not during treatment due to the modulations in the field that mask the patient's anatomy. The aim of this study is to be able to generate a Monte Carlo (MC) simulated image of

patient position during IMRT treatments to be used as a reference image, enabling comparison with measured IMRT EPID images after calibrating both images to verify the phantom position.

In previous studies carried out by Fielding et al. [3, 4], measured EPID images were used in the verification of IMRT treatments using different delivery techniques for IMRT. It was shown that it is feasible to use measured EPID images, but there were no reference images for comparison. If MC EPID images can show the bone structure of the patient after calibration, then these images will be available to complement the currently available verification process of the patient's position.

Chapter Two presents a detailed background of radiotherapy with a focus on IMRT and the treatment planning involved in this modality as well as the three dimensional conformal radiotherapy.

Chapter Three develops the Monte Carlo models used in this work. A description of the Monte Carlo software EGSnrc and the associated user codes BEAMnrc and DOSXYZnrc [5-7] is also provided.

Chapter four uses the MC models developed in chapter three to generate a simple IMRT field from a set of simple square fields (5×5, 10×10, 15×15, 20×20, and 25×25 cm^2). The study develops a test of the ability of MC code to generate clinical IMRT fields. A simple model lung phantom was designed for this study and images were calculated using DOSXYZnrc in the model detector of the EPID. The calibration method (division method) [8] of the MC IMRT EPID images was tested in this chapter and implemented and validated in Chapter Five. The results were used as a proof of principle of the ability to simulate IMRT fields using the BEAMnrc code using the step-and-shoot delivery technique, and the ability to remove beam modulations and reveal the lung anatomy in the images.

Chapter Five introduces more clinical examples. Several studies investigated the calibration process of both measured and simulated images. A prostate IMRT plan, a head and neck IMRT plan, and phantoms of different geometry and materials were investigated. These three studies used plastic water slabs as the calibration phantom

for measured images. The modified CT data file of the egsphant file was the calibration phantom for the simulated images.

Chapter Six investigates the sensitivity of the method to detecting intentionally introduced translation and rotation errors in the measured IMRT EPID images of the head and neck phantom, using a calibrated MC IMRT EPID image as a reference image. Three different methods were used to detect those errors – visual inspection, maximum linear Pearson correlation (MLPC), and the iView method.

Finally, Chapter 7 summarises and discusses the outcomes of this project, and includes the overall conclusions of all the studies. Suggested further work and investigations are also included in this chapter.

Chapter 2: Background

2.1   CANCER

Cancer is the uncontrolled growth of cells in the body. Normally cells grow and divide depending on the need to keep the same number of cells balanced. When cells begin to grow and divide rapidly without control in a localised region; tumours can develop. Those cells can be either malignant or benign. In the latter case, these cells are removed and they will not grow back or spread, but if malignant, the cells are cancerous and can invade other cells surrounding them. They can also travel to affect other organs through blood flow and the lymphatic system, where they are called metastasis [9-11].

Cancer is a major cause of death worldwide; it was the cause of death for 7.9 million deaths (around 13% of all deaths) in 2007. Cancer of the lung, stomach, liver, colon, and breast cancer cause the most cancer deaths each year as shown in figure 2-1. About 72% of all cancer deaths in 2007 occurred in low- and middle-income countries. Deaths from cancer worldwide are increasing with an estimated 12 million deaths expected to occur in 2030 [12].
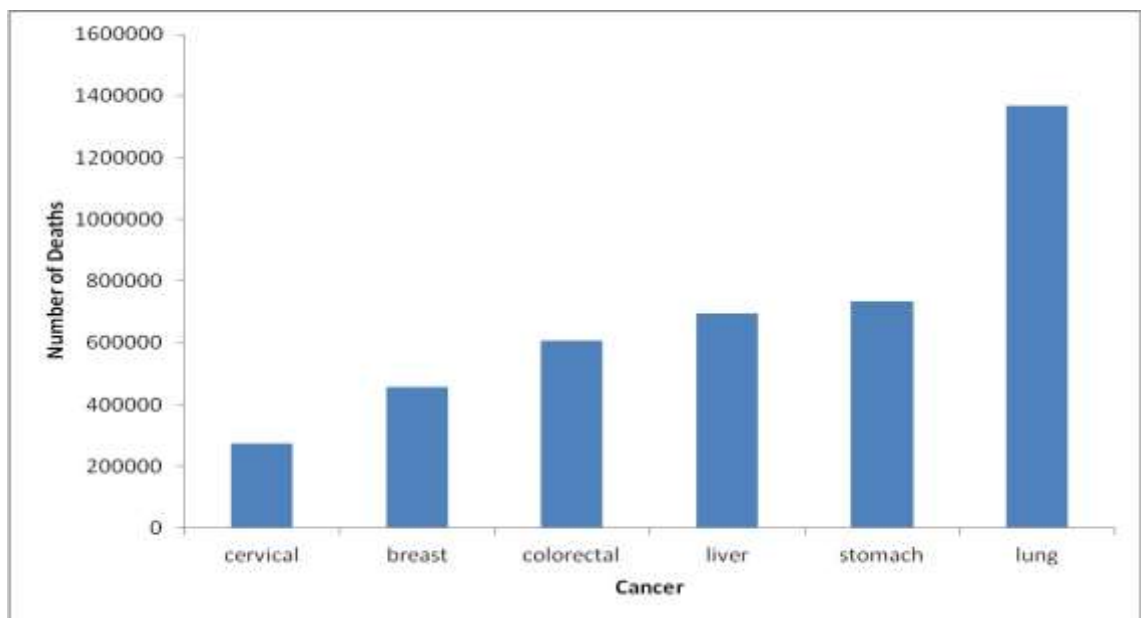
Figure 2-1: *The number of deaths caused by most common cancers as reported by World Health Organization for 2008. AIHW's report 2009 [1].*

Cancer in Australia is a major cause of death and an enormous burden on the health care cost for the future. Cancer claimed more than 43,000 lives in 2010 in Australia. There has been an increase of annual cancer deaths of more than 15,000 in the past 30 years. The Australian Institute of Health and Welfare (AIHW) reported a future estimate of expected cancer cases diagnoses to rise from 121,500 cases in 2011 to 150,000 cases by 2020. The cancer incidence ratio in men was 1 in 2 and 1 in 3 women by the age of 85. The Australian government cancer research funds accounts for around 22% of all research expenditure [13-16].

2.2   CANCER TREATMENT

There are different approaches to cancer treatment, which can be relatively successful if cancer is diagnosed in its early stages [17, 18]. The main approaches used are surgery, chemotherapy, and radiotherapy. The treatment used depends on the type and staging of the cancer. Radiation can be used with the aim either of curing the patient, or to offer the patient palliation. It was reported that drugs contribute 2% of the cure in cancer patients, radiotherapy and surgery combined cure up to 30% [19]. Radiation therapy treatment can be used either alone, pre-surgery, during surgery, or post-surgery, and can be combined with chemotherapy.

2.3   RADIATION PHYSICS

The term radiation term refers to the emission and spread of energy through space or medium [20, 21]. This energy takes form from high-speed particles such as electrons and electromagnetic waves [20, 22] which includes visible light and X-rays [21]. Radiation is classified as either ionising or non-ionising radiation. Ionisation occurs when neutral atoms gain or lose one or more electrons, so it becomes either positively or negatively charged.

2.3.1   Radiation interaction with the medium

If an X-ray passes through a medium, interactions between the X-ray and medium's atoms take place and energy will be transferred to the medium causing ionisations and excitations of the medium's atoms. Interactions between the ionising radiation beam and the medium depend on the type of energy of the original radiation beam and the

medium's atomic structure. The reduction of the number of photons is known as attenuation. Attenuation depends on the original number of photons and the thickness of the medium (absorber). When photons are absorbed their energy has been deposited into the medium. When the original beam is deflected, causing photons to follow a new path different to the original beam, this is known as scattering [20, 21, 23]. The reduction in the beam intensity depends on the thickness of the medium that the beam is passing through, and it decreases exponentially.

$$\mathbf{I} = \mathbf{I_\circ} \times \mathbf{e}^{-\mu t}$$

[2-1]

Where: I = intensity transmitted, $I_\circ$ = intensity of the original beam, μ = absorption coefficient, and t = medium (i.e. tissue) thickness.

An X-ray beam produced from the target in the X-ray tube or any radioactive source consists of a large number of photons. This beam is attenuated in a medium by five types of interactions [20].

• Photodisintegration: this is caused by interactions between high-energy photons (> 10 MeV) and a nucleus, resulting in the emission of a neutron by the nucleus [20].

• Coherent scattering: when a photon passes near a nucleus, then the electrons will begin oscillating. This oscillation causes the radiation of energy from the moving electron, similar to the original photon energy, and a scattering of photons in small angles. This type of scattering occurs in materials with a high atomic number with low energy photons involved [20, 24]. This scattering, also known as classical scattering, has two types: Rayleigh scattering and Thomson scattering [21].

The remaining three important types of interactions for radiotherapy treatments are:

• Photoelectric effect: this occurs when a photon beam interacts with an atom and transfers its entire energy to the electrons of that atom [21]. This energy transfer causes the ejection of electrons from its inner orbits, when the photon energy is greater than the electron binding energy. These electrons are known as photoelectrons [20, 23]. This type of interaction is dominant in the diagnostic radiology energy range and is most likely for high Z atoms and energies < 35 kV. For example, bones absorb more radiation than soft tissue or water due to the higher atomic number, [21]. Photoelectric effect is an important effect in radiotherapy treatment [23].

- Compton scattering: this involves the photon interacting with a "free" electron, which means its binding energy is, much less than the incident photon energy, where the photon transfers part of its energy to the electron. The free electron is ejected from its orbit with an angle defined by the kinematics of the interaction. This electron interacts with the atoms, losing energy in the medium before reaching rest. These electron-atom interactions cause radiation damage to cells [23]. Compton scattering is the predominant interaction at MV energies in soft tissue (i.e. 45 kV - 50 MV) [21]. Another factor that affects the probability of Compton scattering occurrence is the electron density of the absorber. A Compton scattering cross section depends on the electron density of the medium, therefore, since bones have higher electron density than tissue or water, radiation absorption in bone is higher than in tissue [25].

- Pair production: the photon undergoes transformation into an electron and a positron around the nucleus. The electron loses all of its energy through the absorption process, where the positron's energy drops down to a low energy while traversing through a medium via ionising of the medium's atoms until it attracts an electron to combine with it through an annihilation process [21, 23, 24]. The latter process causes the appearance of two photons. They move in opposite directions, with a total momentum of zero (i.e. conservation of momentum) [21, 23, 24]. When a photon with energy > 1.024 MeV is absorbed by the nucleus, this photon energy is transformed into mass (i.e. electron-positron pair, $E = mc^2$). This phenomenon occurs above photon energy 1.022 MeV, and the occurrence increases with high atomic number materials, and at energies > 10 MeV [21].

2.4   RADIOTHERAPY TREATMENT

Radiotherapy involves the use of ionising radiation to kill the cancer cells by delivering the maximum possible radiation dose, while simultaneously delivering the minimal possible radiation dose to healthy surrounding tissue and organs at risk (OAR) [13, 17]. This maximises the tumour control probability (TCP) and minimises normal tissue complication probability (NTCP) [20, 26, 27]. If the medium that the X-rays are passing through is body tissue, then the energy may be deposited in the cells, causing damage to the cells and their ability to divide, which is the principle of radiotherapy treatment.

Radiotherapy is delivered using an external source (e.g. electron, photon beam) or internally by placing one or more radioactive sources in or near the target volume (brachytherapy) [17, 18]. The main focus of this study is the use of external radiation therapy using high-energy photon beams of 6 MV and 10 MV using IMRT modality.

2.4.1 Conformal Radiotherapy (CRT) and 3-D CRT

CRT allows the delivery of high doses to the tumour volume, while sparing the healthy surrounding tissue and OAR. It's often used with the intention of conceivably curative treatment [28]. The simplest radiation beam setup of CRT or the 2-dimentional (2D) radiotherapy is the use of two opposed lateral fields, or four fields 'box' [29]. Advancement in computer technology, radiotherapy treatment delivery machines, radiotherapy treatment planning systems (TPS) and the imaging technologies (i.e. computed tomography (CT), magnetic resonance imaging (MRI) and ultrasound) led to more conformal radiotherapy modalities such as 3-D CRT, IMRT, 4-D CRT and image guided radiotherapy (IGRT) [30].

3-D CRT is based on 3-dimensional anatomical information planning [31]. It was developed to give a better delineation for the cancer volume and organs at risk, to achieve a high dose with conformity in the targeted cancer volume and consequently minimise the dose to normal surrounding tissue [28, 29]. The fields used in the treatment are shaped individually, have uniform intensities, and delivered from different gantry angles to treat the targeted tumor volume. Using 3-D CRT can lead to better physical and biological results clinically [31], because the tumour volume is delineated with much better accuracy than CRT.

2.4.2   Intensity Modulated Radiotherapy (IMRT)

IMRT is an advanced method of 3-D CRT and one of the most precise forms of delivery of external beam in radiotherapy. In this modality, intensity modulated fields containing a different number of segments/beamlets; each are delivered from different gantry angles around the patient with high precision and high doses to the target volume. The intensities are modulated so each field will have high and low intensity radiation within the same field, allowing better control over the distribution of the radiation dose in the target cancer volume [29]. The reasons for choosing the IMRT modality for treatment are:

i)   Concavity of PTVs: almost 30% of clinical cases require concave dose distribution. IMRT is considered a successful method to achieve these dose distributions [19].

ii)   Conformal avoidance: the OAR and important tissue structures can be better spared in IMRT than in 3-D CRT due to beam shaping via MLCs. IMRT is able to create multiple avoidance structures, while treating different targets [32].

The first experimental implementation of IMRT was by Bortfeld and Boyer in 1994, where they used multiple static fields [21, 31, 33]. IMRT has become an active area of research interest. Historically, as reported by S. Webb (2005) there was independent research work conducted by himself, Bortfeld and Radhe Mohan on generating radiation fields with modulated fluence in 1988. Until 1999, published research in the IMRT field had been minimal, with most work focusing on planning, not on delivery [31]. The appearance of commercial IMRT systems – with all the improvements and developments of those systems – made IMRT more widespread, and it is now used in many clinical departments around the world. As a result of the extensive research, IMRT has emerged as a revolutionary radiotherapy technology in treating cancer with external high-energy beam. Figure 2-6 shows the difference between 3-D CRT and IMRT in dose coverage and safety margins included in the treatment. This is achieved via either static or dynamic MLC delivery techniques to deliver those multiple static beams sequentially [34]. These two techniques of delivery will be explained in more detail in the IMRT delivery techniques sections.
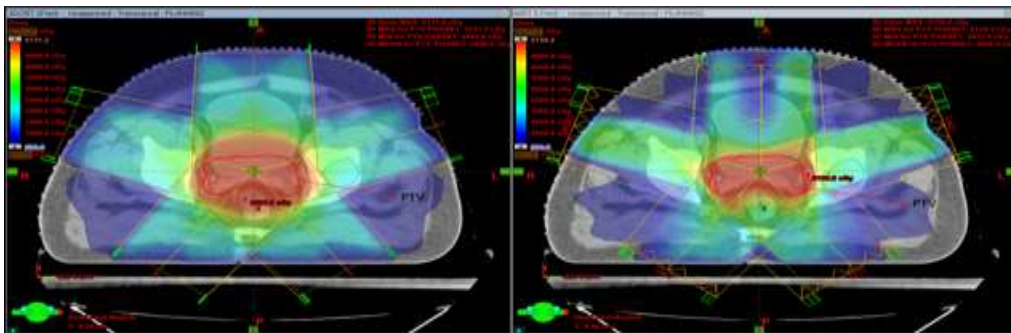
Figure 2-2: *The difference between 3-D CRT and IMRT in dose distribution in the target volume and the tissue spared. Left figure shows 3-D CRT dose distribution levels, while the right represents that of the IMRT [30] (printed with permission).*

2.5   EXTERNAL RADIOTHERAPY TREATMENT PLANNING

Uncertainty in knowledge of the true extent or spread of the cancer volume is a main limiting factor in radiotherapy [20]. Therefore if the treated cancer volume does not include the microscopic spread of the cancer, the treatment could result in a non-desirable outcome [20]. There are other factors that could affect the treatment outcome, such as the organ motion, tumour volume motion, and patient motion. These factors and others could lead to systematic and random errors. These errors should be considered when the cancer volume is defined [20].

This section summarizes the conventional and 3-D CRT treatment planning process. The next section will detail the differences between the conventional treatment planning and the IMRT planning process. The conventional planning process in few steps [52]:

Volume definition: Target volumes are defined by ICRU reports 50 and 62 [35, 36] as shown in Figure 2-3. The definition of these volumes is significant for 3-D radiotherapy treatment planning and radiation dose reporting. The gross tumour volume (GTV) is normally defined using computed tomography (CT) and/or magnetic resonance imaging (MRI) scanning/imaging techniques. A clinical target volume (CTV) is then defined by adding a margin to the GTV, which includes any microscopic tumour spread. The internal margin (IM) is added to the CTV to account for any internal organ in the patient. The IM leads to a new intermediate volume defined between the CTV and planning target volume (PTV) which is known as the internal target volume (ITV). Finally, the PTV is defined, which aims to account for motion and positioning inaccuracies. The PTV defines the volume to be irradiated [37]. This allows for patient position and setup-errors to be considered. The PTV is used in treatment planning [38]. The organs at risk (OAR) should be outlined in the treatment plan so that they can be spared during the treatment. Determining the GTV is based on the oncologist's clinical tests and images acquired for this reason, such as MRI or CT, to define the volume of the tumour. Once the target volume has been determined and radiotherapy treatment is chosen, the CTV is determined based on the patient's histological medical examinations or surgical specimens, by assessing the spread of tumour around the GTV [39]. This delineation of the CTV is a highly subjective process [31, 38, 40, 41].
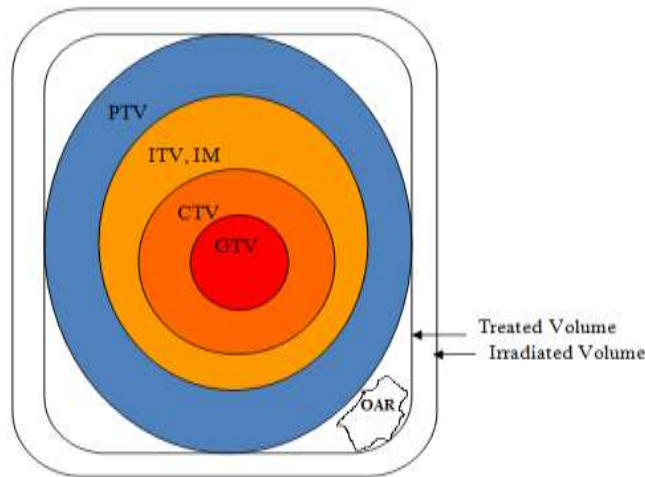
Figure 2-3: *Schematic view of radiotherapy volumes as defined in ICRU reports 50 and 62 [35, 36].*

Dose specification: The knowledge of the total and fractional dose delivered to the target volume over the treatment period is crucial. This knowledge allows for suitable comparison of the treatment outcome results. The ICRU reports 23, 50 and 83 [35, 42] have defined different dosimetric end-points for reporting the dose values, the minimum, maximum and mean target dose at these points. The reference dose point defined by the ICRU is located at a point where the dose can be calculated accurately. The centre of the PTV along the isocentre or beams intersection point is the suitable location for the dose reference point [22].

Patient data acquisition: to carry out a good treatment plan, reliable patient data is required. This data forms a significant part of the simulation and planning process. The patient dimensions can be calculated using the CT slices or from any other image generated via other imaging technologies such as MRI and/or PET. The bony anatomy or the fiducial markers can be used in matching position in the plan with the same positions on the patient [22]. The patient information can be acquired using different imaging modalities such as CT, MRI with CT image (fusion) or any other imaging technologies. The defined/contoured volumes are drawn and outlined as well as the OAR on the CT slices [22].

Patient set-up and immobilisation: establishing the patient position for treatment is significant. A suitable immobilisation device is used –if needed- to maintain the patient in

the reference position for the treatment. The accuracy of the patient position and beam delivery decide the need for immobilisation device or not for treatment. These devices are used to immobilise the patient movement during the treatment or to provide a dependable means of reproducing the patient position in the simulation process to treatment [22, 43]. The most used immobilisation devices are the head rest and plastic mask in head and neck treatments. The vacuum-based devises are commonly used when treating the thoracic or pelvic area.

Localisation: The tumour location, volume, shape, and OAR are determined using CT scans (localization). This is because they present the anatomical information with high resolution and contrast in the transverse slices, based on electron density. The electron density data is important for calculating the dose inhomogeneities caused by the different structure of human tissues.

The location of the target volume can be identified on each slice. Therefore, the target volume can be linked to bony anatomy using scout images acquaired at the beginning of the CT process. Relating the target volume to the bony structure procedure allows for more accuracy in determining the tumor spread, and thus improved precision in the field definition during the simulation process [22].

'Virtual' simulation process based on CT data can be used to generate digitally reconstructed radiographs (DRRs). These DRRs can be used as the simulator graphs to determine the beam factors for treatment. The most advantageous point of the simulation process is that the anatomical structure data can be used to determine the treatment field parameters directly. The DRRs are produced by tracing the beam line from the virtual radiation source in the CT data of the patient to the film level where a synthetic radiographic image is formed based on the 3D data. This image is formed using the summation of the attenuation coefficients of the different structure along the beam line. This generates an analogous/optical density on the virtual film level that forms the image used for treatment planning.

Beam's eye view (BEV) is used to determine the beam parameters for treatment. They are projections of the field limits and the patients outlined structure in the beam line projected on a virtual film plane. They are usually masked onto the DRRs to generate the

simulation radiograph. Therefore, the field shape is decided in relation to visible anatomy in the DRR and the projected structure in the BEV. The treatment port films are compared with these DRRs periodically for the accuracy of the patient setup during the treatment.

The simulation process commences by positioning the patient in the treatment position (reference position) on the CT-simulator table. The patient position is verified using the CT scout images. Usually the patient is marked with a reference isocentre prior to the scanning. The shiftts to the isocentre are calculted using fiducial markers placed on the anterior and lateral locations on the patient and the help of the positioning lasers. The tattoos are used to mark the fiducial markers locations on the patient body for reproducing the same patient position setup in the treatment room [22, 34, 43]. Once the target volume and the OAR are outlined on the CT images and the DRR and BEVs are generated using the CT data set. The beam geometries and shielding for treatment is determined in relation to the target volume and OAR. The shielding and beam geometries are used to increase the healthy tissue sparing and maximise the dose to the target volume [22, 43]. *The dose calculations*: dosimetric issues are the focus of the quality assurance (QA), in particular dose calculation verification. Fundamentally, QA is repeated to check input data accuracy of the TPS in reproducing the input data. Dose calculation algorithms are dependent on beam data, which is input by the user. Verification measurements are performed to determine that the dose calculation algorithm is accurate. The traditional method of verification 2-D involves comparing dose display plots such as cross beam profiles, depth dose profiles (DDP) or isodose curves. The 3-D dose distributions comparisons need more complicated techniques such as dose volume histograms (DVH), dose difference displays and/or gamma index method to evaluate the agreement between measured and calculateddose distribution [22, 43].

Plan evaluation: To ensure PTV is covered and targeted effectively, the treatment portals (DRRs or simulation radiographs) are verified. The dose distributions are verified to confirm adequate coverage to the target volume and OAR are spared as required [22, 44].

Measurements are acquired for different points within the target volume, a grid of points over 2-D image or over a 3-D array of points over the patient's anatomy. The most common tools used for the evaluation of planned dose distributions are, the isodose

curves, orthogonal planes, dose statistics and DVHs. The isodose curves are used mostly when the number of the CT slices is small, and so evaluate the treatment plan in single plane or many planes. The isodose curves at the isocentre are compared with the edge of the target isodose curves. The desired ratio should be within 95-100% for the plan to be accepted while the OAR doses are within the tolerance values.

Orthogonal planes are commonly used with larger number CT slices used for dose calculations. They are used because it is unfeasible to evaluate treatment plan using axial slice isodose distributions when large number of CT planes used for calculations. Dose-statistics are different from the isodose curves and the orthogonal planes tools. They provide quantative data on the target volume and OAR and the dose received by these structure. The minimum dose, maximum dose and mean dose to the volume are reported by the dose statistics as well as the dose received by at least 95% of the target volume [22, 43] .

The treatment time and monitor units (MU) are crucial part of the dose delivery process because they define how long the beam-on for each beam used in the treatment plan as well as the MU. The MU and/or the treatment time calculations are based on the treatment techniques. There are two treatment techniques, fixed SSD or isocentric techniques. The fixed SSD technique is results in isodose distribution controlled by the percentage depth doses (PDD) for each beam. The PDD result from carefully defined dose delivery to points at the depth of dose maximum for each beam. The isocentric technique results in dose distribution that is most controlled by tissue-maximum ratios normalised in a way that the beam delivers an approved fraction of the overall dose at the isocentre [22, 43, 44]. Once the monitor units and treatment time are calculated and the 2D dose distributions, DVHs, and DRR displays, and 3D displays of anatomy, beams, and dose a hard copy output of the plan is generated for implementation. Finally the plan is transferred to the treatment machine [43].

Plan review and verification: A review of the overall planning stages is performed before the treatment delivery [34, 43, 45]. Portal images are used for verification before the treatment commences. These images are compared with simulator radiographs or DRRs. Treatment plan verification involves performing a check on both types of accuracy – dosimetric and geometric – in radiotherapy treatment pre-treatment delivery. Geometric

verification is performed to ensure that the radiation doses are delivered to the right volume location within the limits set by the uncertainty margins as per the plan [46].

The portal images are obtained either through online electronic portal imaging devices/systems (EPIDs). Online portal imaging using electronic portal imaging devices (EPIDs) are usually attached to the treatment machine (i.e. linear accelerator (linac)) via mechanical arms or semi-robotic arms. These imaging systems are categorised according to the radiation detectors into three types, fluoroscopic detectors, ionisation chamber detectors and amorphous silicon detectors (a-Si). They are computer controlled to process transferred detector information and convert this information to an image. The quality of images generated via these systems differs from one system to another.

The a-Si detector is used in this study. This type of detector comprises an array that consists of amorphous silicon photodiodes and transistors arranged in a rectangular matrix. The detector uses a combination of metal plate and fluorescent phosphor screen. Electron-hole pairs are generated in the photodiodes by the light photons. The quantity of these electron-hole pairs is relative to the intensity allowing an image to be acquired. The contrast and resolution of the generated images via this system are higher than the images generated via the other two detectors systems. These three online portal imaging systems are explained in detail in the electronic portal imaging devices section [22].

For geometric verification, usually two orthogonal EPID images for all fields are acquired pre-treatment and compared with the reference image. Both images are inspected visually and via verification software to verify the patient position and setup-errors to be adjusted before the treatment as needed [34]. Therefore, a good quality reference image is required for this process.

Treatment delivery: Once the treatment plan is approved after comprehensive review of all the aspects of the planning process including the dosimetric and geometric verifications, the treatment can commence.

2.6   TREATMENT PLANNING SYSTEMS

The planning technique explained above that is used for 3-D CRT planning is known as the forward planning technique. This technique involves trying variety of arrangements

of beam angles, weights, couch angles and beam modifiers devices and other parameters to achieve the optimal dose distribution desired. These variations of the different combinations of parameters are performed manually until satisfactory dose distribution is achieved as required.

The radiotherapy modality of investigation in this project is IMRT. The planning process of IMRT is similar to 3-D CRT with some critical differences should be pointed out and detailed. To achieve a successful treatment, IMRT requires a much more complicated and time-consuming planning. More attention and parameters consideration is required in IMRT planning due to dose escalation within targets [47-49]. The planning technique that is used in IMRT planning is known as the inverse planning technique. In IMRT delivery, each field is composed of several beamlets/segments with varying intensity modulation. Therefore extracting the optimal intensity profiles for each field size requires sophisticated dose computation algorithms. This type of planning algorithm is known as the inverse planning algorithm. Brahme and Bortfeld have carried out the pioneering work in the development of inverse treatment planning algorithms. In inverse planning, planners define the required dose distributions in the target volume using constraints, and the treatment planning system software calculates beam weights and modulated intensity patterns via an optimisation algorithm [50-53]. The optimisation results can be changed by the planner by changing the desired dose and constraints and then re-optimising [50]. The optimisation algorithm is a mathematical approach to achieve the best physical and technical possible treatment plan that satisfy specified physical and clinical measures under certain restraints, using state-of-the-art algorithms [50].

There are two types of optimisation criteria based on physical and/or biological standards. The physical measures depend on the dose coverage of the target and normal tissues. The biological measures based on tumor control probability (TCP) and normal tissue complication probability (NTCP). The inverse planning system represents constraints and goals such as the dose distribution by using single dose value, dose volume points, and DVHs all in a cost function. These constraints must be minimised or maximised in the optimisation algorithm input for the target volume and normal tissues based on the optimisation measures and priorities. The object of the optimisation process is to alter the beam intensities so that the best possible dose distribution required is achieved. The parameters that can be altered -by planners- for optimisation are the intensity maps, beam

angles, beam energy and number of beams. If the planner alters these constraints, the cost function is altered resulting in impact on the results. Therefore, a good inverse planning system should offer a cost function with needs meeting the clinical requirements and concerns [50].

There are some planning considerations in the inverse planning, which can be summarised as reported by the AAPM report [50]:

1. *Dose calculations and beam modelling:* The doses in IMRT are calculated by splitting the beams into smaller subdivisions known as *beamlets* or *segments*. The small dimension of the segments is associated with small collimator openings. Making the modelling of the head scatter important for head scatter evaluation and for applying the appropriate corrections. The transmission of fields through the collimators and penumbra in CRT affect the results at the edges of the beams and outside the beams, hence, they have reduced the clinical importance. In IMRT, modelling of the transmission and penumbra is an imperative issue as segment intensities vary through MLC movement during irradiation. The dosimetric precision depends on the reliability of the penumbra representation due to the various beams edges within the GTV [43, 50].

2. *Leaf sequencing and deliverability:* the segment intensities and their delivery are determined by the IMRT planning system. Therefore, the collimator transmission, leaf shape and sides affect the final delivered doses. There are different available systems take care of the interchange between the inverse planning, leaf sequencing and dose calculations in various means. These methods influence the speed of planning and the precision of dose calculations. For instance, certain systems allow weight optimisation of segments of actual delivery sequence so that the dose conformation is improved. Some IMRT systems use different dose calculations algorithms for faster optimisation [43, 50].

3. *Heterogeneity corrections:* As IMRT is delivered using a large number of radiation beams and orientations, and higher dose gradients in the target volume, therefore heterogeneity corrections are more important in IMRT planning than CRT and 3-D CRT planning. The treatment outcome will be compromised, if these heterogeneity (i.e. air lung, bone) corrections are not applied [43, 50].

4. There are other specific differences between IMRT and conventional radiotherapy techniques. These are concerns solely due to the escalated doses in this modality of treatment. These planning issues include:

I. Dose uniformity is the main objective of IMRT to the target volume. The uniformity of the dose within the target volume may be affected, when IMRT is used to produce dose distributions with concave shapes targets and steep gradients around OAR. An increase of dose inhomogeneity is expected in the target volume when there is increase in the dose difference between required dose in the target and OAR, concavity of the required dose increases, the distance between target and OAR decreases, or the number of beam directions decrease. Therefore, the inverse planning algorithm should give flexibility to the user to maintain the dose balance between target volume and OAR [43, 50].

II. Target volume and OAR delineation is a crucial process for IMRT. The inverse planning delegates more responsibility to the planner in delineating the target volume and OAR. In IMRT, all the volumes of the target, OAR and critical structure must be defined and contoured clearly. If these critical structures are not well defined, it may result in incorrectly high doses delivered to them. Another reason for contouring all the area of interest in IMRT is to evaluate DVHs. Additionally, high dose areas can appear in unrestrained normal tissues. Therefore, constraints must be applied normal tissues to avoid such unwanted high dose issues [43, 50].

III. Dose grid size in IMRT needs to be finer than the size of segments or fluence map in order to adequately sample the effects of the modulations, since the size of the OAR and critical structure are affected by the large dose gradients produced by IMRT near them [43, 50].

IV. Build-up region, special attention must be paid into the build-up region when target volumes are delineated and contoured within this region for two reasons. Firstly, usually there are discrepancies between the calculated doses and actual delivered doses to the target volumes. Secondly, the low doses in the build-up region can be mis-interpreted by the inverse planning algorithm as underdosing the target volume. Hence, the increase in the intensities of the corresponding segments by the planning algorithm. Consequently, hot spots within the target volume may result in the total plan quality reduced. Dose modifiers such as bolus

should be used to resolve the hot spots issue, in the case of the target volume is actually in the build-up region [43, 50].

V. Mobile targets such as lungs motion in inverse planning is more problematic than in CRT planning. The day-to-day changes in shape are accounted for in CRT planning by adding beam margins in air, which is known as flash. The inverse planning algorithm treats a well-defined target. Significant variations in the delivered doses to the target volume will be encountered when tissues are moved via organ motion (i.e. respiratory motion) during treatment over distances that are comparable to the segments size. Hence, plan evaluation must consider the differences between the living patient in the treatment and the image in the plan [43, 50].

VI. Margins added to the treated volume in in radiotherapy are a significant issue. Usually the target volume contours can be expanded via the planning system in three dimensions. These systems vary in the method they use to increase the targets and critical structure boundaries and how these extended regions are treated especially when inverse planning is used. Additionally, the localisation errors are significant in IMRT, because the result in larger dose error, due to the large dose gradient in IMRT [43, 50].

VII. Plan evaluation for IMRT involves thorough evaluation of all prospective problems that could compromise the accuracy of the delivered doses to targets and normal tissues. IMRT could create hot spots or cold spots in unpredicted positions. There is a probability that doses occur outside the target resulting in increase of the NTCP. Low doses may occur within the target decreasing the TCP. A combination of dose evaluation tools must be used for IMRT. Some of the aspects that should be evaluated in IMRT plan are the dose uniformity within the target, normal tissue sparing, the safety of margins and dose gradients, build-up region high doses and using inhomogeneity corrections.

Plan validation involves dosimetric and geometric verification to ensure satisfactory doses delivery to the targets. The planned dose distributions approval based on the delivery of uniform dose to the target volume and the doses delivered to the critical structures are within or below the tolerance levels that is specified in the plan. *Dosimetric verification* is performed using different

available dosimetry systems. Due to the complexity of IMRT and the large dose gradients in the target, there is a potential for high discrepancies in the dose distributions. Therefore, the chosen system for the dosimetric verification is important and depends on the parameters needed for quality assurance procedures. There are different combinations of checks are developed by the physicists as part of the quality assurance (QA) for IMRT plan. These techniques include calculations, inspection, and experiment.

1. Calculation techniques are used to verify the MU and absolute doses via particular algorithms. These algorithms calculate the doses from the MLC delivery files and compare them with TPS's predicted dose. Other algorithms calculate the intensities from the delivery files and estimate the dose by applying certain techniques. These different dose calculation techniques are based on pre-treatment information will not be able detect any dose errors in the treatment delivery. Therefore, other techniques should be used for dose calculations based on information derived from the delivery files (i.e. EPID measurements).

2. Experimental technique (verification measurements) uses a flat phantom to verify the deliverable dose distribution. The IMRT plan is superimposed on the phantom to generate the verification plan by applying the parameters of each field such as the MLC segments, leaf trajectories, and MU for each field. The phantoms used in the verification are specifically designed for IMRT, and comprise different inhomogeneity incorporated to account for verification of the plans and algorithms that are used for tissue inhomogeneity corrections. The phantom is then irradiated as per the plan and the doses are measured using certain detector such as ion chamber. The measured dose in the phantom is then compared with predicted doses to the phantom.

3. There are other plan verification tests required for IMRT. The AAPM reports 46 and 62 have recommended certain checks for individual plans that apply for IMRT [43, 54]. The target volume coverage must be checked -to ensure there is accurate coverage- in three dimensions. Another important verification check is the treatment isocentre pre-treatment as the inverse planning systems have the ability to shift the isocentre from the original set-up, as most of the CRT

systems. A comparison between the plan DRRs with EPID images of the treatment is usually performed to ensure the accuracy of the field isocentre.

4. *Position verification* is an imperative part of the IMRT plan validation. As mentioned above, the treatment isocentre must be verified so that there is a match between the planned isocentre and the treatment isocentre. The portal images of the treatment fields must be acquired frequently (i.e. weekly) and compared with the plan DRRs. Currently, daily CBCTs images are are acquired and compared with the reference image.

Finally, the IMRT planning process follows the same conventional planning with some differences at the start and at the end of the planning procedure steps. These issues have been pointed out and detailed above. The IMRT planning include, patient positioning and immobilisation, patient data and image acquisition, structure segmentation (targets delineation), IMRT planning using inverse planning technique, file transfer and management, plan validation and verification (dosimetric and geometric verification) and finally IMRT delivery. Figure 2-4 summarises the overall IMRT planning phases.
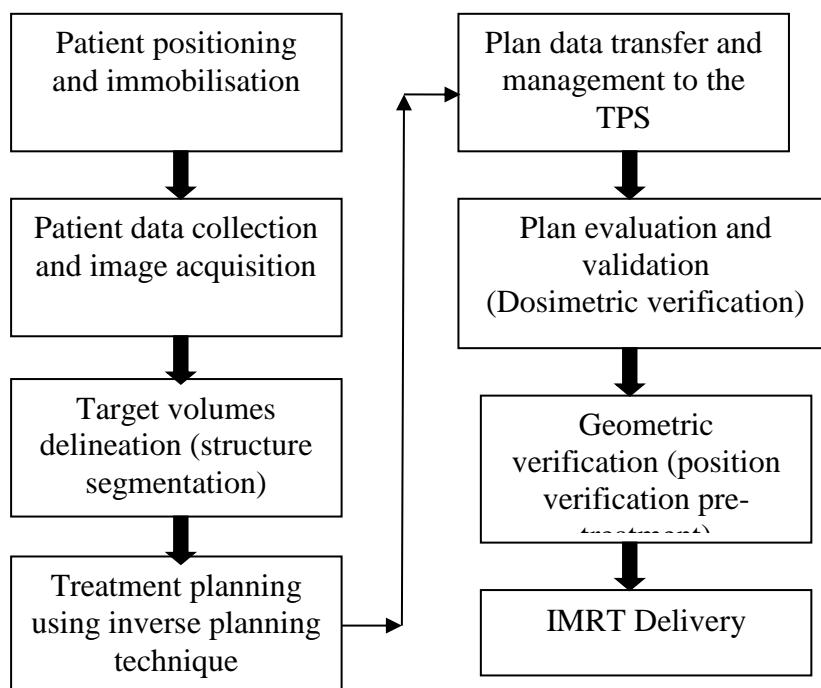
Figure 2-4: *The overall planning process of IMRT.*

2.7   IMRT DELIVERY TECHNIQUE

There are different methods of delivery for IMRT:

- The cast material compensator: these have been used in radiotherapy for a long time to produce simple forms of IMRT. These compensators are shaped to attenuate the open-field photon fluence.

- Multiple-static MLC shaped fields: known as the "step-and-shoot" technique as reported by different authors [19, 20, 55]. Using this method, patients are treated with multiple fields. They are delivered sequentially to generate an intensity-modulated beam according to the treatment plan [20]. Once the first segment is delivered the radiation is turned off until the MLC leaves are moved, then the radiation will be turned on again [20]. The step-and-shoot delivery method is a simpler technique in comparison with other delivery methods of IMRT. Non-uniform intensity profiles can be achieved by the sequential addition of regular or complicated shaped segments [19]. The multiple-static MLC shaped fields technique has been investigated in this project.

- Dynamic MLC techniques: this delivery technique has been called many different names such as "sliding window", "camera shutter", and "sweeping variable gap" [20]. The leaves usually move simultaneously with different velocities and the radiation is delivered continuously during the leaf movement [20, 34]. The leaves move with different velocities that may reach up to 2 cm/second. To minimise the treatment time, the leading leaves move as quickly as possible [20].

- Tomotherapy: simply, it is an advanced form of IMRT combined with the computed tomography (CT) or helical CT scanning with a linac. This technique is also known as slice-based therapy because it treats the tumour volume one layer at the time, where the intensity and the direction of the beam can be modified during the treatment [56, 57]. The main advantage of this approach is the minimum dose is delivered to healthy tissue and OAR.

- VMAT/RAPID arc: this technology is the most recent technology in radiation therapy and can deliver the dose required in a much shorter time in comparison with IMRT. This means less exposure to radiation and better outcomes in sparing healthy surrounding tissue and OAR during the treatment [19]. This technology is known also as intensity-modulated arc therapy (IMAT) [56][58-61].

2.8   RADIOTHERAPY ACCURACY

Successful radiotherapy outcome requires a lot of coordinated effort. This demands a high level of accuracy by following certain protocols, standards, and procedures to reduce uncertainties to a minimum. Accuracy in radiotherapy is a major issue, widely investigated by many researchers and physicists in the field. Radiotherapy accuracy involves two major types of accuracy: dosimetric and geometric accuracy [62]. The geometric accuracy and patient position verification process during IMRT is the main concern of this project.

2.8.1 Geometric verification in radiotherapy

Geometric verification refers to detecting the discrepancies between measured and planned (reference) positions (set-up errors). This process gives an indication of certainty that the target volume is treated according to the plan. Geometric verification is performed by comparing measured images taken before and ideally, during the treatment with a reference image. The reference image should show planned geometry (target volume and surrounding OAR) and the treatment field location with respect to internal anatomy (i.e. bone). These reference images are digitally reconstructed radiographs (DRRs), simulator images, or volumetric planning datasets or other images. Generating the reference image process is performed before the treatment outside the treatment room [63]. The patient is then imaged in the treatment room immediately before the treatment starts or during the treatment to develop a measured treatment image for comparison. The image guided radiotherapy (IGRT) latest technology should be used for this purpose to ensure adequate dose coverage to the target volume. Regardless of the improved imaging techniques, some unavoidable residual set-up errors may remain. These errors could be due to the patient's external movement or internal organ motions caused by natural processes such as breathing during the delivery. There are other factors could contribute to producing these set-up errors such as the patient set-up technique for treatment, immobilisation devices used to set-up the patient in the treatment position and/or CTV delineation and shape. There are several methods used for geometric verification to manage the set-up errors:

1. The off-line method: the verification procedure is performed after the treatment. The reference image is compared with measured images obtained in the treatment room pre-treatment. If there are any geometric discrepancies, they are corrected in the subsequent fraction [35, 63, 64].

2. The online method: the measured image obtained immediately before the treatment commences and compared with the reference image. Thus, any required correction is performed short time before the treatment delivery. IGRT is the most reliable technologies used in online verification. The measured images acquired in the treatment room using different imaging technologies such as kilo voltage (kV) and megavoltage (MV), EPID MV and other technologies that will be detailed in the IGRT section [35, 63, 64].

3. The real-time treatment verification method: matches the measured and reference images during the treatment radiation delivery. Some real-time systems are used for this verification. They allow for treatment to be stopped or gated to perform the corrections required [63]. Some systems detect the displacement tolerance levels specified in the plan for verification of set-up errors during the treatment. Other systems use the assumption that the distance between the external reference (i.e. marker) and internal anatomy (i.e. bony anatomy) remains constant [35, 36, 63]. This method is a type of intra-fractional verification.

Inter-fractional and intra-fractional verification: the inter-fractional verification compares set-up precision between different treatment fractions. The intrafrational verification investigates the set-up precision within a particular treatment fraction or over the period of treatment [35, 36, 63].

The set-up errors are calculated as the shift detected between the measured image and the reference image. Set-up errors detection indicates a displacement in the treatment field position. The field displacement is identified with respect to the isocentre, treatment field edges, bony anatomy or all combined. Set-up errors accounts for translational and rotational errors. They comprise systematic and random errors [65, 66]. Three types of set-up errors should be identified to explain set-up errors [35, 36, 63]:

1. Gross error: is an undesirable set-up error that is larger than what the CTV to PTV treatment margins comprise. When the set-up errors are larger than the tolerance

values specified by the plan, they cause overdose to a portion of the OAR and underdose to a part of the target volume. There are different causes of this large type of error such as the field size, field positioning, patient alignment, or incorrect isocentre position [35, 36, 63]. Hence, this error must be corrected before the first fraction of treatment delivery. Comparing immediate pre-treatment image acquired in the treatment room with the corresponding reference image, is the method of choice to detect this error.

2. Systematic error: is the variation of the same amount and movement occurs in every fraction during the treatment course. This error refers to individual patient or to a group of patients during the treatment. For individual patient the systematic error is calculated as the mean error over the treatment course. For a group of patients it is calculated as the standard deviation (SD) of the mean error of individual patient. They are introduced usually in the treatment preparation stage [63]. Therefore, these errors are constant over the entire course of treatment [67]. They are mainly caused by target delineation process, CTV position, and shape, target changes due to growth or shrinkage between the delineation process and treatment. Another important source of systematic errors is phantom data transfer error. When initial image data is transferred to the treatment machine (linear accelerator) from the TPS, errors could occur. The possible reasons for these errors are either the laser alignment difference between the CT and the treatment machine, field borders and leaf position (MLC), couch longitudinal position difference between CT and treatment couch, isocentre position, source to surface distance (SSD) and/or gantry and collimator angle precision. These errors occur frequently in each fraction. Verification data for 3-D CRT treatment plans are attained from two imaging planes by acquiring two orthogonal images. Systematic errors are usually minimised using correction protocols for each individual patient over the course of the treatment [35, 36, 63].

3. Random errors: refers to the variation that can fluctuate in amount and direction for every treatment fraction. The random error is calculated as the standard deviation of measured errors over the treatment course for a particular patient. For a group of patients it is calculated as the mean of the random errors for individual patient. These errors are variable, and change at every treatment fraction [63]. These errors usually arise at the treatment delivery phase. They are commonly

caused by patient set-up technique, target position and shape (CTV changes between fractions) and intrafrational errors (patient external and internal movements during delivery in a treatment fraction). They are mainly affected by the immobilisation devices used and by the patient movement. Therefore, online verification method and online correction approach is the most suitable method to detect such errors and apply the suitable corrections. The random errors can be minimised by carefully choosing immobilisation devices and by providing extra attention to patient set-up procedure [35, 36, 63].

The set-up errors are measurable through a single measured image acquired and compared with the reference image for correcting in 2D. To distinguish between systematic and random errors, more than one image should be acquired to apply precise position corrections. The estimate of the mean position can be enhanced via acquiring more images for the comparison with the reference image. Therefore, images are acquired using EPID over few fractions to offer a more precise estimation of the mean position [63]. Another factor affects the margins added to CTV to the PTV is the estimated size of the set-up errors. The systematic errors may cause underdosage to a part of the CTV; therefore, these margins need to allow for sufficient coverage of the CTV to PTV. The random errors could cause a blurring of the cumulative dose distributions around the CTV. The geometric verification method that is used (off-line or online method) determines the type of error that could be detected.

The detected set-up errors using these verifications methods are analysed by the treatment verification team. An analysis based on the tolerance and action levels are carried out. The *"tolerance" values or tolerance levels* are the acceptable monitored range of set-up errors from the reference point set by the radiation oncology department. The tolerance levels in a clinical environment take into consideration factors such as immobilisation method, tolerances in equipment movement and set-up (i.e. the field isocentre tolerance value), and internal organ motion. Therefore, the tolerance levels in imaging protocols depend on the anatomical site imaged, treatment technique, CTV and PTV margins, and patient compliance during treatment. The desired tolerance levels specified for treatment verification are chosen based on the margins added to the CTV to the PTV to sustain acceptable dose coverage of the CTV. These values may be obtained from portal imaging for certain treatment region [63].

Background

Action levels of a measurement are the point at which action is necessary. They set up minimum settings where performance is considered undesirable beyond these levels. Hence, an action will be considered to alter particular parameter/s in a certain measurement, depends on the significance and risk of not adjusting that parameter. There are common actions adopted for treatment geometric verification such as further imaging, re-evaluation of systematic errors, and immediate adjustment such as adjusting the patient position (i.e. gross error detected). The action level value depends on the planning margins CTV to PTV, frequency of imaging, the daily set-up error (random error), and the strategy used to confine the set-up errors over the treatment course [63].

Depending on the action level, a correction strategy is chosen to correct the error. The main purpose of an imaging procedure for geometric verification is to provide a precise evaluation of the systematic set-up errors. These errors must be assessed over a minimum number of treatment fractions (3-4 fractions) in order to estimate the error precisely. Two types of correction strategies are used for calculated systematic errors. The *no action level (NAL) strategy [68, 69]* acts on systematic errors only and does not take action against any gross errors. The systematic error is calculated after 3-4 fractions and the correction is performed regardless of the tolerance levels for that treated area. Since this strategy does not identify any action levels for corrections, an extended NAL procedure suggests that a weekly image is acquired in addition to the first 3-4 fraction images. Hence, no action is required if verification results are within tolerance levels, otherwise additional images are acquired to decide systematic error [63].

The other correction strategy is the *shrinking action level (SAL) [70]*, which utilises an action level that decreases with the increase of the number of the fractions imaged. The mean error over the acquired images is compared with the current action level. The treatment set-up adjusted by this value if the discrepancy is larger than the action levels. The initial action level and number of images acquired determine the final action level. This strategy avoids set-up error correction in early stage of the treatment, as these errors may result from random errors instead of systematic errors [63]. Previous study compared both correction strategies using an average of ten imaged fractions for each patient, showed that NAL strategy is more efficient in terms of number of images per decline in

systematic error [63, 69]. Consequently, despite the use of correction strategy, weekly imaging is advised as an extra check for set-up errors verification.

Set-up errors (systematic and random) sources lead to discrepancies between the delivered dose and planned dose to the CTV and OAR. Higher uncertainties in the dose delivered to the tumour could lead to a reduction in the tumour control probability (TCP) and an increase in the normal tissue complication probability (NTCP) [27]. Previous studies showed that systematic errors could cause larger underdosage to the CTV than the same level of random error [45, 65-67]. In 1999, Van Herk *et al.* investigated the effect of both random and systematic geometrical errors on the probability distributions of the accumulative dose delivered to the target volume to develop a computational CTV to PTV margin rules. The study found that to deliver a minimum dose of 95% to the CTV for 90% of the patients, a CTV to PTV margin should be 2.5 times the overall SD of the systematic errors plus 1.64 times the overall SD of the random errors [67].

The geometric verification process implementation within any radiation oncology department, should take into consideration all critical aspects to ensure a reliable verification process. These aspects are: the equipment used for patient position/set-up errors verification (reference image and treatment measured image acquisition, image matching), staff tasks and preparation, imaging procedures (image acquisition and the time and frequency of imaging), set-up errors measurements (gross, systematic and random errors), tolerance and action levels and the corrective strategies, and dose considerations that are associated with exposure (from images acquisition for verification), and an audit to be performed for overall process [63].

The reference image and treatment images should be of a good quality to perform the comparison to detect any set-up errors. Both images should have an adequate quality to detect and outline the field edges and the surrounding structure (i.e. bones, soft tissue) around the treated volume. At least three points should be identified in the reference image to match these points with the treatment image. The ideal treatment image should have a reasonable spatial resolution and high contrast and a high contrast to noise ratio. Therefore, image-processing software should be used to produce the image quality entailed.

Background

Subsequent to the generation of the reference image and treatment images of a sufficient quality, they are matched using verification software, to detect any displacement between the reference image and the treatment image. Since the verification process is subjected to uncertainty from start to finish, the inaccuracy level should be assessed throughout the process, to evaluate the overall accuracy of the verification process. The QA programmes implement certain procedures to evaluate the verification system to ensure the accuracy of reported displacement information. The displacement data should be assessed for absolute accuracy, by testing and analysing data comprising an identified displacement. The user accuracy should be tested by varying the users measuring the displacements. The accuracy of the registration technique based on the use of different registration algorithms should be evaluated. The image processing could affect the measured displacement; so, this affect should be assessed. Testing the accuracy of the output consistency is performed by investigating the accuracy of the couch movements [63].

Imaging protocols that are implemented by radiation oncology department should guide the user on the suitable images, action required and one or more of the correction strategies to be used over the course of the treatment. They should state clearly the need to act directly for gross errors. In addition, they should state the number of fractions permitted before action is performed on systematic and random errors. There are various methods of treatment images acquisition that are used for geometric verification. For instance, they can be acquired using single or double exposure or inter-fractional or intra-fractional methods. The image acquisition method is dependent on the anatomy location, the visibility of the anatomy within the treatment field; and the anatomy motion during the treatment. To correct the patient position using planar images two orthogonal images should be acquired within a short time for accurate verification in 3D. These images will give displacements information that is used to correct for couch movement required for patient repositioning. The field position accuracy can be calculated in 2D or 3D depending if the planar images are acquired in 2D or 3D [63]. The number of images acquired must be acceptable and justified because of any associated doses from the radiation exposure (*concomitant exposure*) that could influence the planned dose [63, 71-73]. An estimate of the associated doses from the imaging method that is used for verification should be considered in the verification imaging protocols. There are various imaging technologies used to acquire verification image in the treatment room. These

technologies are used to acquire images either before the treatment commences or post treatment for geometric verification. The ideal verification image is acquired during the treatment to give information about the patient position.

Geometric accuracy in CRT is less sensitive to set-up errors than IMRT because of the lower dose gradients in CRT. Many researchers have investigated geometric uncertainty in many different regions of the body using conformal radiotherapy and IMRT methods [74-79].

2.8.2   Image-guided radiotherapy (IGRT)

The aim of image-guided radiotherapy is to reduce geometric uncertainties by imaging the tumour volume and nearby critical organs to enable a better dose delivery accuracy to the target volume [80]. In addition, the advantages of accurate pre-treatment alignment will involve decreasing set-up margins, which could lead to better dose avoidance of normal tissue [81, 82]. IGRT technologies are used in the treatment room for imaging. These technologies involve ultrasound, X-ray, or optical imaging to assist in the precise beam delivery to the target volume. Based on the comparison between these images and reference image, geometric uncertainties can be reduced by applying the required correction strategy. The imaging technologies used in IGRT are, computed tomography (CT), magnetic resonance imaging (MRI), positron emission tomography (PET) for tumour delination, ultrasound, and X-ray. The first imaging modalities used in IGRT were the ultrasound, radiographic films and EPIDs followed by CT cone-beam, or fan-beam with X-ray kV or MV [80, 83]. All these imaging technologies have improved the localisation of the tumour and the patient positioning and reductions in set-up errors, which has resulted in significant impact in improving geometric accuracy [84].

IGRT needs a multi-disciplinary team to assist in executing this therapeutic process. This process can be summarised in a few steps: acquiring an image for target volume location and organs at risk to be avoided, registering the target via available automatic software, and finally applying any required corrections strategy if needed. Translation and rotation errors are detected and corrected via couch movement [84]. The main advantage of the IGRT systems is that they are real-time imaging and localisation systems, such as EPID or CBCT systems. As a result of using IGRT, better accuracy in escalating the dose in the

target volume has been achieved, as well as reducing toxicity. The disadvantages or concerns about IGRT are the resource-intensive nature of delivery, and the extra dose resulting from the imaging systems used. Also, most of these systems are expensive and not available to all patients, or the image is of a poor quality and has anatomic distortion as in ultrasound images [84].

2.8.3 Image-guided radiotherapy imaging technologies

As discussed in the previous section, IGRT came into effect because of the development of the imaging technologies and treatment systems, in addition to the need for high precision between the planned dose and the delivered dose to the target volume. Based on the imaging technologies used in IGRT, systems are classified into either radiation-based or non-radiation (non-invasive)-based imaging systems. The radiation-based imaging systems include:

1. Electronic portal imaging devices (EPID): Historically, the EPIDs were developed in the 1980s to replace radiographic film for the purpose of patient set-up verification [85]. EPIDs have many advantages over X-ray film. For example, the images obtained are available immediately, so the position of the patient can be adjusted during the treatment course. Additionally, the images are digital, which helps image processing and contrast enhancement. A range of EPID technologies have emerged including "in-house" systems as well as commercial systems. There are three main EPID technologies: fluoroscopic detectors, matrix ionisation chambers, and amorphous-silicon detectors [85]. These three different EPIDs have been used to acquire patient position images on the linear accelerator. Amorphous silicon, flat-panel imagers or active matrix flat panel imagers (AMFPIs) are the latest technology were developed in late 1990s in order to improve the quality of on-line EPIDs imaging.

Camera-mirror-lens-based systems involve an X-ray scintillator that communicates with a TV camera using the mirror and lens. The X-ray converter includes a flat metal layer (usually copper with a thickness between ~1–1.5mm) and a phosphor screen. The metal layer serves to convert the X-ray beam into high-energy electrons and to block low-energy photons as well as scattered radiations to obtain an image with an improved contrast. The phosphor screen converts X-rays and electrons into visible light; a small

part of the high energy electrons are converted into light that diffuses through the screen, exiting to the mirror. The camera and lens capture a fraction of the emerging light when it is then transformed into a video signal. This signal is sent into the image processor for display on the monitor [85]. A disadvantage of camera-based EPID is that they are bulky, making the devices awkward to use [2]. However, the foremost disadvantage in a camera-based EPIDs system is a reduction in the image quality because of optical scattering in the optical chain of the EPID. Noise from TV camera-based units limit their performance [2]. Image quality therefore remains an important issue.

The scanning matrix ionisation chamber design was developed at the Netherlands Cancer Institute (NCI) and has been adopted widely [85]. The principle of this system is a liquid ionisation chamber consisting of two parallel plates, where each plate has 256 lines of electrodes separated by a small gap (~0.8 – 1.27 mm) filled with an organic liquid (iso-octane or trimethylpentane) which is ionised when the chamber is exposed to radiation. A 1 mm steel front plate provides build-up [85, 86]. A high voltage (~300V) is applied to each electrode on one plate where the other electrodes on the other plate are connected to electrometers. Small size detectors and a lack of geometric distortions in the image are the most important advantages with this system, but there is a major disadvantage where the utilisation of incident photons is low compared to that of a true area detector (low quantum detection efficiency). This problem has been improved by the fact that the rate of ion recombination in the trimethylpentane is relatively slow (~0.5 sec) [85]. In these systems the dose required to generate an image is larger than that for other available EPIDs [85].

Amorphous silicon (a-Si) EPID was developed for diagnostic applications, and used for megavoltage (MV) electronic portal images (EPI) to give high quality images at low doses. The imagers comprise three layers. First layer is a metal plate converts the incident photons to electrons and absorbs low energy scatter. The second layer is the scintillating phosphor screen, which converts electrons to visible photons. The third layer is the detector array, which is a matrix of photodiodes of which each forms a pixel Each pixel consists of a photodiode and a thin film transistor that acts as a switch to control data flow (read out) [22, 85, 87-89]. Extensive studies have been done on a-Si EPIDs [2, 67, 88-93]. A study by Herman and his colleagues concluded that EPID was a clinically realistic replacement for film [94]. The a-Si image showed significant improvement in the

image quality over film. Munro reported that a-Si EPID demonstrated the same or better spatial resolution than other available EPIDs, but demonstrated X-ray quantum limited performance [2]. The reason for limited performance was the signal-to-noise characteristics, which were determined by the quantum efficiency of the phosphor screen and not the flat panel read-out electronics. The performance of a-Si EPIDs detective quantum efficiency can be improved by increasing the thickness of the phosphor screen, but those results in loss of spatial resolution. Table 2-1 lists the commercially available EPIDs. The a-Si EPID was used in this project for acquiring the IMRT field images during the delivery of the field to the phantoms.

Table 2-1: *Summary of different commerciallyEleekta and Varian available EPID systems. From reference [66, 73].*

Make	Elekta	Varian
Model	SRI100	Vision
Type of detector	Camera	Liquid ion chamber
Linac mounted	Yes	Yes
Detector area	30x38	32.5x32.5

2. Fan-beam MVCT (Tomotherapy) is a CT scanner with a gantry able to move across the patient. The couch can be also moved towards the scanner or the gantry for imaging as well as for treatment. [95]. The treatment beam and imaging beam is generated by the treatment linac, but the imaging beam is generated with the nominal electron energy reduced to 3.5 MeV for fan-beam MVCT [81, 96]. The images generated by this system are images of the patient in the treatment position. The imaging beam is in the MV energies range, which causes low contrast images [97, 98]. The images are acquired with a pitch value of 1, 2, or 3 that translates into slice thickness of 2, 4 of 6 mm. The scans generated via this system are of low contrast, but still of enough contrast to distinguish some soft-tissue. The image registration accuracy depends on the slice thickness and pitch value as well as the scanned anatomical site. Previous studies reported that for head and thorax phantoms the registration accuracy ranged between 0.5-1.5 mm and 0.5-2 mm [99, 100].

3. Megavoltage cone-beam CT (MV-CBCT) (ArtisteTM, Siemens, Concord, CA) consists of a-Si flat panel detector for MV imaging attached to the linac to acquire MV images of the patient reference position. The detector is attached opposite the linac gantry at 145 cm source-to-imager distance, to generate the MVCT 3D-images [101]. This system demonstrates a localization accuracy of $\leq$ 1mm. The main advantage of the MV-CBCT is the use of one X-ray source and one detector (EPID) [96].

The megavoltage images have poor contrast and blur due to different reasons, such as the interaction of photons with tissue in the MV energy range, which is ruled by Compton interaction that are independent of atomic number and produce scattered photons [97, 98]. Therefore, the EPID imaging made the target localization difficult. Consequently; the use of implanted gold seeds within the target volume so that easily can be seen in the EPID images. The poor contrast of the EPID images motivated the researchers for the development of the kV and cone-beam CT.

4. Integrated kV imaging: this system include an X-ray tube with a-Si detector attached to the linac either orthogonal to the treatment beam axis (Elekta Synergy, Vero, Brainlab and Varian OBI) or along the treatment beam axis. The images are used for localization and patient monitoring in fractionated and hypo-fractionated treatment [87, 96]. These systems can generate 2D and 3D images to be matched with DRRs or volumetric images from the planned CT data. The principle of imaging of these systems is by scanning in either partial or continuous rotation around the couch/patient and imaging the average position of the organs and detecting internal organ motion. These scans are normally repeated at the end of the treatment session for estimates of intra-fractional changes. The images of the kV CT images have a better contrast than MV CT images, and the geometric accuracy is within 1 mm [87, 102-105]. Nevertheless, the images quality produced by CBCT is not of diagnostic quality but of suitable quality for visualising bones and soft tissue in some sites. Clinically, kV-CBCT can be used to image soft-tissue (i.e. prostate and lungs) directly without the use of implanted fiducial markers. The other drawback on this system is the imaging doses associated with acquisition time that ranging from 0.2-2 cGy per acquisition. The poor contrast caused by motion blur in the image due to long acquisition time and scattered radiation [96].

5. Fan-beam kVCT (CT-on-rails, Siemens) this system generates images of diagnostic quality images, similar to imaging systems used for treatment planning. The in-room CT-linac system sets on rails to allow for movement across the patient, while the patient stays still on the treatment couch in the treatment position. This modality enables image registration for CTV alignment directly as well as the use of the whole CT data set for adaptive replanning to take in consideration the interactional anatomy changes [81, 96]. The geometric accuracy of this system is ≤ 1 mm.

6. X-ray real-time tracking systems that are combined with infrared and 2D orthogonal kV imaging localization. These systems are designed to track the tumours by imaging the implanted fiducial marker within the treated target. These systems known as Hybrid systems and include:

   a) 2-D kV stereoscopic imaging or the Cyberknife system (Cyberknife, Accuracy) is used as a robotic radiosurgery system. A compact linac is attached to a robotic arm for radiation beam direction control, via an X-ray imaging system fixed in the treatment room ceiling with flat panel detectors fixed to the side of the treatment couch. The images are acquired during the treatment over a period of 5-90 seconds. Different tracking technologies can be used during the treatment. The cyberknife's couch can rotate with 6 degrees of freedom to allow for position changes [106, 107].

   b) Real-time tumor-tracking (RTRT) system was developed by Hokkaido University, school of medicine and Mitsubishi Electronics Company Ltd. This system has four camera systems fixed on the floor and an image intensifier fixed to the ceiling. The principal of this system is that, it images embedded fiducial markers within the target volume and uses the information for gating. Thus, the linac will be gated to deliver the beam when the markers are within the allowed planned location with respect to the isocentre as per the plan [108, 109].

   c) VERO system (BrainLAB/MHI), consisting of two X-ray systems with flat panel detectors attached. Patient alignment is performed using a pair of radiographs coupled with couch movement. The couch has 3D alignment capability to assist in the initial set-up. To verify any translational and rotation errors pre-treatment, images are acquired and matched with DRRs using the bone anatomy for matching and evaluation of these errors [81, 110].

d) Optical imaging and 2-D kV orthogonal imaging (ExacTrac-X-ray, BrainLAB) it is a stereotactic IGRT system uses the optical positioning and kV radiographs imaging for patient positioning and online corrections of the patient position. ExacTrac is infrared-based optical positioning system that is used to setup the patient in the initial treatment position via controlled couch movement (robotic couch); and for monitoring patient's respiration for gating of the treatment beam as needed during the treatment. The kV X-ray imaging system (X-ray 6-D) is used for patient position verification based on correlation between the tumor position and external fiducial markers. This system requires a calibration procedure before it is used to allow for accurate anatomic position determination via the infrared markers and kV X-ray. This calibration procedure is performed to link the ExacTrac system with the linac isocentre [81, 111, 112].

The second type of the IGRT systems is the non-invasive (radiation) imaging systems include ultrasound, camera-based, MRI, and electromagnetic tracking systems. The main advantage of these systems is their non-use of ionisation radiation.

1. Ultrasound uses 3D images in target alignment to reduce the inter-fraction setup errors. The disadvantage of this system is that images are of a poorer quality, and the geometric accuracy ranges between 3-5 mm. the most known commercially available systems include Clarity, BAT, iBEAM, and SonArray. The first in-room ultrasound IGRT (US) was used originally for prostate sites imaging but later on was used for abdominal and breast IGRT imaging [81, 113]

2. Camera-based systems (optical tracking systems) are used for patient surface–based localization. They are also used to monitor the inter-fraction motion. The main advantage of this system is the speed in addition to the use of non-ionising radiation. Geometric accuracy is ranging between 1-2 mm. There are two commercially available systems AlignRT (VisionRT, UK) and C-Rad Sentinel (C-RAD, Sweden). The Align RT system uses two cameras minimum for stereotactic imaging. The C-Rad system scans with one camera and laser system [81].

3. Electromagnetic tracking systems are used mainly in prostate treatment. They use electromagnetic transponders implanted inside the target volume to detect any motion in the target in real-time, where they can be tracked using array detectors. They are used to improve the setup accuracy as well. Geometric accuracy of this

system is < 2 mm. The most commonly available system of this type is Calypso (Calypso, Varian). The main components of this system are a mobile AC electromagnetic console, a receiver array, three infrared cameras attached to the ceiling, and a hub. This system is independent from the linac in the treatment room [81, 114].

4. Magnetic resonance imaging (MRI) systems are used in real-time imaging via continuous soft tissue imaging to evaluate any organ motion. They have a geometric accuracy between 1-2 mm. The images of this system are of low quality, caused by patient motion, magnetic susceptibility artefacts, and non-uniformity in the magnetic field. However, The enhanced soft-tissue contrast in MRI images in comparison with CBCT images is an advantage for imaging various treated regions such as abdomen and pelvic. Therefore, the ability to integrate this imaging system into radiation treatment delivery in the treatment room should improve accuracy of the escalated dose delivery to target volume.

2.9 MEGAVOLTAGE IMAGING USING EPID

The imaging process involves an X-ray source generating radiation that traverse through patient or phantom, and an image receptor to form the image from the X-ray fluence that reaches the image receptor. The MV images are formed using treatment beam of MV energy range generated by the linac. These images are usually compared with reference image (i.e. DRR, simulator image, and predicted MC image). Generally, the quality of MV images is inherently poorer than the X-ray kV images. The increase in the photon beam energy causes a decrease in subject contrast. There are other reasons for causing poor quality of the MV images such as the performance of the image receptor, X-ray scatter due to patient thickness (scatter increase is proportional to patient thickness), the X-ray source size, the noise in the human eye-brain system, and the position of the receptor [25]. There are a number of quantities used to characterise the quality of the portal image [25]:

Image contrast: this is the difference in attenuation between an object and its background. The contrast is a measure of the difference in X-ray attenuation within patient (i.e. the differential attenuation between bone or air and soft tissue). It can be simply expressed:

$$C = \frac{signal}{meanSignal} \qquad\qquad [2.2]$$

The subject contrast is determined by the x-ray beam energy, the radiological properties of the imaged subject and the how much x-ray scatter reaches the image receptor. The energy range of the x-ray beam affects the contrast of the image. At low energy beams travelling through patient, the photoelectric interactions are the dominant. The cross section of the photoelectric interaction is proportional to atomic number cubed and inversely proportional to the cubed energy. Therefore, larger attenuation coefficient in bone is due to higher atomic number in comparison with water or soft tissue. At high energies range, Compton scattering becomes the dominant interaction, above 20 keV for soft tissue and above 50 keV for bone. Compton scattering cross section dependency on the electron density of the medium, which changes slightly with the atomic number, explains the difference in attenuation, and thus the significant contrast reduction at MV energies range [25].

Signal-to-noise ratio (SNR): Two main sources contribute to the SNR of an image, quantum noise, and detective quantum efficiency. The quantum noise is due to the X-ray quantum statistics since the imaging process formation is a process involving the detection of X-ray quanta that reach the receptor and interact in it [25]. Detective quantum efficiency (DQE) is a measure of the efficiency of the imaging system in how it transfers information through the detector system [25]. DQE analysis determines the magnitude of noise contributed by the imaging system to the image [25]. Ideal imaging detectors have a high DQE in order to detect a large fraction of the incident X-ray beam that interacts with the image receptor [25]. Most commercially available portal imaging systems have relatively low quantum efficiency. These systems use a metal plate to convert X-ray quanta to Compton electrons, and a phosphor screen to convert the electrons to optical photons [25]. DQE increases with the increase in thickness of the metal plate, or of the phosphor screen due to the interaction probability of X-ray quanta with phosphor screens becoming higher with thicker screens [25]. Other sources of noise that affect the portal image quality includes the energy absorption noise, noise added by the imaging system, and noise in the human eye-brain system [25].

Background

Spatial resolution: measures the blur in the image that is caused by the imaging system [25]. It can be described and analysed by the point spread function, which examines how well the imaging system can reproduce a point object. This function can be expressed as a form of the modulation transfer function (MTF) which shows how well the imaging system can pass different spatial frequencies [25]. This is calculated using Fourier transformation of the point spread function. Spatial resolution is a factor affecting the image quality of the EPID images, and its effect depends on the size of the X-ray source, the spatial resolution of the image receptor, and the image magnification. Geometric blurring caused by the X-ray source increases with the increase of magnification; while the size of imaged anatomy projected at the plane of the image receptor increases, decreasing the effect of blurring produced by the image receptor. [25]. Finally, image magnification depends on the source object-detector distance. The MV portal images have a lower spatial resolution than diagnostic images due to the reduced attenuation of the high energies images in comparison with kV energies, which causes reduced sharpness of the imaged object and noticeable change in the projected object dimension [25].

X-ray Scatter: Adds noise to the image -reducing the object contrast and the SNR- by generating signals in the image receptor that do not carry any geometric information of the patient's anatomy [25]. This effect can reduce the contrast and the SNR of EPID images. X-ray scatter affects kilovoltage images, but has a lesser effect on megavoltage EPID images [8, 25]. The scatter element of the fluence reaching the receptor decreases with the increase of the incident X-ray beam energy. There are other factors that affect the scatter part of the X-ray fluence reaching the receptor in the megavoltage energies [25] including patient thickness where scatter increases with an increase of the thickness of the patient, field size, and as the air gap between the patient and the image receptor decreases scatter also increases .

EPID systems require some form of correction or calibration to generate a high quality image. Generally, background signals are subtracted from the EPID image to improve the quality of the image. Noise in the calibration images can affect or reduce the image quality, therefore, this noise should be minimised. Calibration procedures of the EPID comprises of exposing the EPID to radiation under certain conditions, following the

recommendation of the manufacturer. Generally, the most common EPID calibration procedures performed are:

1. Measurement of the dark current or acquisition of an EPID image with no beam to measure the signal present in EPID. Usually this image is acquired before and/or at the end of a treatment.
2. Acquiring an open field image to correct for pixel gain variations across the beam profiles.
3. Beam energy and field size calibration is performed by acquiring flood field images with the beam on. These are performed at different energies and dose rates.
4. Gantry angle calibration is performed to test the mechanical stability of the EPID to correct for any mechanical shift offsets in the calibration of a flat field, or significant changes to linac characteristics at various gantry angles.
5. Other parameters affecting EPID image quality, such as the scatter and attenuation caused by the patient thickness and detector distance should also be considered calibration parameters.

In this project, EPID images were corrected for flood field (the EPID's signal) automatically by Elekta's iView image acquisition software. In addition to the automatic correction via the software, a dark field image (electronic offset signal) was acquired at the end of each field's delivery. This image was subtracted from the raw image of the field to correct for pixel sensitivity variations in the EPID.

2.10 GEOMETRIC VERIFICATION USING EPIDS

The EPID can be used to acquire images to confirm the position of the patient by performing the imaging before or during the treatment. The patient position verification process involves matching the information in the EPID image and the information (i.e. the field edges and bone anatomy) in the reference image. Based on the results of image matching, the EPID image will be aligned to the reference image (landmark technique) [25]. The treatment field edge detection is also important in the set-up verification because it can be used as a coordinate system where a variation in the patient anatomy can be determined, [25] and to verify the shape and orientation of the treatment portal [25].

Background

Before the introduction of the latest imaging systems, geometric verification mostly used 2D images obtained using EPID at high energies (i.e. megavoltage). The field position and alignment set on the patient's body with skin markers could be verified with respect to the bone structure. Depending on the visibility and stability of the bone anatomy in EPID images for position verification.

The patient position is verified using online or off-line methods (described in section 2.8.1). Previous studies investigated both methods [25, 115-117]. They showed that when the online method was used for the patient set-up verification, the anatomical location error correction rate was dependent on the observers and their visual analysis. In addition, up to 50% of the initial fields used were found to be in error and required correction. When the offline method was used, the analysis showed that some residual set-up error remained [25, 115-117]. EPID images viewed before the treatment are known as *localisation images* and images viewed during the treatment to adjust the patient position/set-up are known as *verification images* [85].

IMRT patient set-up verification is usually performed either pre- or post-treatment, but not during the treatment, due to the modulations of the beam and intensity variation which masks the patient's anatomy [3, 31, 34]. Hence, it would be useful to use a calibration method to remove these modulations to outline the anatomy in the EPID images of the patient, allowing verification of IMRT to be possible during the treatment, so that set-up errors can be adjusted in subsequent fractions in the manner as using CRT and 3-D CRT. Once these images are calibrated they can be compared with the simulated reference image then set-up errors can be corrected to achieve a better outcome of the treatment.

In 2002, Fielding et al. [4] investigated the use of camera-based EPIDs for the patient position and set-up error verification process in IMRT [4]. The resulting IMRT EPID images from using a dynamic MLC delivery method were calibrated using a previously published calibration method. They successfully extracted images of patient anatomy by removing beam modulations. Those results showed the ability of the EPID images to be used in both dosimetry and setup-error verification.

2.11 DOSIMETRIC VERIFICATION USING EPIDS

The accuracy of the dose delivered to the target volume in radiotherapy is the main concern in IMRT treatment. This can only be achieved while keeping the geometric and dosimetric accuracy at its best. The dose delivered to the target volume needs to match the planned dose. Therefore, quality assurance procedures are used to detect dosimetric errors [118]. EPIDs are used as a replacement or alternative to film dosimetry, as shown by Chang, [119]. In 2008, Van Elmpt et al. carried out a review of the literature on radiotherapy treatment dosimetry [120]. This review showed that EPIDs became the preferred imaging device for patient positioning verification over the past decade. Moreover it has also became preferred for dosimetric verification, since EPID images also contain dose information [120]. There are some dosimetric errors encountered in individual IMRT beams calculated by the treatment planning system (TPS) caused by the lack of charged particle equilibrium in the small subfields and interleaf leakage of the MLC [118]. The International Commission on Radiological Units and Measurements (ICRU) report 24 (1976) and report 42 (1988), stated that the uncertainty criteria in the dose delivered to the target volume is 5%, which is translated into a standard deviation (SD) in the range of 1.5 – 2.0 [79, 121, 122]. Mijnheer (1987) reported uncertainty criteria of 3.5% and Brahme (1988) reported 3% uncertainty. Boyer and Shultheiss (1988) reported that a 1% improvement in dosimetric accuracy could improve the cure probability by 2% [122].

2.12 RESEARCH GAP

This project focuses on the current limitations of imaging during IMRT treatment using a-Si EPID. Currently, it is feasible to image the patient before or after treatment (to obtain useful anatomical information) but not during the IMRT treatment field delivery, due to the modulations in IMRT beam that mask the internal anatomy. Previous studies carried out by Fielding et al. [3, 4] used EPID images for verification of IMRT patient set-up using different delivery techniques for IMRT. It was shown that was feasible for measured images, but there were no reference image to compare them with (except 'the day-one' delivery image).Therefore, they recommended comparing those images with reference image either DRR or MC predicted portal image. They suggested the comparison between the images to perform systematic errors analysis for patient set-up

during IMRT. Previous researchers showed that systematic errors have crucial effect on the delivered dose to the cancer volume [45, 65-67]. In this project, to detect these errors MC predicted portal image is to be generated and used as a reference image instead of 'the day-one' delivery image they used in their study [3].

Set-up errors verification is an important part of radiotherapy. The evaluation of geometric errors is beneficial to ensure the accuracy and reproducibility of patient set-up [123]. EPID images usually are used to measure the set-up errors by verifying them against DRRs or simulator images. The increase in the geometric uncertainty can lead to reduction in the TCP and increase in the NTCP.

Van Herk et al investigated the effect of both random and systematic geometrical errors on the cumulative dose delivered to the target volume in terms systematic and random errors. It was found that a margin between the CTV and PTV is required of 2.5 times of the total standard deviation (SD) of systematic errors (Σ) plus 0.7 times the total SD of the random errors (σ') [67].

$$2.5\Sigma + 0.7\sigma' \qquad\qquad [2.2]$$

Many researchers have investigated the evaluation of set-up errors in radiotherapy for various diseased sites (i.e. head, brain prostate, cervical). The EPID and other IGRT technologies images were used as verification images. These images in most of those studies were compared with DRR or simulator images using verification systems available within their departments. Based on the set-up errors evaluation results, Van Herk's equation was used to calculate the CTV-PTV margins in those studies [123-130].

Previous study was carried out to measure the inter-fractional and intra-fractional set-up errors in patients with head and neck or brain cancers receiving IMRT treatment [124]. The patients (7 patients) were imaged using kilovoltage imaging device (permenantly mounted on the gantry of Varian 21EX linac) before and after IMRT treatment 3 times a week. The inter-fractional errors were evaluated using daily images compared with reference image. The residual errors (from weekly correction protocols) and intra-fractional set-up errors were identified as the difference between post-treatment and pre-

treatment images. The set-up errors were evaluated using their in-house image registration software. They also investigated the inter-observer variation influence on the results, as well as the various registration techniques. Moreover, translational data were compared with rotational data to search for correlation. The results showed translational set-up errors from all the data ranged from $0 - 2$ mm in the right-left (RL), anterior-posterior (AP), and superior-inferior (SI) directions respectively. Residual error for the 5 patients with a weekly correction protocol was between $0 - 1$ mm,RL, AP, and SI. Intra-fractional translation errors were small, ranging from $0 - 1$ mm in the RL, AP, and SI directions respectively. In the sagittal and coronal views respectively, inter-fractional rotational errors were -1.1 ± 1.7 degrees and -0.5 ± 0.9 degrees, and intra-fractional rotational errors were 0.3 ± 0.6 degrees and 0.2 ± 0.5 degrees. No significant correlation was seen between translational and rotational data [124].

In 2009, another study was carried out to evaluate the inter-fractional set-up errors using daily electronic portal images (EPI) of IMRT in head and neck cancer patients. The CTV-PTV margins were calculated from the set-up errors evaluation as well. DRRs were used as the reference images compared with portal images by matching the bone anatomy landmarks. The systematic errors were calculated in the three directions, and were found to be less than 1 mm while the random errors were around 2 mm. The CTV-PTV margins varied from 3-4 mm. It was concluded that applying on-line protocols with contouring of the bony anatomy on EPI is important to decrease the systematic mean error in their patient group. Moreover, the suggested a weekly EPI in anterior-posterior (AP) and medio lateral (ML) directions, in addition to every two days EPI image in carino caudal (CC) direction would be useful to overcome the set-up errors [126].

A study by Kang et al was completed in 2010 on the accuracy of positioning for head and neck cancer patients using 2D and 3D image guidance to determine an optimised image guided set-up by comparing the set-up errors from both 2D and 3D images [127]. The patients (9 patients) were imaged weekly throughout the treatment. The orthogonal kV images were compared with DRRs (2d-2D) using bony anatomy. Then kV cone beam CT (kVCBCT) images were acquired, and compared with simulation CT images using translations on the same bony anatomy (3D-3D). These images were registered manually in both methods. Another set of kVCBCT images were acquired after treatment to evaluate the intra-fractional motion. The results of this study showed that daily manual

Background

2D-2D registration reduces positioning errors for mask- immobilized head and neck patients, whereas the 3D-3D registration adds a small improvement over 2D-2D registration.

Another study was published in 2015, to estimate the patient set-up uncertainty using BrainLAB Exatrac X-ray 6D system in image-guided radiotherapy to deliver optimal margin strategies. Patients with brain cancer (15 patients) were studied. Two images before treatment were acquired using the Exatrac X-ray 6D system for patient position verification and CTV localization. DRRs were generated by the 6D fusion software with position variations in both 3 translational and 3 rotational directions for the CT images. The set-up errors (systematic and random errors) were calculated using Van Herk's formula [67]. The CTV-PTV margins were calculated using Herk's and stroom et al [45, 67] equations. The results showed that global systematic errors were < 2 mm in all directions, while random errors were between $0.1 - 0.3$ mm. The safety margins of CTV-PTV were 0.5 mm and 2.6 mm laterally for Herk and stroom respectively. Carnio-caudal axis was 1.5 mm and 3.4 mm, and AP axis 2.3 mm and 3.9 mm. Hence, they concluded that daily X-ray imaging is important to evaluate the precision of treatment delivery to various anatomical regions [129]

Recently, a new study has investigated different treatment sites (brain, head and neck and prostate) to assess patient set-up error in three directions (x, y and z) and optimum treatment margin for IMRT using image-guided system [128]. This study collected and analysed data of 60 patients. CT simulator images were used as the reference images. The CTV and critical structure were contoured in these images with aid of MRI images registration and fusion. The treatment position verification performed using MV image guidance system attached to the linac (Oncor Expression, Siemens) and capable of acquiring 3D cone beam CT (CBCT). Verification images were acquired in the treatment position. These orthogonal MV planner images were compared with their corresponding DRRs reference images, using visible bony landmarks. The results of this study showed that for brain and head and neck sites, more than 90, 80 and 100% of the total image acquisitions were less than 3 mm in lateral, longitudinal and vertical. For prostate site, set-up errors were less than 3 mm in lateral, longitudinal and vertical. The calculated CTV-PTV margins were 3.4, 3.4, and 1.9 mm for brain, 3.5, 3 and 1.8 mm for H&N and

5, 4.6 and 4.5 mm for the prostate cases in the lateral, longitudinal and vertical directions [128].

Subsequently, this study aims to develop an imaging procedure for patient set-up verification that complements the currently available procedures, during IMRT using the calibrated MC IMRT EPID image as a reference image. Therefore, the investigations of this study starts with the simulation of IMRT fields (simple and clinical) as well as designed phantom (lung phantom), EPID and calibration phantom to calculate a MC predicted portal image. This MC image will be calibrated and used for comparison. (Chapter Four). The study will investigate further the simulation of complete IMRT field (head and neck and prostate plans). A simulated calibration images approach will be investigated for calibrating the simulated images of the simulated IMRT fields. The phantom position will be verified via clinical patient position verification software (iView) to match the calibrated IMRT EPID images with the calibrated MC image as a reference image (Chapter Five). Further investigation will be performed to investigate the sensitivity and accuracy of methods implemented in verifying the phantom position by analysing intentional translation and rotation errors introduced to measured images via the couch movement in the treatment room using the MC image as the reference image (Chapter Six). Qualitative and quantative analysis will be performed on the results, and a proposed imaging procedure of patient position verification for estimating the systematic errors of patient set-up will be detailed (Chapter Seven).

Chapter 3:   Monte Carlo Techniques

3.1   INTRODUCTION

Monte Carlo (MC) techniques are a statistical simulation method based on the use of random numbers to sample probability distributions that describe a process [92]. The radiation transport process is a good example of a problem to which MC techniques have been applied. MC uses the probability distributions describing photon and electron interactions with the medium they are travelling through. It has the ability to track particle interactions travelling in a medium [93]. Available MC codes determine the probability of individual photons and charged particle interactions using models of the basic laws of physics [20]. Systematic errors should be taken into consideration here

since increasing the number of particles makes systematic errors more dominant, because they reduce (some) random errors. The only drawback with all available MC codes is that the larger the number of the particles simulated, the longer the computational time needed. Therefore, the real challenge with MC is modelling as accurately as possible using a smaller sample with fewer particles [20].

There are a number of general purpose MC codes available for radiotherapy modelling and simulations of radiation transport [20] including Geant4 [131], Monte Carlo N-particles (MCNP) [132], Peregrine [133], and EGSnrc Code [134]. The most commonly used MC code in radiotherapy is the EGSnrc (electron gamma shower) code. MC code has been found to be the gold standard technique for dose computation in radiotherapy [20]. The long computational time of MC could be overcome in future with the continuous improvement in computers and information systems technologies. The latest version of the EGS – EGSnrc [5] code – was used in this research along with its associated user codes BEAMnrc and DOSXYZnrc [6, 7].

3.2 ELECTRON GAMMA SHOWER MULTI –PLATFORM SYSTEM

Historically, the EGS code system for Monte Carlo simulation of electron and photon transport began as a high-energy physics tool. EGS was developed at the Stanford Linear Accelerator Centre (SLAC) by Richard Ford and Ralph Nelson in the mid-1970s. The first version of this code was the EGS3 code in 1978 [134] . EGS3 was created as a package to simulate electron and photon transport in different geometries at energies from a few KeV up to 1 MeV. The need to upgrade EGS3 came as a result of demand for simulating higher and lower energies of photons and electrons than those possible in EGS3 (i.e. 1 to 10 keV) [134]. During the 1980s the National Research Centre, Canada (NRC) and SLAC collaborated to upgrade the EGS3 code to make it work in the energy ranges of interest. EGS4 code is the new version of EGS3, and made available for medical physics research [91, 134].

EGS code is a structured set of subroutines that handles all of the physics in a simulation in a manner that allows users to write their own geometry and scoring routines [91]. The main feature of EGS4 is to simulate the radiation transport of both electrons and photons and their interactions with matter. The main interaction types that generate energy

deposition in a medium and recognised by radiotherapy have been considered and simulated in the EGS4 code. These interactions and processes are bremsstrahlung production, positron annihilation, Moliere multiple scattering, Moller (e- e-) scattering and Bhabha (e^+ e-) scattering, pair production, Compton scattering, and photoelectric effect [134, 135].

Since 1985, many enhancements and improvements have been implemented in EGS4, including physics modelling, development of new tools and techniques, systems and support issues, and timing and benchmark database issues. All of these developments have been summarised by researchers between 1985 and 1994. Since EGS4 was released, the number of research projects and publications using the code have greatly increased (i.e. >1000 papers) [135]. Many researchers have contributed to the improvement of EGS4 [134]. Following the improvements, the National Cancer Centre, Canada, introduced a new version EGSnrc.

3.3 RADIOTHERAPY MODELLING

3.3.1 BEAMnrc

BEAMnrc is a user code that allows the geometry of a Linac to be modelled. In 1995 the BEAM code was released for general use, and it has become widely used for many research purposes.[91]. Rogers and other researchers in Canada at the National Research Council (NRC) released this code. It was advanced as part of the Omega project to develop 3D treatment planning for radiotherapy (with the University of Wisconsin) [91]. BEAMnrc is designed to model the linac's head geometry, where a modular approach is used to simulate each component in the head of the linac. Simulation results of the head geometry are stored in an output data file known as the "phase space file". This file includes all the information about the particles (histories) used in the simulation; and where each particle has interacted in the linac at certain plan stages. The phase space file can be used in further beam calculations as an input file to DOSXYZnrc software to determine the dose distribution in a phantom or patient model. BEAMnrc can be used to model Co-60 units and diagnostic X-ray units as well as the linac [91]. The linac model used in this project is explained in the next section.

3.3.1.1 The linear accelerator model

The linear accelerator head geometry of the Elekta Precise linear accelerator was modelled in BEAMnrc in the method specified in the manufacturer's specifications document shown in Figure 3-1. All materials and geometries were modelled accordingly. All the phase space files from the BEAMnrc simulations were saved [6]. The linac model was commissioned to match the actual clinical linac at the hospital, operating at 6 MV. The commissioning procedure followed was described and used by previous researchers [136-138]. The percentage-depth-dose curves and the lateral profiles were calculated in a water tank using different square fields. A 10×10 cm^2 square was used as the reference field. These simulated results were compared with measured data until a good match was found. The initial electron mean energy matching the measured data was found to be 6.2 MeV. The commissioning details and results are shown in Appendix 1. BEAMnrc was used to simulate open square fields and in clinical IMRT fields (Chapter Four). The study progressed to simulate entire IMRT treatment plans of head and neck and prostate (Chapters Five and Six).

The beam source used in simulating the linac head geometry was ISOURC 19, a circular beam with 2-D Gaussian x-y distribution, parallel or with angular spread. The beam can either be parallel with direction cosines specified by the user, or it can have an angular spread from the z-axis, specified by a mean angular spread [6].
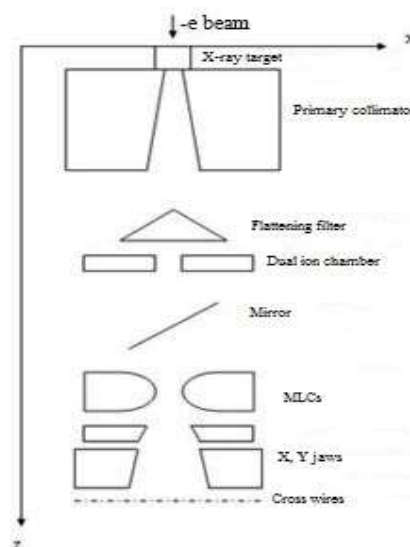
Figure 3-1: *The linac head geometry modelled in BEAMnrc.*

The number of histories used was 1 x 10^8 particles to minimise statistical uncertainity with directional bremsstrahlung splitting (DBS) with splitting field radius. Before using different DBS radii for each field size, all the simulations were carried out using splitting radii of 30 cm. Both results with 30 cm radii DBS and exact field size radii +3 cm were compared with respect to the simulation time and uncertainty in the results. The option with the exact field size DBS +3 cm was used since the results showed reduced uncertainty by 2-3% over the 30 cm DBS simulations, which indicates a more precise results using this option. The parameter Global ECUT at 0.7 MeV and Global PCUT at 0.01 MeV were used to save simulation time, where any particle energy below these assigned parameters was ignored and not tracked, and their energy deposited in the same region. All BEAMnrc simulations were run in parallel to reduce simulation time and to minimise uncertainty in the results, batches of 10 processes were run for each beam in each simulation. Phase space files resulting from each process for each simulation were summed. The linac head geometry modelling parameters used in BEAMnrc is shown in Table 3-1.

Table 3-1: *BEAMnrc parameters used in modelling the linear accelerator.*

Parameter	Parameter value / option	Parameter	Parameter value / option
Global ECUT	0.7	**Brems angular sampling**	Directional
Global PCUT	0.01	**Brems cross sections**	BH
Global SMAX	5	**Bound Compton scattering**	Off
ESTEPE	0.25	**Pair angular sampling**	Simple
XIMAX	0.5	**Photoelectron angular sampling**	Off
Boundary crossing algorithm	PRESTA-I	**Rayleigh scattering**	Off
Skin depth for BCA	0	**Atomic relaxations**	Off
Electron-step algorithm	PRESTA-II	**Electron impact ionisation**	Off
Spin effects	On		

3.3.2 DOSXYZnrc

DOSXYZnrc is an EGSnrc-based Monte Carlo user code for calculating dose distributions in a rectilinear voxel phantom, and is based directly on the DOSXYZ code developed for the EGS4 code system [91, 139]. DOSXYZ code was developed to

calculate dose distribution in a patient defined by a CT dataset. This code handles the complexities of the accelerator beam incident at any arbitrary angle [140]. DOSXYZnrc simulates the transport of photons and electrons in a Cartesian volume and scores the energy deposition in the designated voxel. A variety of beams may be incident on the phantom, including full phase-space files from BEAMnrc.

All runs in DOSXYZnrc used the same DBS radius used in the BEAMnrc simulations, and all the incident particles on all phantoms. The number of histories used in the simulations was different for each run in each study. All runs were performed in parallel in a batch of 10 processes. The output file of '3ddose' format was analysed for doses and profiles of axes, and for extracting the simulated images. The phase space files for each IMRT segment were used in DOSXYZnrc to simulate the above phantoms. An in-house matlab code was developed to combine the 3ddose files by summing all the single 3ddose files, as shown in Appendix 2 and Appendix 3. This code sums the dose distribution from each segment and saves it to the same format file (3ddose) to generate the simulated IMRT EPID image in the detector layer.

3.3.2.1 EPID and phantoms models

In this study, the Elekta iView GT a-Si EPID was modelled according to the manufacturer's specifications. All the layers of EPID, the materials densities, and thicknesses of the different layers were modelled accordingly using DOSXYZnrc. The nine materials used in modelling the EPID only were labelled in MC code as AIR700ICRU, LUNG700ICRU, ICRUTISSUE700ICRU, ICRPBONE700ICRU, CU700ICRU, AL700ICRU, Gadox (detector material), am-Si, and 170C700ICRU. The distance from the target to the surface of the EPID was 159 cm as shown in Figure 3-2. The images were calculated at the Gadox screen layer that was 160 cm from the target. The total active area of the EPID was 41×41 cm^2.

A lung, humanoid head, and pelvic phantoms were modelled in DOSXYZnrc. All the phase space files generated from BEAMnrc simulations were used in the input files for phantoms simulations in DOSXYZnrc. All these fields were simulated with exact gantry angles as per the measurements. The lung phantom was designed and simulated for this project. When simulating the humanoid phantoms the CT data was used in the simulation. The CT data was converted into 'egsphant' file format that was handled by CTCombine

code [141]. This output file is an ASCII file containing all the information needed for DOSXYZnrc to simulate the CT phantom and for the DOSXYZ_SHOW package to view the CT phantom. It contains information such as number of materials or mediums in the phantom and their names, number of voxels in X, Y, and Z directions, and their boundaries. Four materials were used in the input file of CTCombine were air, lung, tissue and bone. These materials were labelled in MC code as AIR700ICRU, LUNG700ICRU, ICRUTISSUE700ICRU, and ICRPBONE700ICRU. This code merged both the EPID model and phantom model together by combining both egsphant files into one file of the same format to handle gantry angle rotation in simulating the experimental system. The CTCombine code [141] was developed by the High Performance Computing Team at Queensland University of Technology, Brisbane, Australia. It handles rotating and combining CT data from an accurate detector model to simulate radiotherapy portal imaging at zero and non-zero beam angles. Therefore, this code works for simulating IMRT plans where the EPID and the CT phantoms together can be rotated at any gantry angle. This code solves the problem of rotating the gantry and EPID at the same time while keeping the phantom stationary. The CTCombine had been used in this project in Chapters Five and Six.
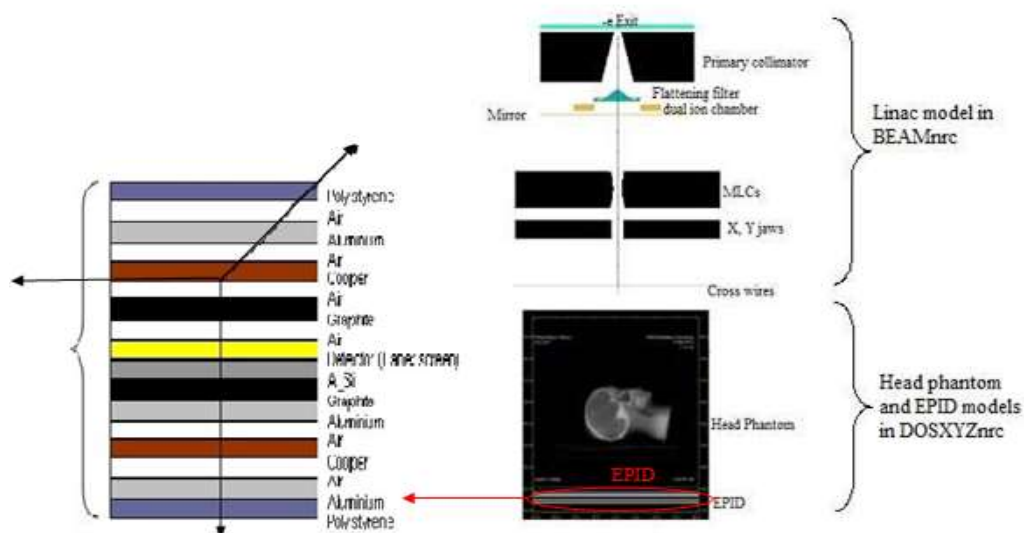
Figure 3-2: *Schematic view of the simulation process of the linac (BEAMnrc) and phantom containing the EPID model (DOSXYZnrc).*

Two different calibration phantoms geometries were simulated in DOSXYZnrc in this project:

1. The polymethyl methacrylate (PMMA) slabs with thicknesses corresponding to the humanoid phantoms (referred to from this point as PMMA calibration phantom) used in the measurements (Chapter Four and Study A in Chapter Five). The PMMA calibration phantom used in the experimental data collections was modelled in DOSXYZnrc. All these simulations were performed at zero gantry angle beam and 100 cm from the target to the isocentre. This phantom was used as the calibration phantom for revealing the lung anatomy (Chapter Four) and the bone anatomy of the pelvic phantom from the IMRT EPID image (Study A, Chapter Five). The images were calculated at the EPID with resolution of 256×256 voxels.

2. Modified CT data of the egsphant file (referred to from this point as modified pelvic/head calibration phantom). Two humanoid phantoms used head and pelvic phantoms as in Studies B and C in Chapter Five and Chapter Six. The CT data of the egsphant file of those two phantoms were edited by replacing the bone structure with a tissue equivalent structure to generate a uniform density material phantom, as shown in Figure 3-3. This was achieved by editing the egsphant files of the pelvic and head phantoms by modifying the CT data file. They were edited to replace the voxels within the phantom with tissue material (i.e. ICRUTISSUE700ICRU) and its corresponding density. A matlab code was developed for this purpose as shown in Appendix 6. The reason for using this phantom is generate a uniform density material (tissue equivalent) phantom for calibration has the similar shape and thickness as the phantom used in the simulations. The use of such phantom expected to work better for calibration. Moreover, the IMRT fields will be simulated using the same gantry and collimator angles as per the plans instead of delivering the fields from zero gantry angles as in the measurements when using the PMMA phantom.
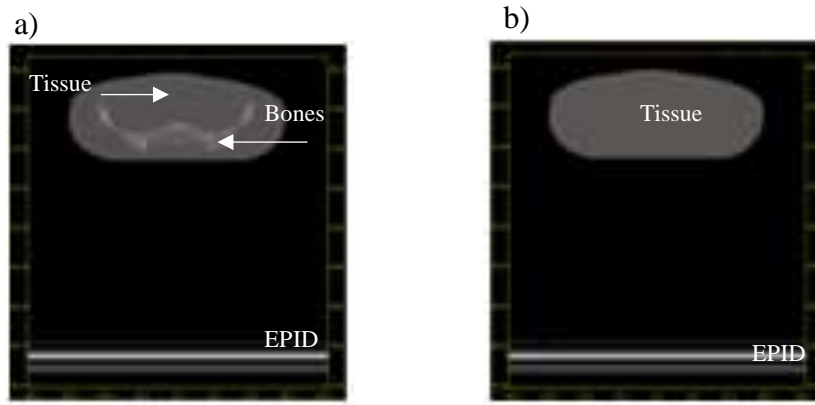
Figure 3-3: *a) Pelvic phantom containing bones and tissue structure view from the original egsphant file including EPID. b) The calibration phantom of the pelvic phantom view after modifying the original pelvic egsphant file where it is formed of uniform density.*

3.4   CALIBRATION OF THE SIMULATED EPID IMAGES

The resulting IMRT EPID images were calibrated to remove modulations that hide the bone anatomy within the phantoms used in this project. The calibration method used in this project had been described in detail in previous studies [142], and was applied by Fielding *et al.* for IMRT fields [3]. It is used to remove the intensity modulations from the IMRT EPID images. Measured pixel intensity at the EPID image plane is assumed a simple exponential function of the object thickness, it can be described mathematically:

$$I_{(x)} = I_o \times e^{-\mu t} \hspace{3cm} [3.1]$$

Where $I(x)$ is the measured intensity in the EPID image, $I_0(x)$ is the intensity for zero thickness of attenuator (open field), μ is the linear attenuation coefficient and x is the thickness of the phantom. This equation shows that the radiation intensity will decrease exponentially with the thickness of the phantom.

To reveal the bone anatomy that is masked by the modulation in the images, a simple division method is used to calibrate these images [8]. In this process, the IMRT EPID images generated in the detector layer in the EPID were calibrated by dividing them by a calibration phantom image (PMMA or uniform tissue equivalent phantom). This is shown in Equation 3-2, and Figure 3-4 explains the principle of this calibration method.

$$I_{MC\_calibrated} = \frac{I_{MC\_phantom}(x, y)}{I_{MC\_calibration\_Phantom}(x, y)} \qquad [3.2]$$
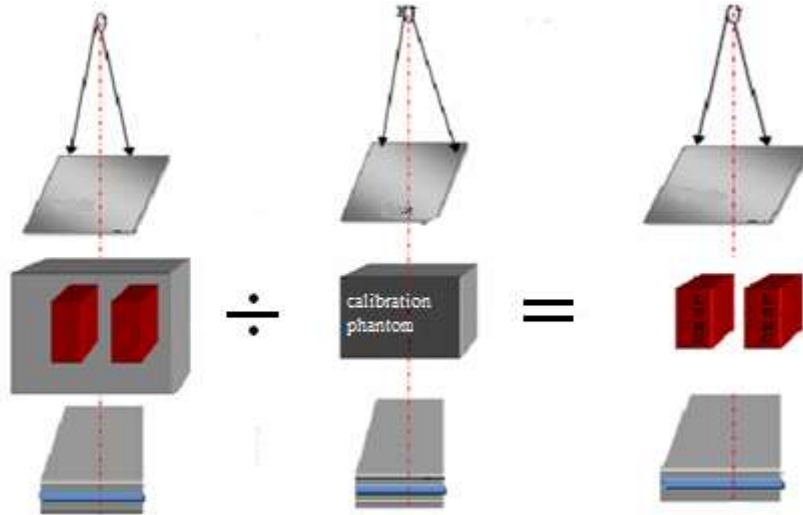
Figure 3-4: *Schematic diagram of the calibration geometry using the division calibration method procedure.*

3.5 MONTE CARLO PERFORMANCE

Despite the accuracy of MC techniques in predicting the dose distribution measurements and in modelling the linac head geometry, the long computational time remains a major drawback restricting clinical use and implementation of MC codes. There are various techniques adopted in MC user codes to reduce the computational time to increase the efficiency of its calculations. These techniques enable the reduction of the simulation times and/or reduce the uncertainties in the simulated results. These techniques are known as variance reduction techniques. They are used to improve MC efficiency (Equation 3.3)

$$\varepsilon = \frac{1}{S^2 T} \qquad [3.3]$$

Where T is CPU time and S^2 is an estimate of the variance for the quantity of interest. There are three main variance reduction techniques used in EGSnrc:

3.5.1 Range rejection

In this technique any particles with energies less than a threshold value that is assigned to these particles in the input file will be neglected and terminated, and their energy will be deposited in the same region. Some of these parameters used in EGSnrc and BEAMnrc are:

• ECUT: is known as the Global ECUT or the electron cut-off energy in MeV. If the electron energy is below the ECUT then it will be terminated and the energy will be deposited in the same region. The default value of ECUT is 0.7 MeV [6].

• PCUT: this is known as the global PCUT or the cut-off energy for photons in MeV. Usually the default value of PCUT used is 0.01 MeV.

3.5.2 Bremsstrahlung splitting

Using this technique can provide up to a four times improvement in the efficiency in MC calculations when modelling beams generated by linacs [5, 143]. When an electron interacts in the target, bremsstrahlung photons are produced with some of the electron's original kinetic energy.

The advantage of this technique is that photon sampling is faster. For example, when an electron interacts with the target in the linac, it produces a bremsstrahlung photon [144] . In the MC simulation this bremsstrahlung photon has a statistical weight $w = 1$ [144]. When more than one bremsstrahlung photon is generated, then each photon will have a splitting number (e.g. $N_{split} = 3$). Identical photons are created and each will have a weight of $w = 1 / N_{split}$ [144] as shown in Figure 3-5.
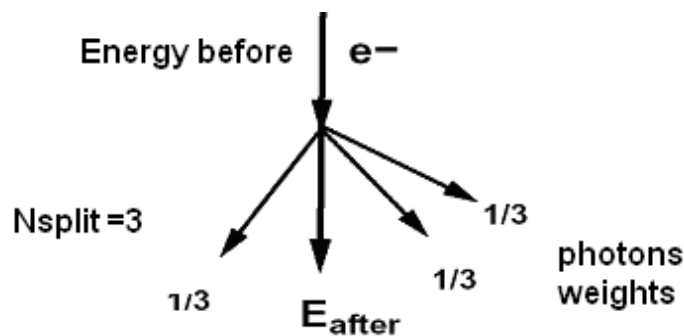
Figure 3-5: *Schematic illustration of electron interaction with the target and releases 3 photons at a splitting number =3. The photons are shown with their weights and energy.*

There are three types of bremsstrahlung splitting implemented in EGS4 and EGSnrc:

- Uniform bremsstrahlung splitting (UBS) [145]: as explained above, these photons are sampled as a constant with splitting number (i.e. N_{split}) which increase the probability of these photons reaching the ROI.

- Selective bremsstrahlung splitting (SBS) [146] : SBS is more efficient than UBS in MC calculations by a factor of 3 to 4 times. It differs from UBS by dealing with the splitting number (N_{split}) as a variable instead of a constant [146]. The splitting number will be a function of the direction (i.e. the angle between the central axis and the original electron $N_{split}(\theta)$) [144].

In this type of splitting, bremsstrahlung photons will be emitted in directions slightly different to the electron's original direction, so a smaller splitting factor $N_{split}(\theta)$ is used with a maximum factor at $\theta = 0$ and minimum factor at $\theta = 180$. The collimators absorb bremsstrahlung photons travelling at large angles. The calculation time in MC becomes longer when tracking these photons. The SBS reduces the calculation time due to fewer number of photons travelling with large angle, and calculates only the photons that have a higher probability of reaching the ROI [144]. There is one disadvantage for this type of splitting, which is the non-uniform distribution of statistical weights. The bremsstrahlung photons in a certain area will have different weights, which affects the efficiency gain of this technique by making it smaller than may be expected [144].

$$w(\theta) = \frac{1}{N_{split}(\theta)} \qquad\qquad [3.4]$$

- Directional bremsstrahlung splitting (DBS). The DBS was introduced into EGSnrc and BEAMnrc in 2004 [143]. This technique showed improvements in efficiency in MC calculations by a factor up to 8 times better than SBS and 20 times better than UBS [147]. It uses a constant splitting factor for the produced bremsstrahlung photons in the same way as UBS N_{split} where a complex algorithm analyses photon directions [144].

All the photons with a statistical weight of $w = 1/N_{split}$ and reaching the ROI will be calculated. The photons with $w = 1$ will not be calculated to reduce the calculation time by activating the Russian roulette variance reduction technique [144] which will be explained next. These photons, known as "fat-photons", are terminated because they are aimed outside the treatment field of interest [6, 144].

3.5.3 Russian roulette

This technique is considered the opposite to the particle splitting technique [144]. When it is used in MC simulation, the principle of this technique is that each electron or photon has a survival probability $P_{surv.}$ less or equal to 1. In MC simulations these particles will have a random number that will be sampled from a uniform distribution in an interval [0, 1], where this particle will survive if its random number probability is less than the survival probability $P_{surv.}$, but be discarded (i.e. killed) if it is larger than $P_{surv.}$ [144].

The surviving particle will have a statistical weight of $w = 1 / P_{surv.}$. Usually, this approach is used in conjunction with bremsstrahlung splitting [6, 144]. When bremsstrahlung photons are generated with $w = 1 / N_{split}$, they could have enough kinetic energy to reach the second collimator of the linac. These photons could interact with the collimator material via Compton scattering mechanism, which will lead to generating Compton electrons that have the same weight as the photons causing this event. Very often, these electrons are absorbed in the same region and do not reach the ROI, which means the calculation time for these electrons would be wasted. Therefore, discarding these electrons would reduce the simulation time performed using the Russian roulette technique. It can be turned on or off and by setting up the probability value.

3.5.4 Other techniques

There are further techniques used in BEAMnrc include:

1. Photon forcing: is used to force some photons to interact in a certain component module (CM) or region, to improve the statistics of photons interactions in the defined region.

2. Parallel processing: in this technique, simulations can be split into smaller jobs. Each job can be run on a separate processor in parallel. Monte Carlo simulations in the EGSnrc code can be run in parallel and the final results of each simulation combined at the end of

the runs [5]. As a result the elapsed time for any simulation is reduced which results in an increase of the efficiency [5].

3.6 **SUMMARY**

This chapter discussed the Monte Carlo method as a statistical method of random sampling that is based on probabilities. The MC method is used to describe the interactions of photons and electrons with matter.

The EGSnrc MC Code and its history were discussed, including the user codes BEAMnrc and DOSXYZnrc. The BEAMnrc user code was used to model the linac head geometry and DOSXYZnrc was used to calculate dose in model phantoms from CT and non-CT data. The linac model used in this project was discussed as well as the commissioning procedure. The EPID and the phantoms models were outlined and explained.

The uncertainties in MC can be reduced using different techniques such as using a large number of histories (particles) and using the parallel computing method to minimise statistical uncertainties and improve MC calculation efficiency. These different methods were used to reduce the calculation time to improve the efficiency. The variance reduction techniques used in these simulations were discussed.

Chapter 4: Simulation and calibration of Monte Carlo IMRT portal images

4.1 INTRODUCTION

IMRT has in recent years become the standard of care for radiotherapy treatments [19, 34]. High precision IMRT delivery makes patient set-up accuracy even more important than 3D CRT. The accuracy of the treatment field positon during the treatment ensures a precise dose distribution within the CTV. Hence, the detection of the field edges and certain structure (bone, soft-tissue) in the reference image and the treatment images is crucial for geometrical verification.

This chapter investigates applying the proposed calibration method that was detailed in the previous chapter on simulated IMRT images to detect the field edges and lung structure in the images. Therefore, a simple IMRT field and a clinical IMRT field were simulated using BEAMnrc. These fields were combined to simulate an IMRT step-and-shoot delivery [17, 18]. The linear accelerator head geometry of the Elekta Precise was modelled using the BEAMnrc code. The amorphous silicon (a-Si) EPID and the calibration phantoms (i.e. PMMA phantoms) were modelled using the DOSXYZnrc code. A model of a lung phantom was designed and simulated as well. This method was also extended to more clinical IMRT fields and model phantoms. The phantoms simulated in this study are shown in Figure 4-1.

The beams modulations caused by non-uniform intensities of the IMRT fields mask the anatomy in IMRT images acquired during the treatment. Thus, the calibration method will be tested to remove simple and complex beam modulations from the simulated IMRT EPID images. The lung anatomy is predictable to be visible in the calibrated image along with the simulated field shape and edges.

This chapter will be used as a proof of principle of MC code ability to simulate an IMRT fields using step-and-shoot delivery technique as well as predicted IMRT EPID images. Moreover, this chapter will be assessing the division calibration method of the simulated IMRT EPID images.
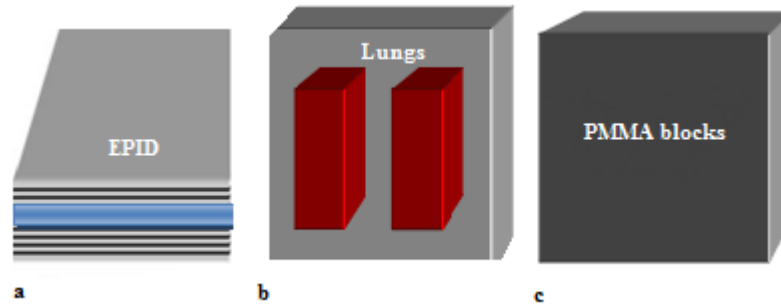
Figure 4-1: *a) Schematic view of EPID. b) Schematic view of the lung phantom. c) Schematic view of PMMA phantom (calibration phantom).*

4.2 METHODS AND MATERIALS

All the simulations in this study were carried out using the EGSnrc Monte Carlo code. As part of the EGSnrc code, the BEAMnrc and DOSXYZnrc codes were used to model the linear accelerator head geometry and the phantoms, including the EPID, respectively.

4.2.1 BEAMnrc simulations

4.2.1.1 The linear accelerator model

The linear accelerator head geometry of the Elekta Precise linear accelerator was modelled using BEAMnrc as directed in the manufacturer specifications document of Elekta and detailed in previous chapter. All the phase space files from the BEAMnrc simulations were scored at 52 cm from the source [6]. The model was commissioned using the methods that previous researchers used [137, 138]. The commissioning process is detailed in Appendix 1.

4.2.1.2 Open square field sizes simulations

A series of square field sizes were used in the simulation: 5×5, 10×10, 15×15, 20×20, and 25×25 cm^2. Each field size was run in parallel (to reduce simulation time) in batches of 10 processes, each with $5×10^7$ particles per batch. The smallest field size of 5×5 was assumed small enough (as IMRT segment) to prove the principle of generating simple IMRT field from these series of square fields. The phase space files resulting from each process were combined to reduce uncertainty in the results. The combined phase space files for each square field size were collected at the scoring plane. They were used later as input to the

DOSXYZnrc simulations. This procedure was used to generate a simple IMRT field by summing the different size square fields when simulating the phantoms in DOSXYZnrc. The individual 3ddose files were summed using an in-house matlab code (Appendix 2 and Appendix 3). Each simulated image was calculated in the model EPID.

4.2.1.3   Prostate IMRT field simulations

A prostate IMRT treatment field consisting of eight segments was simulated. Each of the eight segments had a different number of monitor units (MU), so the number of particles used for each segment was scaled depending on the MUs for each segment. The BEAMnrc input files were created using the Monte Carlo DICOM Toolkit (MCDTK) [148]. This software was developed to examine the accuracy of the radiotherapy dose calculations performed by the clinical TPS by comparing the TPS dose results against MC simulations of the treatment. One of the main capabilities of this software is the generation of BEAMnrc input files from imported DICOM format files from the radiotherapy plans [148]. The phase space files generated in BEAMnrc were later used in the DOSXYZnrc simulations for an open field with the EPID, PMMA, and a simple lung phantom.

4.2.2   DOSXYZnrc simulations (phantom modelling)

The EPID and phantoms used in this study were simulated using the DOSXYZnrc user code. The simulated EPID images were obtained in the detector layer. There were two simulated IMRT fields used with these phantoms: firstly, a simple IMRT field (open square fields) and secondly, a clinical IMRT field (prostate IMRT field)

4.2.2.1   DOSXYZnrc simulations with simple IMRT field

4.2.2.2   EPID simulations (Open field images)

The Elekta Precise iView GT a-Si EPID was modelled according to the manufacturer's specifications in DOSXYZnrc following methods that detailed in previous studies [91, 136, 138]. The EPID model has been discussed in the previous chapter. The same series of open square field sizes used in BEAMnrc and their phase space files were used in the simulations of the EPID. Each simulation used 3 billion particles; the same DBS parameters used in the BEAMnrc simulations for each field were used in DOSXYZnrc runs. All these simulations in DOSXYZnrc were performed with no phantom in the beam

for normalisation. In-house code (IDL version 6.3, Research Systems, Inc.) was used to read the simulation output 3ddose file to obtain the image from the detector layer Gadox screen in the EPID model. The dose was scored in the Gadox screen layer as an image of 168×168 pixels with a voxel width of 0.25 cm in the xy-plane. A simple step-and-shoot IMRT image was generated by summing the simulated images for the different size square fields using a matlab code as shown in Appendix 2 and Appendix 3.

4.2.2.3   PMMA phantom (calibration phantom) simulation

Eight uniform blocks of PMMA with dimensions 30 x 30 x 3.8 cm with a mass density of $\rho = 1.17$ g cm^{-3}, were modelled in DOSXYZnrc, as shown in Figure 4-2. The simulation procedure in the previous section was repeated for different thicknesses of PMMA. The PMMA phantom was set-up isocentrically. The thickness of PMMA for the eight simulations was 3.8 cm, 7.6 cm, 11.4 cm, 15.2 cm, 19 cm, 22.8 cm, 26.6 cm, and 30.4 cm. The reason for simulating different thicknesses of the PMMA was to compare the doses in different thicknesses to find the best corresponding calibration phantom thickness that corresponds to the lung phantom thickness (30 cm). The image of the 30.4 cm thick PMMA phantom thickness (eightblocks of PMMA) was used as the calibration image.
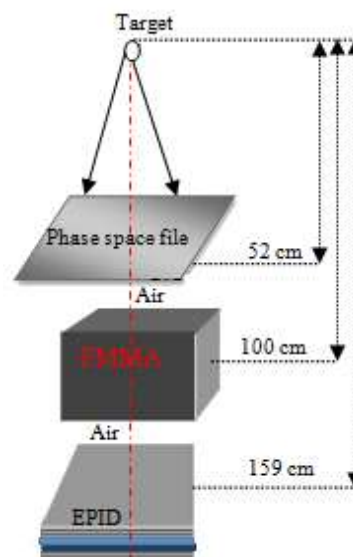
Figure 4-2: *Schematic diagram for open field image acquired in the detector for PMMA phantom of 30.4 cm thickness.*

4.2.2.4 Model lung phantom simulations

A phantom with dimensions 40 x 40 x 30 cm filled with tissue equivalent material with mass density = 1 gcm^{-3}, and two lung equivalent volumes with a mass density of = 0.26 gcm^{-3}, was modelled in DOSXYZnrc as shown in Figure 4-3. The phantom was modelled in an isocentric set up. These simulations were performed in DOSXYZnrc, and the phase space files generated in BEAMnrc for the same series of square fields as in Section 4.2.1.1. The EPID image of each field was calculated in the model detector. The summed image was again generated by combining the 3ddose files as in Section 4.2.3.1.
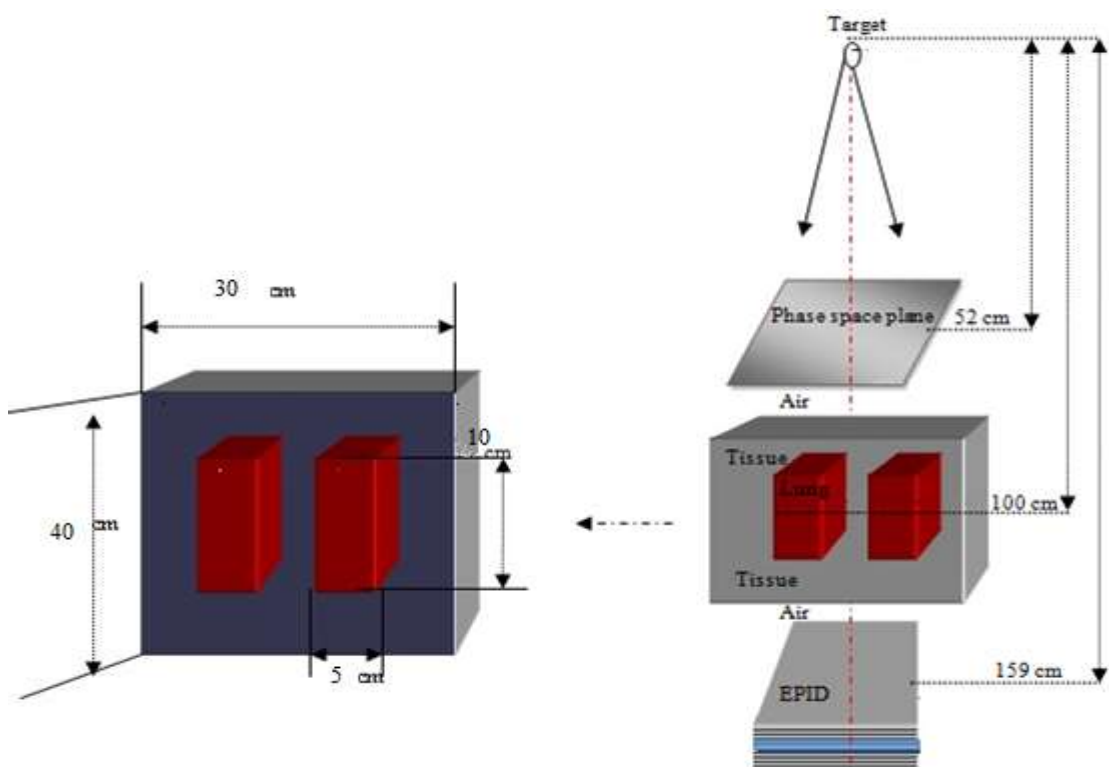
Figure 4-3: *Schematic diagram for open field images acquired in the detector for the lung phantom.*

4.2.3 DOSXYZnrc simulations with a clinical IMRT field

The procedures described in Section 4.2.1.3 were performed to calculate phase space files for a prostate IMRT treatment. The prostate IMRT field was modified to be simulated on the central axis at zero gantry angles rather than the treatment beam angles, in order to

maintain the uniform thickness of the calibration phantom that corresponds to the pelvic phantom thickness. The phase space files were used as input files for DOSXYZnrc. The number of particles used in these simulations was scaled as in the BEAMnrc simulations depending on the individual monitor units (MUs) for each segment. The total number of the MUs for the field was 51 MU. This simulation of the IMRT field was performed on the modelled phantoms used in the previous Sections 4.2.2.3 and 4.2.2.4 (PMMA and lung phantoms), and the simulated EPID images were calculated. The images simulated in DOSXYZnrc were, the IMRT EPID images without a phantom in the way of the beam for normalization, the calibration images, and the images of the lung phantom.

4.3   CALIBRATION OF THE IMRT EPID IMAGES (DIVISION METHOD)

Following the simulations of the linac and the phantoms (lung, PMMA and EPID), the EPID images was calculated. These simulated images were calibrated following the procedure explained in Section 3.2.3. The PMMA calibration phantom approach was used in this chapter to calibrate these simulated images of the lung phantom.

The simulated IMRT EPID images of the model lung phantom resulting from using both simulated IMRT fields (simple and clinical fields) were calibrated using the division calibration method (pixel-by-pixel). These two images were displayed and the contrast was enhanced in these images using matlab to show a clearer lung anatomy in these images.

4.4   CONTRAST EVALUATION

The contrast (C) in the simulated images (simple and clinical IMRT EPID images) after calibration was calculated to assess the effect of the calibration method on the image contrast. The procedure used in the contrast evaluation was the same procedure used in previous EPID studies (T. Kairns et al. 2010; Flampouri, et al. 2005; Roberts et al. 2008) [149]. The following equation was used:

$$C(x,y) = \frac{I_L(x,y) - I_T(x,y)}{I_T(x,y)} \qquad [4.1]$$

Where, $I_L(x, y)$ is the mean intensity value at the ROI in the lung in the EPID image. $I_T(x, y)$ is the mean intensity value at same region of interest in the tissue outside the lung. The ROI area was chosen as 3×3 pixels in lung and tissue. Figure 4-4 shows the model lung

phantom and the region of interest was used to calculate the contrast in the simulated images. The mean value of the pixels was calculated. The contrast of the calibrated images of simple and clinical IMRT fields was compared with the 25×25 field image of the lung phantom.

Figure 4-4: T*he model lung phantom showing the region of interest (black square) used to calculate the contrast before and after calibration in the simulated images.*

4.5 RESULTS

4.5.1 Open square field simulations images

1. EPID simulations (open field images) images

The individual simulated EPID images are shown in Figure 4-5 (a, b, c, d, e). The IMRT image resulted from combining these square fields is shown in Figure 4-5 (f).
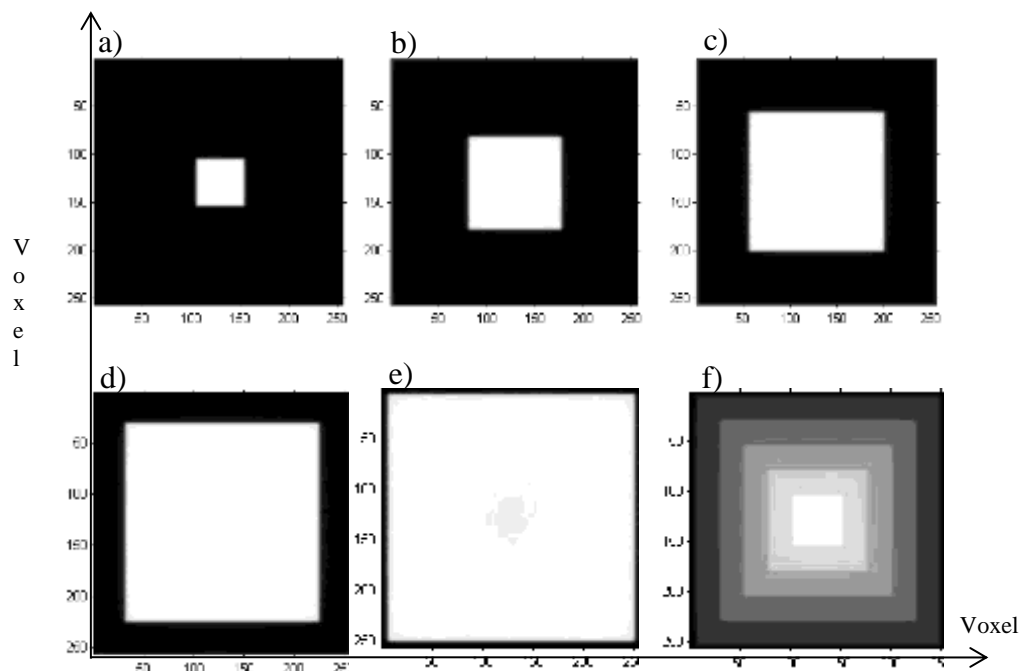
Figure 4-5: *The simulated EPID image of each square field size used to generate the simple IMRT field: a) 5×5 cm^2, b) 10×10 cm^2, c) 15×15 cm^2, d) 20×20 cm^2, e) 25×25 cm^2.and f) The resulting IMRT EPID image.*

2. PMMA phantom simulations images

The square fields were simulated and the simulations were performed on the modelled PMMA phantom. The simulated EPID individual images and the simulated IMRT image are shown in Figure 4-6 (a, b, c, d and e). The simple IMRT EPID image (calibration image) generated from combining the square fields is shown in Figure 4-6 (f).
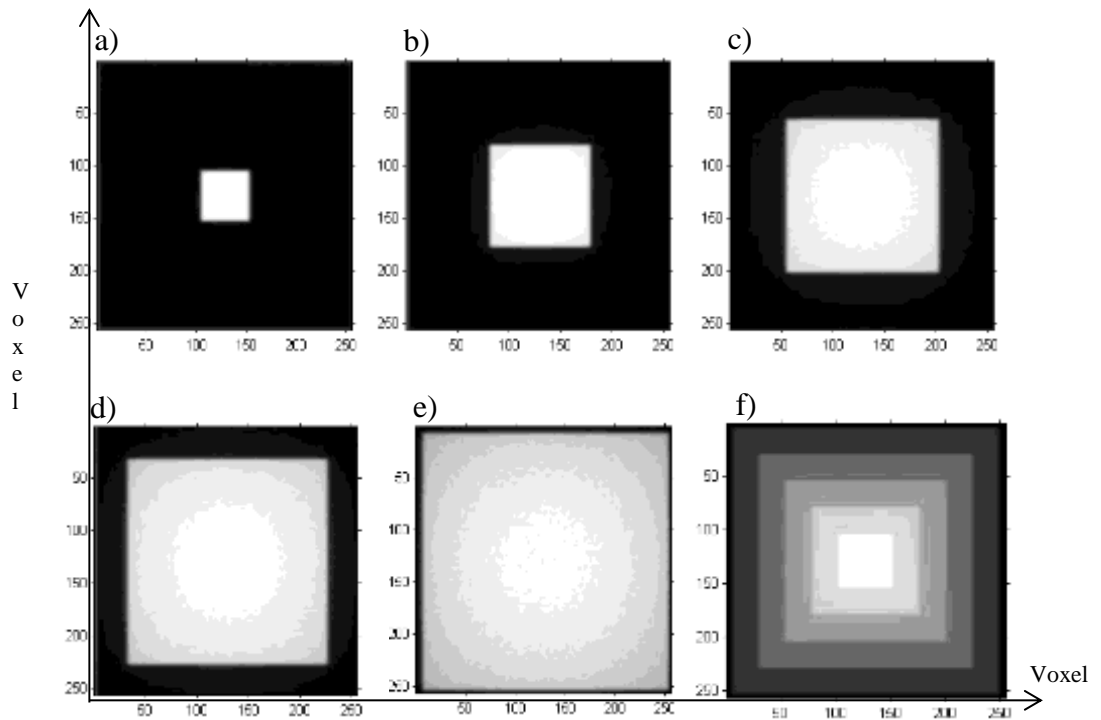
Figure 4-6: *The simulated image of PMMA for each square field size used to generate the simple IMRT field. a) 5×5 cm², b) 10×10 cm², c) 15×15 cm², d) 20×20 cm² , e) 25×25 cm² and f) The resulting IMRT EPID image.*

3. The model lung phantom simulation images

The simulated EPID images and the simulated IMRT images of each field are shown in Figure 4-7 (a, b, c, d and e). The generated IMRT EPID of the model lung is shown in Figure 4-7 (f).
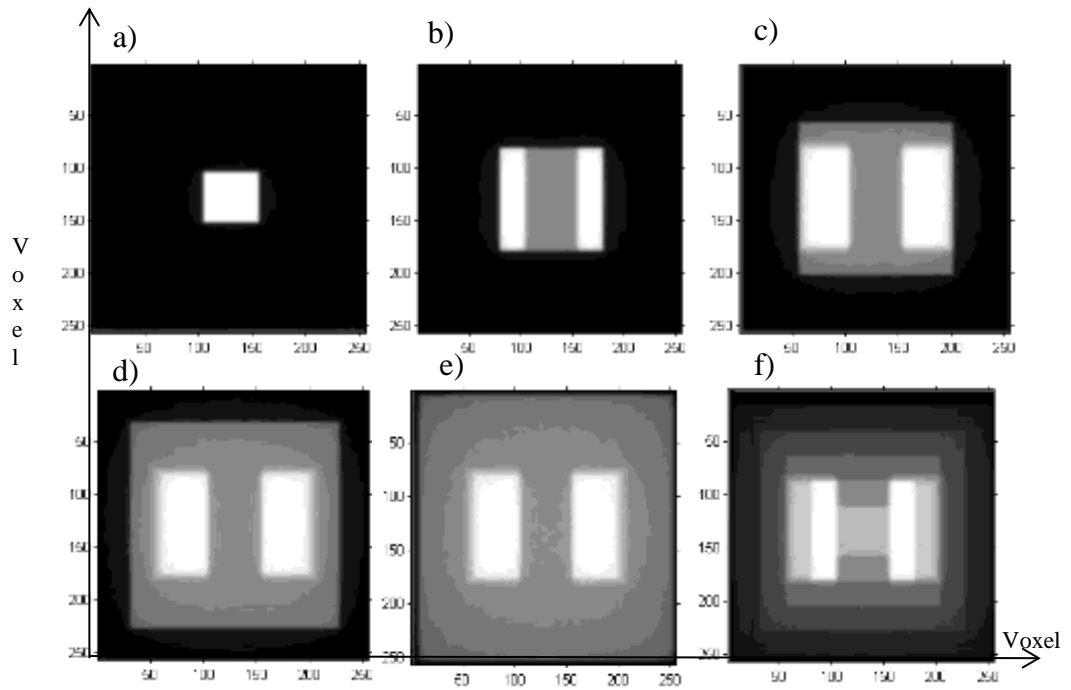
Figure 4-7: *The simulated EPID image of each square field size used to generate the simple IMRT field image using the square fields for the model lung phantom. a) 5×5 cm², b) 10×10 cm², c) 15×15 cm², d) 20×20 cm², e) 25×25 cm² . f) The resulting IMRT EPID image.*

4.5.1.1 The calibration of the simple IMRT field image

After generating the simple IMRT EPID image of the model lung phantom and the IMRT EPID image of the calibration phantom (PMMA), the model lung phantom image was calibrated using the division method (pixel-by-pixel). This simulated IMRT EPID images of the model lung phantom before and after calibration are shown in Figure 4-8.
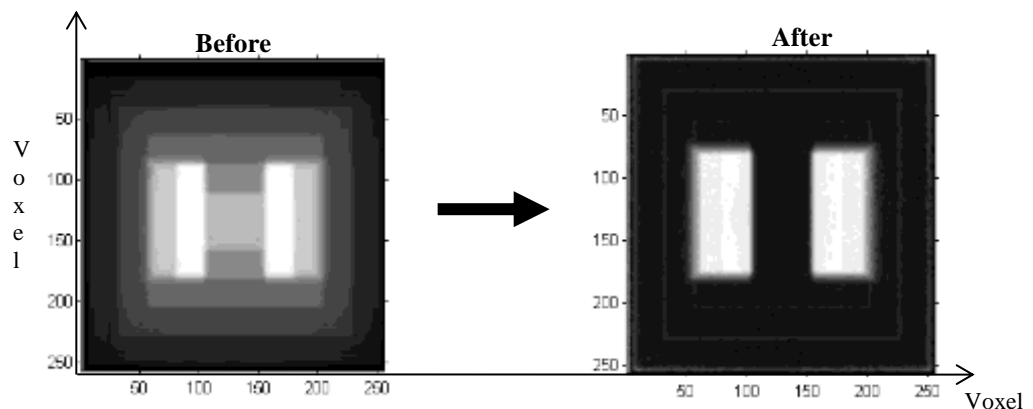
Figure 4-8: *The IMRT EPID image of the model lung phantom before and after calibration.*

4.5.2   Clinical IMRT fields

The same simulation and calibration procedures followed for simple IMRT fields were applied to the case of a more clinical IMRT field. The clinical IMRT field was used here as a proof of principle of the simulation and calibration method for more complicated field. The EPID images for these simulations were:

1. The PMMA phantom simulations

The simulated individual segments EPID images of the prostate field are shown in Figure 4-9. The segments phase space files were used in the input files of DOSXYZnrc for simulating the model lung phantom and PMMA as shown in Figure 4-10 (a, b).
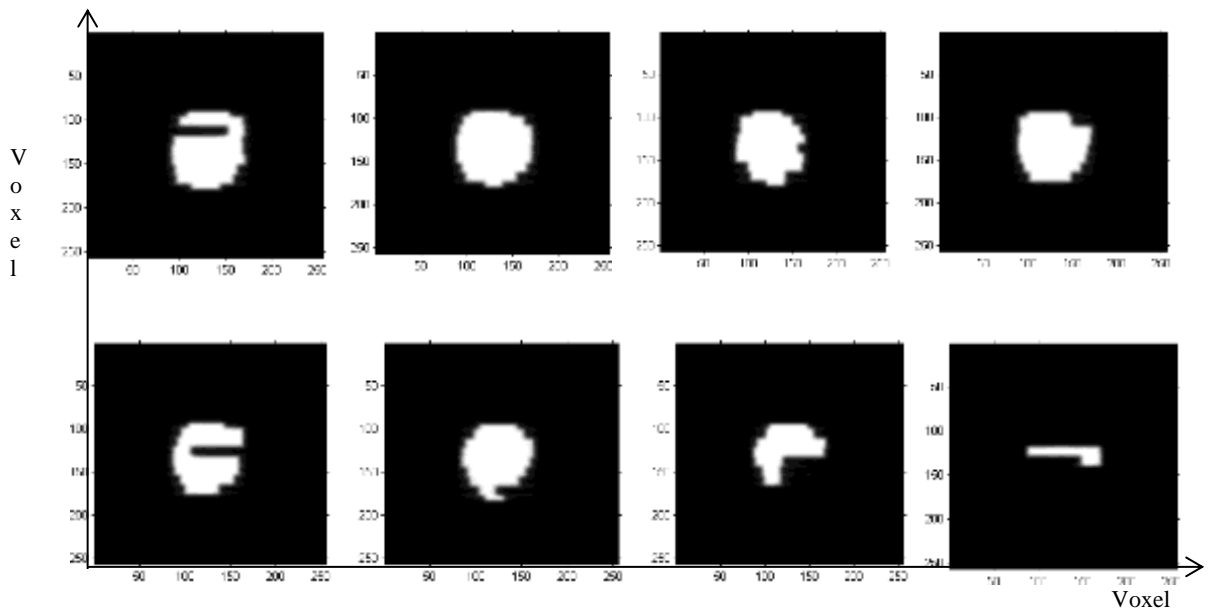
Figure 4-9: *The simulated IMRT field images of all the segments of the PMMA phantom.*

2. *The model lung phantom simulation*

The simulated EPID images for the individual IMRT segments were combined together to form the simulated IMRT EPID image before calibration by summing the dose distributions in the detector layer resulting from simulating each segment as shown in Figure 4-10 (a, b).

4.5.2.1   The calibration of the clinical IMRT field image

The simulated IMRT EPID image of the model lung shows no distinct lung anatomy as shown in Figure 4-10 (a), due to beam modulations. To show clearer lung anatomy in the image, beam modulations were removed from this image using the calibration method.

Figure 4-10(c) shows the calibrated simulated IMRT EPID image, which shows the IMRT field edge and visible lung.
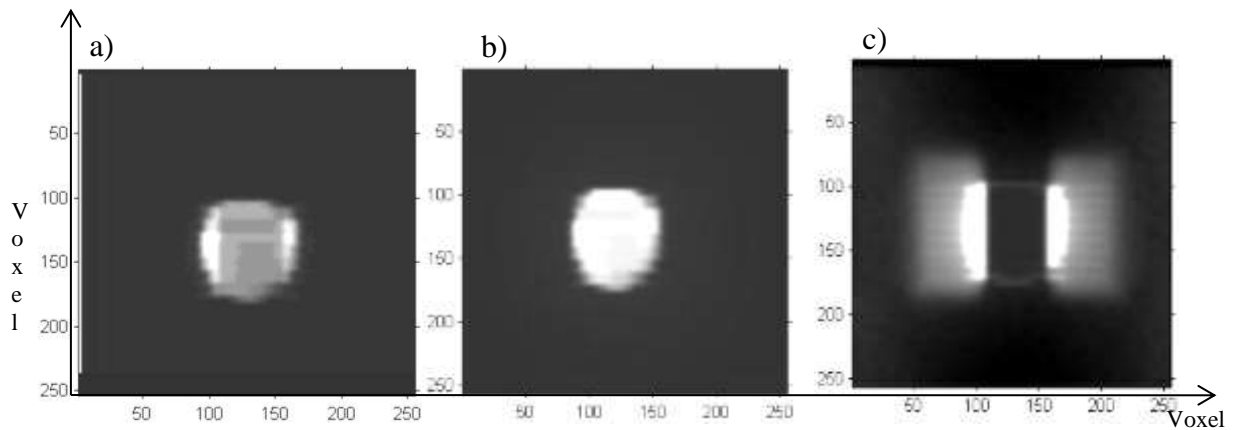
Figure 4-10: *a) the simulated IMRT EPID image of the simple model lung phantom before calibration. b) The simulated IMRT EPID image generated of the PMMA phantom (calibration image). c) The calibrated simulated IMRT EPID image of the model lung phantom.*

4.5.3 Contrast results

The contrast was calculated in the 25×25 cm^2 field as the reference image for comparing the results of the contrast of the lung in the *calibrated simulated IMRT EPID* images of the simple and clinical IMRT fields shown in Table 4-1. These images in Figure 4-11 show the regions in lung and tissue used to calculate the contrast.

Table 4-1: *The contrast results for each image calculated using equation 4-1.*

Image	contrast
Open field image 25×25 cm^2 (reference)	0.72 ± 0.67
Calibrated simple IMRT field image (square fields)	0.54 ± 0.33
Calibrated clinical IMRT field image (prostate)	0.51 ± 0.07
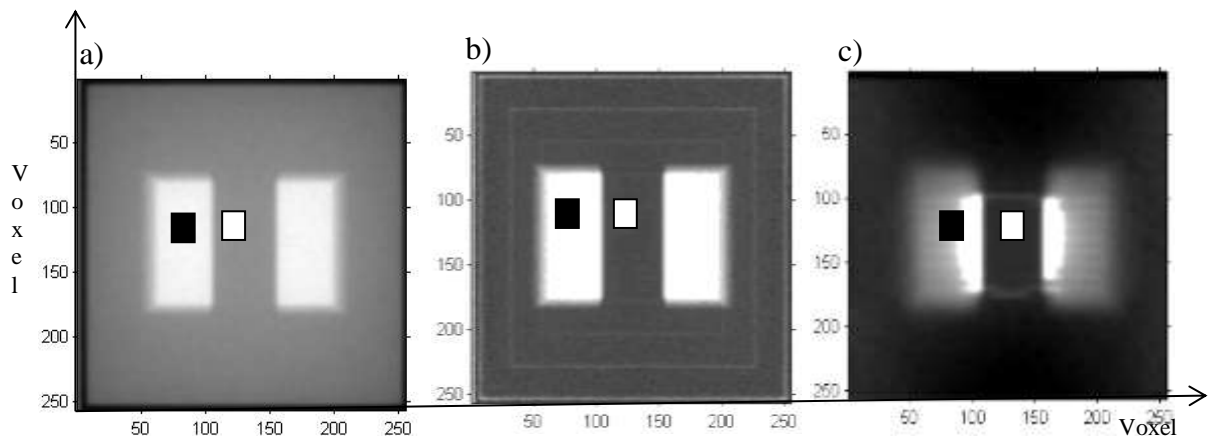
Figure 4-11: *The images used to calculate the contrast. a) The open field image of 25×25 cm² (reference image). b) The calibrated simulated IMRT EPID image of the simple IMRT field of the model lung phantom. c) The calibrated simulated IMRT EPID image of the clinical IMRT field (prostate) of the model lung phantom. The filled regions black are where the I_L calculated in the lung, and the white filled region where the I_T was calculated in the tissue within the field.*

4.6 DISCUSSION AND SUMMARY

This chapter investigated as a proof of principle the ability of MC EGSnrc and its associated user codes, BEAMnrc and DOSXYZnrc, to simulate two IMRT fields using the step-and-shoot delivery technique. The IMRT EPID images were simulated and generated by summing the dose distributions of the individual segments of the simple IMRT field (square fields) and the clinical IMRT field (prostate field with eight segments) in the detector layer, as explained in the previous chapter.

Firstly, the simple IMRT field EPID image was generated as shown in Figure 4-7(f) of the model lung phantom. The simulated image shows that when the square fields of uniform intensities are summed to generate the IMRT simulated image, the modulations of the beams have masked the lung anatomy in the model lung phantom. Therefore, this image was calibrated to remove these modulations and reveal the lung anatomy in the image. The calibrated image in Figure 4-8 shows that the calibration method has removed these modulations and the lung anatomy is visible.

Secondly, the clinical IMRT field (prostate field) was simulated and the IMRT EPID image of the model lung was generated and calibrated following the same procedures. The image before and after calibration is shown in Figure 4-10 (a, c). The lung anatomy in the

uncalibrated image was masked by beam modulation. In addition to beam modulation, the small prostate field simulated covered only part of the lung anatomy in the model.

The contrast was evaluated in the calibrated images and compared with the contrast of the open field 25×25 cm^2 image. The results in Table 4-1 showed that the contrast in the simple and clinical IMRT image had decreased slightly in comparison with the reference image contrast of the open field image. The contrast of both calibrated images was comparable with the reference image. The lungs anatomy in all the images are visible and of an adequate quality.

This work in this chapter and the results are only a proof of principle of the ability of MC code to simulate IMRT fields using a step-and-shoot technique and the calibration of the resulting IMRT EPID images. Both simple IMRT fields and clinical IMRT fields were simulated. These simulated IMRT EPID images showed that the anatomy covered by these fields is masked due to beam modulations. Hence, there was a need to calibrate these images to remove the modulations to reveal the lung anatomy masked by these modulations. The division calibration method was used to calibrate these images. The calibration method worked for both simulated IMRT EPID images. The modulations have been removed from the simulated images and lung anatomy was then visible in both images. The field edge was seen in both images. Since reliable geometric verification requires a good quality reference image as well as a treatment image. Both images should be of an adequate quality to distinguish the field edges in addition to the surrogate structure (bone, soft tissue, or implanted markers). Three points should be clearly visible to be outlined on the reference image to match them with treatment image for detecting any set-up errors. The resulting images from this study show the lung anatomy after the calibration along with the field edges. Therefore, these images were of a reliable qualitative comparable quality to be used potentially as a reference image for geometric verification during IMRT. The lungs anatomy and the simulated fields are outlined in these calibrated images as shown in figure 4-12.
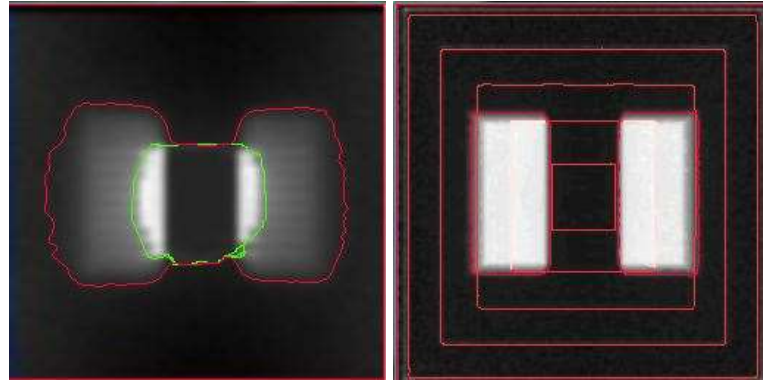
Figure 4-12: *The calibrated simulated IMRT EPID image of the lung phantom showing the lungs anatomy and the field edges outlined of the clinical IMRT field (left) and the simple IMRT field (right).*

The motivation behind the investigation in this chapter was to generate a calibrated simulated IMRT portal image to be used as a reference image for phantom/patient position verification during IMRT. This study in this chapter was performed just as a proof of principle. The next chapters discuss how more studies were undertaken to investigate and verify these results for a wider clinical IMRT plans and with different phantoms. This technique is to be implemented using more IMRT plans measured and simulated.

Chapter 5: Calibration of Phantom Measured and Simulated Treatment Intensity Modulated EPID Images for Anatomical Imaging

5.1 INTRODUCTION

This chapter investigated the use of the methods developed in Chapter Four for more complex IMRT fields and phantom geometries. The calibration method developed was applied to the measured and simulated images in this chapter. Moreover, this chapter investigated the use of the "modified calibration phantom" detailed in Section 3.3.2.1 for simulated images. The gantry angle effect on the simulated and measured calibrated images was investigated.

The studies in this chapter were carried out to develop a MC calibrated IMRT EPID image (further referred as C-simulated image). The MC images before calibration will be simulated. Once the simulated image calculated and the corresponding measured image obtained, both images will be calibrated. The phantom position will be verified using these calibrated images. The simulated image will be used as the reference image and the measured calibrated IMRT EPID image (further referred as C-measured image) will be matched with the simulated image using clinical geometrical verification software. The concern of these studies is to generate simulated and measured images of a quality that allows the geometrical verification during IMRT treatment using the C-simulated as the reference image.

The main motivation behind this study was to overcome the imaging difficulty during IMRT due to beam modulations masking internal anatomy (bones, soft-tissue) of the patient. The imaging of the patient is performed usually pre/post IMRT treatment for patient position verification. These images are usually matched with reference images (DRRs or simulator radiographers) of the patient immediately before the commencement of the treatment to ensure that the patient is in the reference position as per the treatment plan. To remove beam modulations from IMRT images, the calibration method detailed in Chapter Three will be used.

Five studies were carried out in this chapter. Studies A, B, and C concentrate on the ability of the MC code to generate a simulated image that will be calibrated and used as a reference image. This C-simulated image will be analysed and processed to demonstrate the ability to develop a quality image that shows the bone anatomy (landmarks) and the field shape and edges in the imaged area of the phantom. Studies D and E will be performed to investigate the effect of gantry angles on the C-measured image quality. The C-measured image will be obtained using the division calibration method. The calibration image will be acquired during the delivery of the IMRT field into more phantom-like calibration geometry (cylindrical solid water phantom). The IMRT fields will be delivered to the calibration phantom as per the plan, instead of zero gantry angle as in study A, B and C.

5.2   MATERIALS AND METHODS

This chapter investigated five studies involved both measured and simulated work. Study A involved delivering a prostate 6 MV IMRT field to a pelvic phantom. The same field was delivered to a PMMA phantom for calibration. Study B involved the delivery of head and neck 6 MV IMRT fields to a head phantom and to the corresponding plastic water (PW) calibration phantom. Study C involved the delivery of a 5 field prostate plan to a pelvic phantom and PW calibration phantom. These three studies (A, B, and C) were investigated experimentally and were simulated using the EGSnrc code. Studies D and E investigated the delivery of a 6 MV IMRT field to a thorax phantom and a head phantom using two different geometry calibration phantoms (square slabs and cylindrical phantoms) of water/tissue equivalent materials. The reason behind the use of different calibration phantoms in the measurements was to investigate different uniform density calibration phantoms of different materials and geometries.

5.2.1 Experimental Measurements

All the studies involved the use of a Toshiba Aquilion/LB CT scanner to scan the phantoms (i.e. pelvic, head). All measured data fields in these studies were delivered using an Elekta Precise linear accelerator. The images were acquired using the a-Si EPID Elekta iView GT attached to the linac at 159 cm from the target where the detector layer (Gadox) was ~ 160 cm far from the target with a 41×41 cm^2 active area of the detector. All images

acquired were saved as raw images in .HIS (Heimann Imaging Software) format with header information of 100 bytes, 16 bit-unsigned integer array, and 1024×1024 resolution. A Matlab code was developed to read and display these framed '.HIS' format images (Appendix 4). All the images were averaged for the number of frames and corrected for the offset signal (dark image). There were three sets of images; firstly open field images (no phantom in the way of the beam), then a 25×25 cm^2 field using 6 MV photon beam was used to acquire an open field image as a reference field for flood field calibration later images. Finally a 25×25 cm^2 field was used to image the phantoms (pelvic, head, PMMA, and PW). Following is the detail of each study:

Study A: For this study pelvic and PMMA, calibration phantoms were used. The pelvic phantom shown in Figure 5-1 (a) has a physical thickness of ~ 27 cm. The phantom was scanned and the image dataset consisted of 379 slices with a 1 mm slice thickness. This phantom contained bone anatomy (density $\rho = 1.38–1.79$ g cm^{-3}) of the lumbar spine, sacrum, and pelvic as shown in Figure 5-1 (b). The bones are contained in a tissue equivalent material (density $\rho = 1.03$ g cm^{-3}) which also fills the phantom between the bone anatomy. The phantom was setup isocentrically on the linear accelerator couch, with the radio-opaque markers still attached as seen in the CT simulation. These markers were attached for the consistency and accuracy of the isocentre between the CT simulation and the linac. The calibration phantom used in this study was firstly the PMMA slab formed of seven blocks of PMMA. The thickness of each block was ~ 3.8 cm. The calibration phantom was designed to have a thickness equivalent to the radiological phantom thickness. Each of these blocks had a mass density of $\rho = 1.17 - 1.20$ g/cm^3, an electron density of $\rho_e = 3.65 \times 10^{23}$ e/cm^3, with an area of 30×30 cm^2. The pelvic and the calibration phantom were irradiated with 6 MV using a 25×25 cm^2 field. The field was delivered firstly with no phantom between the target and the EPID (open field); followed with an IMRT prostate treatment beam. The IMRT beam was planned for a prostate cancer patient with 11 segments with two control points for each segment, and varying numbers of monitor units as shown in Table 5-1. The IMRT field was delivered at zero gantry angles. All the measured images were acquired using the EPID at ~ 160 cm from the target.
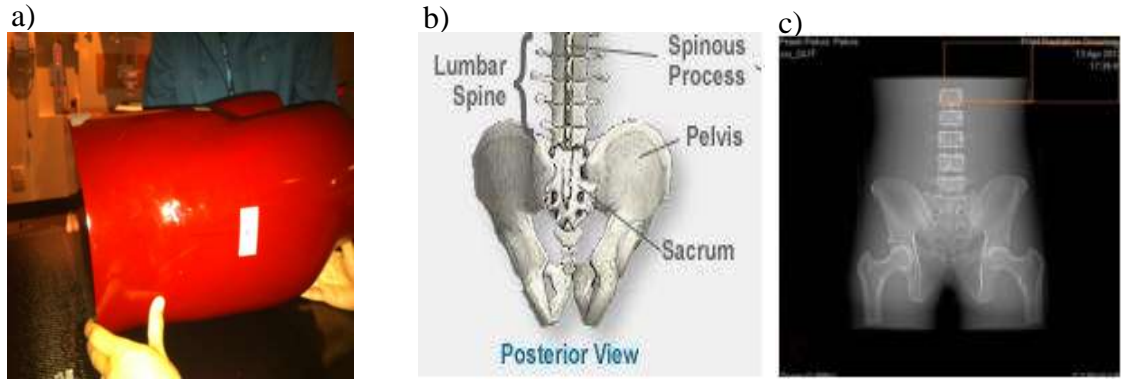
Figure 5-1: *a) The pelvic phantom used in study A. b) The anatomy inside the pelvic phantom. c) Scout image of the pelvic phantom.*

Table 5-1: *The prostate field delivery information.*

IMRT Beams	Monitor units	Gantry/Collimator angle ($\theta°$)
Segment 1	8	0,0
Segment 2	23	0,0
Segment 3	8	0,0
Segment 4	13	0,0
Segment 5	4	0,0
Segment 6	10	0,0
Segment 7	12	0,0
Segment 8	7	0,0
Segment 9	3	0,0
Segment 10	17	0,0
Segment 11	11	0,0

Study B: The same pelvic phantom from Study A was used. An IMRT prostate plan containing five fields was delivered to the pelvic phantom with 10 MV photon energy beam as well as to the calibration phantom. The pelvic phantom was scanned and the CT data of the phantom consisted of 159 slices with a 2 mm slice thickness. The calibration phantom used in this study was the PW slab (CNMC, USA). The PW phantom was chosen as a tissue equivalent material with thickness of 22 cm. Each of these blocks had a mass density of $\rho = 1.03$ g/cm^3 and an electron density of $\rho_e = 3.238$ x 10^{23} e/cm^3 with an area of 30×30 cm^2. The prostate IMRT fields were delivered to the pelvic phantom from different gantry angles. The same fields were delivered to calibration phantom at zero gantry angles to maintain the same thickness through

all measurements. The consistency of the calibration phantom thickness is important to be as close as possible to the depth of the pelvic phantom at the angle delivered for each field as the pelvic images of each field were divided by the calibration image. Hence, the zero gantry angles were used in the field delivery to the calibration phantom. The IMRT prostate field delivery information is shown in Table 5-2. A 25×25 cm^2 field using 10 MV energy beam was delivered firstly to the pelvic phantom.

Table 5-2: *The Prostate IMRT treatment images and delivery information for Study B.*

10X beam, prostate IMRT plan, 5 fields.				
Field	**# of segment**	**# of monitor units (MU)**	**Gantry (º)**	**Collimator (º)**
Field 1	12	87	100	285
Field 2	9	66	45	280
Field 3	9	61	0	90
Field 4	7	52	315	80
Field 5	11	83	260	75

Study C: The experimental materials and methods described in Study B were used in Study C. The differences study C used a head phantom shown in Figure 5-2(a) and the calibration phantom PW thickness was 20 cm. The head phantom was scanned with a slice thickness of 2 mm. The head phantom contains a human skull with a bone density $\rho = 1.4$–1.8 g /cm^3. The surrounding material was tissue equivalent with density of $\rho = 1.03$ g/cm^3. The IMRT plan used in this study was a head and neck IMRT plan containing seven fields, each delivered from different gantry and collimator angles. These fields were delivered to the calibration phantom at zero gantry angles. The delivery information and parameters are summarised in Table 5-3. The 6 MV head and neck IMRT fields were delivered to the head phantom and imaged using the same linac and EPID respectively as for Study B. The phantom was set-up isocentrically on the linac couch. A 6 MV 25×25 cm^2 open field was delivered to the head phantom and calibration phantom and the images were acquired.
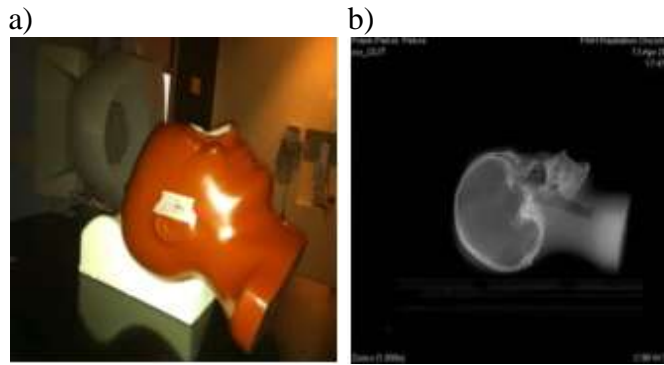
Figure 5-2: *a) the head phantom. b) Scout image of head phantom.*

Table 5-3: *The head and neck IMRT treatment images and delivery information for Study C.*

Field	# segments	Monitor Units (MU)	Gantry angle (º)	Collimator angle (º)	# frames
Field 1	9	58	150	15	90
Field 2	10	58	80	10	90
Field 3	9	57	40	5	90
Field 4	14	89	0	0	130
Field 5	9	58	320	355	90
Field 6	11	53	280	345	90
Field 7	8	65	205	350	110

Studies D and E: These studies were performed to investigate the poor quality of the C-measured images at non-zero gantries. This investigation was performed over two stages. Firstly (study D), the IMRT fields were delivered to the thorax phantom (CIRS, USA) from different gantry angles as per Table 5-3. This field then was delivered to two different calibration phantoms. The first calibration phantom geometry was a cylindrical solid water phantom (QARM, USA), with the fields delivered from different gantry angles as per the plan. The second calibration phantom geometry was a PW slab, where the field was delivered at zero gantry angles (as per Studies B and C). These phantoms are shown in Figure 5-3.

In the second investigation (study E), the IMRT field was delivered to the head phantom (CIRS, USA) and to the cylindrical calibration phantom from different gantry angles. The field was then delivered to the slab calibration phantom at zero gantry angles as for Studies

B and C. The thickness of the calibration phantom slab used was 18 cm. These two studies
were performed to investigate the effect of gantry angles on the quality of the C-measured
images; when the calibration images are acquired at zero and non-zero gantry angles using
different calibration phantoms geometries. Table 5-4 shows all the IMRT fields' delivery
information.

The Agility linac (Elekta) with 160-leaf multi-leaf collimator with 5 mm width was used to
deliver the IMRT fields. All the phantoms were setup isocentrically with 100 cm to the
centre of the phantom from the target. The images were acquired following the same
procedures in the previous three studies (A, B, and C). The EPID images were acquired
with 80 frames and 433 ms integrated time using iView software. The IMRT EPID images
were calibrated using the division method.

a)   b)   c)
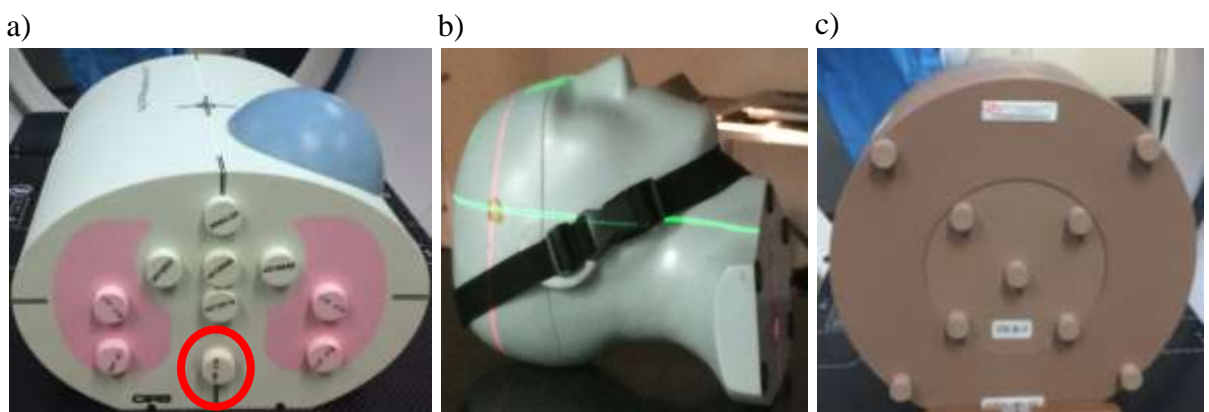
Figure 5-3: *a) The thorax phantom with five tissue equivalent inserts, four lung inserts and
one bone insert (circled in red). b) The head phantom with a holding strap to keep the two
pieces together. c) The cylindrical solid water (SW) phantom (calibration phantom).*

Table 5-4: *The IMRT field's delivery information for Studies D and E.*

Field	Gantry angle (°)	Collimator angle (°)	# of frames	# of monitor units
Field 1	0	0	80	62
Field 2	45	0	80	93
Field 3	90	0	80	36
Field 4	115	0	80	30

5.2.1.1 The calibration of the measured IMRT EPID images

The calibration method (division method) described in Section 3.4 for calibrating the simulated IMRT EPID images was used to calibrate the measured IMRT EPID images. The calibration method was used to remove modulations and beam variances. A Matlab code was developed to read the measured IMRT EPID image, average it according the number of frames and finally correct the image to the signal offset (dark image). The image was corrected by subtracting the dark field image from the IMRT EPID image. The same image correction procedure was applied to the calibration image. The calibration phantoms used in those studies were PMMA phantom (Study A), PW slab (Studies B, C, and E) and the solid water phantom (Studies D and E). Finally, the C-measured image was developed by dividing the humanoid phantom IMRT EPID image by the calibration IMRT EPID image. The measured images of the humanoid phantom and the calibration phantom were the same type and had the same size and resolutions. The C-measured image was calculated as per Equation 5.1:

$$I_{measured\_calibrated}(x,y) = \frac{I_{humanoid\_phantom}(x,y)}{I_{calibration\_phantom}(x,y)} \qquad [5.1]$$

5.2.2 Monte Carlo Simulations

The same commissioned linac model was detailed in Chapter Three. The simulation parameters used are the same as in Section 3.2.1.1.

DOSXYZnrc was used to simulate the EPID and all the phantoms. The model EPID was detailed in Section 3.2.2.1. The humanoid phantoms of the pelvic and head phantoms were

modelled using their CT data, and the phase space files resulted from BEAMnrc simulation were used in the input file of DOSXYZnrc. The EPID model and the CT data egsphant file format were used in the DOSXYZnrc input file. The egsphant file was generated via CTCombine code as detailed in Chapter Three. The calibration phantoms used in these studies were the PMMA phantom for Study A, and the modified egsphant file calibration phantom of the pelvic and head phantoms in Studies A, B, and C.

Study A: Fields were simulated at zero gantry angles as per the measurements. Firstly, a 25 $\times$ 25 cm^2 open field was simulated in BEAMnrc. The phase space file was used in the input file of DOSXYZnrc simulation of the pelvic and PMMA phantoms simulations. Secondly, following the pelvic phantom scanning (described previously in the experimental materials and methodology); the CT data was used in CTCombine to create the egsphant file that included both the pelvic and EPID information together at the different gantry angles. The IMRT field was simulated and the phase space file was used in the DOSXYZnrc simulation of the pelvic phantom and the modified calibration phantom. The boundaries used in creating this egsphant file (describes the phantom in voxels and CT numbers for each material) was from -20.5 to + 20.5 in both x and y directions, and from -37.9 to +37.9 in z direction (CT coordinate system). The voxel sizes were 0.16, 0.16 and 0.46 cm in x, y, and z directions respectively to create an image of 256 $\times$ 256 resolution. The number of histories used in the simulations was 2 x 10^9 particles for each run. All those runs were performed in parallel in a batch of 10 processes. The EPID images of the pelvic and calibration images were calculated and the pelvic image was calibrated using the division method detailed in Section 3.2.3. C-simulated was calculated as per equation 5.2:

$$I_{MC\_calibrated} = \frac{I_{MC\_Pelvis}(x, y)}{I_{MC\_PMMA/modified}(x, y)} \qquad [5.2]$$

Study B: The BEAMnrc code was used to model the linear accelerator head geometry. The phantoms and EPID were simulated in DOSXYZnrc. This model was commissioned and verified by matching the beam profiles and depth dose profile. The best energy match between measured (10 MV) and simulated energy was found to be 9.1 MV. All the simulation procedures in BEAMnrc and the simulations parameters were the same as in

Study A. The five IMRT fields were simulated using different gantry and collimator angles. The CTCombine code was used to produce the egsphant file from the CT data as for Study A. The boundaries used in creating the pelvic and EPID egsphant file were from -20.5 to +20.5 cm in both x and y directions and from -13.2 to +12.8 cm in the z-direction. The z-direction boundaries cover the phantom thickness, where the x and y boundaries cover the entire active are of EPID. The egsphant file is generated then combined with the egsphantfile of the EPID which is read separately from EPID text file that contains all EPID information. The two egsphant files are then combined via CTCombine. The voxel size of 0.16, 0.16, and 0.2 cm in x, y, and z directions respectively created a simulated EPID image with 256 x 256 resolution. The calibration phantom used in the simulations to calibrate these simulated IMRT EPID images was the modified calibration phantom approach used in Study A and detailed in Section 3.2.2.1. The simulated IMRT EPID images were obtained and calibrated using the same calibration method as per Equation 5.3.

$$I_{MC\_calibrated}(x,y) = \frac{I_{MC\_pelvis}(x,y)}{I_{MC\_pelvis\_modified}(x,y)} \qquad [5.3]$$

Study C: this study employed the same simulation materials and procedures used in Study B. The linac model used in this study was the same linac model used in study A with 6 MV energy. Seven IMRT fields were simulated in BEAMnrc using different gantry angles. The phantoms simulated were a head phantom and its modified calibration phantom using their CT data in the input files of DOSXYZnrc and the corresponding phase space files. The boundaries used in creating the head and model EPID egsphant file using CTCombine were -20.5 to + 20.5 cm in both the x and y directions and -18.9 to +14.8 cm in z-direction. The voxel size 0.16, 0.16, and 0.2 cm in x, y, and z directions created an image with 256×256 resolution. IMRT EPID images were generated and calibrated following the same procedures used in Study B.

5.2.2.1 The calibration of the simulated IMRT EPID images

The calibration method (division method) detailed Section 3.2.2 was used in the calibration of the simulated images. Both calibration phantom approaches were used: the first approach was the simulated PMMA calibration phantom, and the second was the simulated

modified calibration phantom. These approaches were also detailed in Section 3.2.2.1. The calibration method is expressed in equation 5.4.

$$I_{MC\_calibrated}(x, y) = \frac{I_{MC\_phantom}(x, y)}{I_{MC\_PMMA/modified}(x, y)} \qquad [5.4]$$

5.2.3 Phantom position and set-up errors verification

Following the calibration of the simulated and measured IMRT EPID images in Studies A, B, and C, the C-measured image of each field was matched with the corresponding C-simulated image. Three methods were used in the images matching process and investigating the similarity between the two images:

1. *Visual inspection:* the C-measured images were inspected and compared with the C-simulated images by four independent individuals to detect any displacement in the bone anatomy or the field edge in the C-measured images. This procedure was applied in the three Studies A, B, and C. Another visual inspection approach was applied in Study A only, which involved overlaying the registered C-measured image on the registered C-simulated (reference image) using Matlab. The C-measured image was left as a greyscale image and partially transparent. The C-simulated image was converted into an RGB image in order to easily visually detect any displacement or bone anatomy mismatch between the two images.

2. *The correlation coefficient r: the C*-measured and C-simulated were correlated in Matlab. The *r*-value was between the two images. The r-value is between 0 and 1, where 1 indicates a strong similarity between the two images (strongly correlated) and zero indicates no similarity or they are not correlated. The *r* value was calculated using Equation 5.5

$$r = \frac{\sum\limits_{i} \sum\limits_{j} (A_{ij} - \overline{A})(B_{ij} - \overline{B})}{\sqrt{\left(\sum\limits_{i} \sum\limits_{j} (A_{ij} - \overline{A})^2 \right)\left(\sum\limits_{i} \sum\limits_{j} (B_{ij} - \overline{B})^2 \right)}} \qquad [5.5]$$

A is the C-measured image; B is the C-simulated image; $\overline{A}$ is the mean of the C-measured image and $\overline{B}$ is the mean of the C-simulated image.

3. *The iView software:* the clinical software provided by Elekta for acquiring and matching EPID images with the reference image was used. Clinically patient's EPID images are used to reduce patient set-up errors by comparing them with digitally-reconstructed radiographs (DRR reference images) as a part of the patient position verification process before treatment. This allows manual registration of the two images for position and set-up errors verification purposes. Treatment field edges the stable bone structure in the reference image can be contoured. The iView clinical software (Elekta) was used in this study to confirm the visual inspection results and verify the phantom position in the measured images of the humanoid phantoms with respect to the MC reference image. This procedure followed can be summarised in few steps:

1. Display the C-simulated image (reference image) in the iView software.
2. Display the corresponding IMRT field C-measured image.
3. Contour the IMRT field edge in reference image.
4. Contour the important visible bone anatomy in reference image.
5. The field edge and bone structure contours were automatically superimposed onto the corresponding C-measured image and matched with the reference image.
6. The iView displays any horizontal/vertical displacement in the C-measured image with respect to the field edge and the bone anatomy in the reference image in millimetres.
7. The matching procedure was repeated four times by performed the matching four times using the iView software.
8. The mean, standard deviation, and standard error of the horizontal and vertical displacements results were calculated and recorded.

5.3 RESULTS

The results of each study in this chapter are presented in two sections as measured and simulated results. All the measured and simulated IMRT EPID images are shown before and after calibration. A comparison between the measured and simulated images results will be presented.

5.3.1 Measurements

5.3.1.1   Study A

Figure 5-4 (a) shows the 25×25 cm^2 open field EPID image of the pelvic phantom. The pelvic image was calibrated by dividing it by the PMMA EPID image (calibration image). The calibrated EPID image pixel values were inverted for clearer bone visibility as shown in Figure 5-4 (b). The bone anatomy in this image after calibration is clearer and can be outlined. The IMRT EPID images before and after calibration of the prostate field of the pelvic phantom are shown in Figure 5-4 (c, d, and e). The greyscale values in the pixels were inverted to improve the bone anatomy visibility. The calibration method successfully removed the modulations improving the visibility of the revealed bone anatomy in the image. The IMRT field shape and edges can be seen clearly in the calibrated image as well.
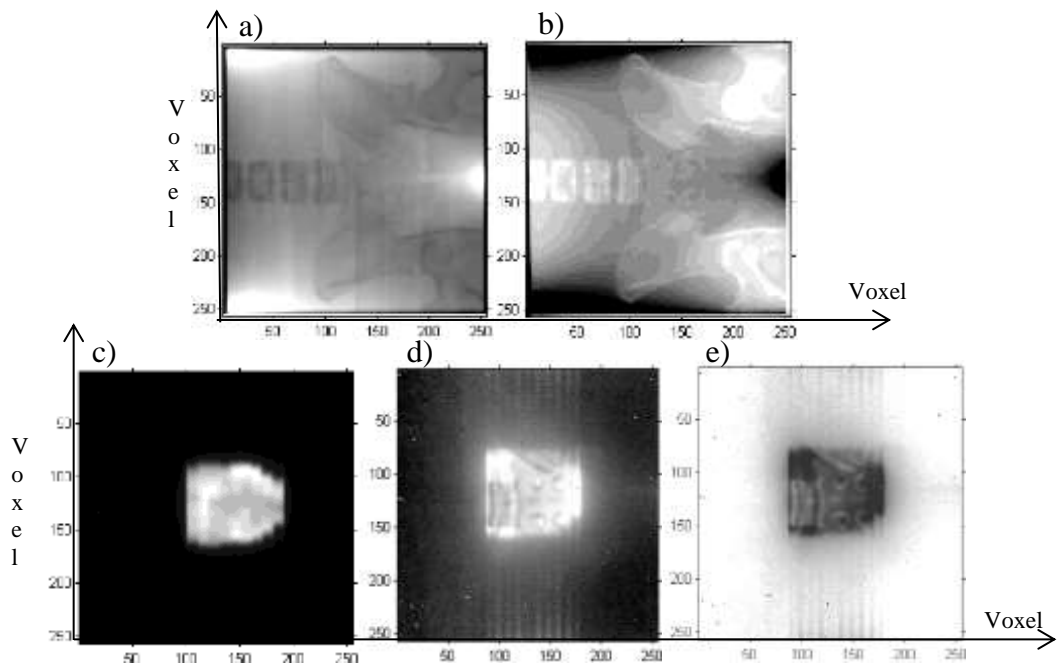
Figure 5-4: a) A *25×25 cm^2 pelvic phantom image (reference image). b) 25×25 cm^2 pelvic phantom image after calibration (the pixels values were inverted to show the bone anatomy clearer). c) The IMRT EPID image of the pelvic phantom before calibration. d) The calibrated measured IMRT EPID image (C-measured) of the pelvic phantom. e) The C-measured image in (d) with all pixels values inverted.*

5.3.1.2 Study B

An open field image of the pelvic phantom was acquired using a 10 MV 25×25 cm^2 field as a reference image. The calibration images of the plastic water (PW) phantom were also acquired. The pelvic phantom bone structure can be seen in the calibrated image as shown in Figure 5-5(a, b). This image was calibrated to visually assess the effect of the calibration on the quality of the image of the uniform intensity image (open field). The calibrated image greyscale values were inverted as shown in Figure 5-5(b) to show clearer bone structure. The resulting calibrated image show the pelvic phantom bone anatomy clearly, and the details of the bone can be outlined.
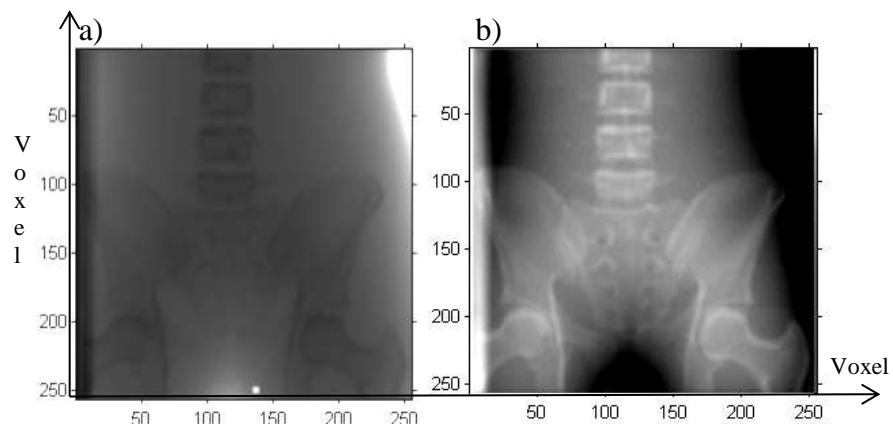
Figure 5-5: *a) A 25×25 cm^2 calibrated pelvic phantom image by plastic water. b) The calibrated pelvic phantom image in (a) inverted to improve the contrast of the bone structure clearly.*

Following measurement of the open field images, the prostate IMRT field's images were acquired using the EPID. Figure 5-6 shows the IMRT EPID images before calibration of the prostate fields delivered from different gantry and collimator angles. The calibration images of the PW phantom were acquired using zero gantry angles fields' delivery.
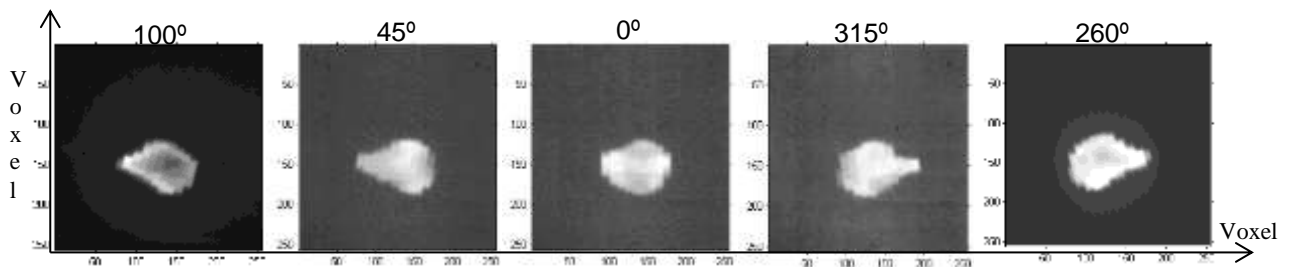
Figure 5-6: *Measured prostate IMRT field images of the pelvic phantom before calibration showing the gantry angles.*

The C-measured images of the prostate IMRT fields in Figure 5-7 show how the calibration procedure has removed modulations from the images. The greyscale calibrated images have been inverted to improve the contrast. The zero gantry angle calibrated image at the third field show the best bone anatomy visibility. The remainder of the calibrated images are of a poor quality and have no clear visibility of the bone anatomy. These images were delivered at a non-zero gantry angles. The causes of the poor quality of these images are discussed in the results discussion section.
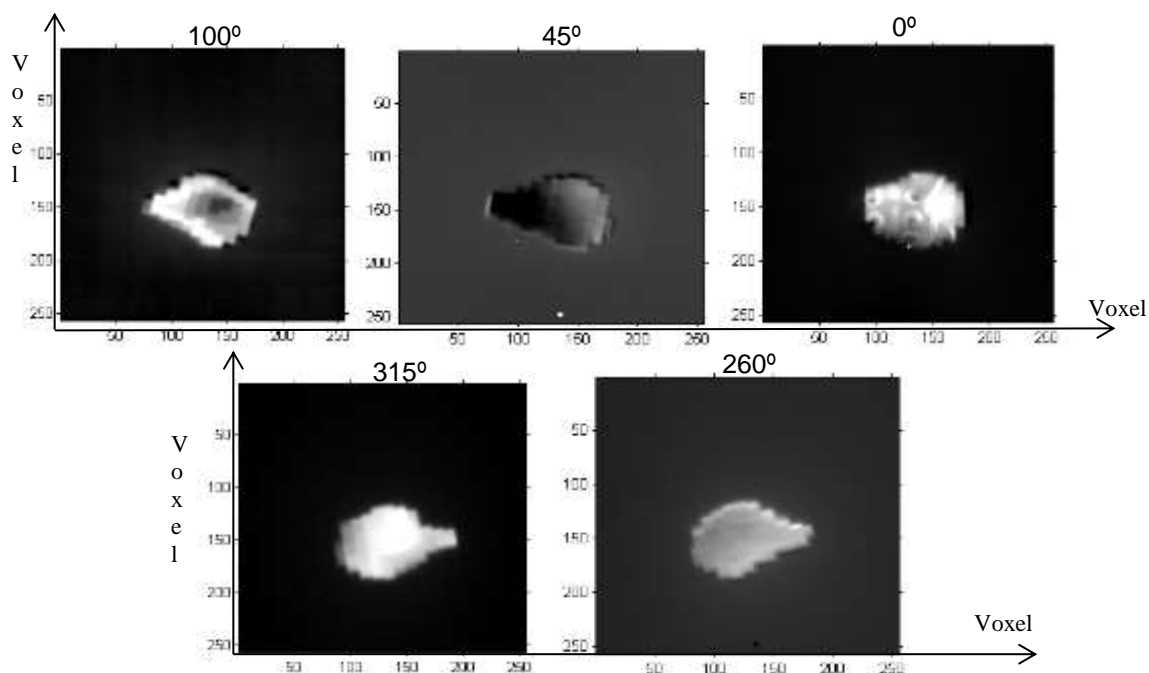
Figure 5-7: *The prostate C-measured images of the pelvic phantom.*

5.3.1.3 Study C

An open field image of the head phantom was acquired using a 6 MV 25×25 cm^2 field as a reference image as shown in Figure 5-8(a). The calibration images of the plastic water (PW) phantom. The calibration method was applied to this image. Figures 5-8(b, c) show the calibrated image of the head phantom. The greyscale values in each pixel of the calibrated image were inverted to show clearer bone structure in the image.
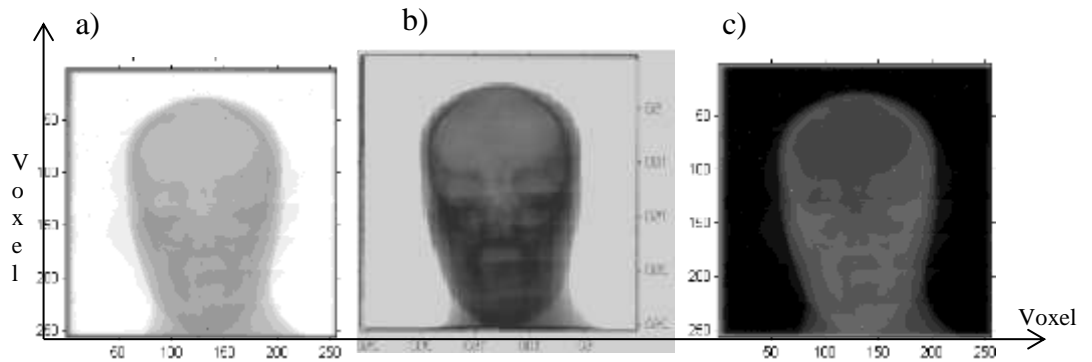
Figure 5-8: *a) Open field 25×25 cm^2 of the head phantom (reference image). b) A 25×25 cm^2 calibrated head phantom image. c) Calibrated head phantom image in (b) inverted to show the bone structure clearly.*

The head and neck IMRT fields were delivered using a step-and-shoot technique from different gantry angles and to a calibration phantom (20 cm thickness PW) at zero gantry angles. The IMRT EPID images for each field with the EPID are displayed in Figure 5-9. The head phantom IMRT images for all the fields were calibrated using the division method as shown in Figure 5-10. Moreover, all calibrated images show that outside the IMRT field the actual phantom can be seen and outlined. The measured calibrated IMRT images of the head phantom show the bone anatomy in the images. By visual inspection of these images, it can be seen that the IMRT field edge in each image can be seen. The bone anatomy in these images was visible and the best result was seen at zero gantry angles. The remainder of the images, delivered at non-zero gantry angles, are of a poorer quality; however, it is visually noticeable that the image quality worsens with the increases of gantry angle between 0° and 180° degrees.
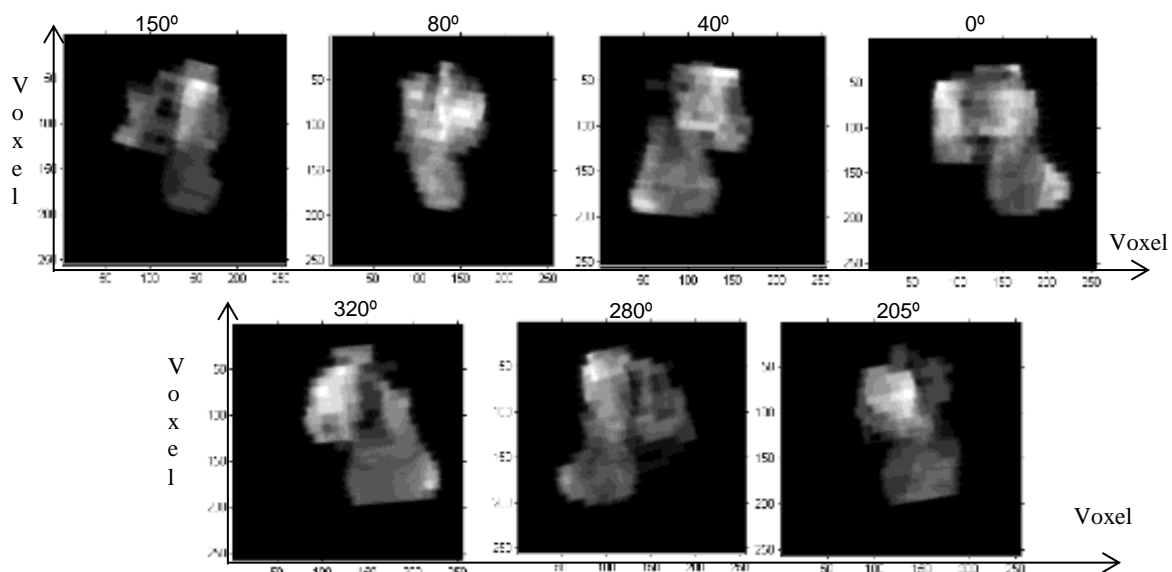
Figure 5-9: *Measured head and neck IMRT field images of the head phantom before calibration showing the gantry angles.*
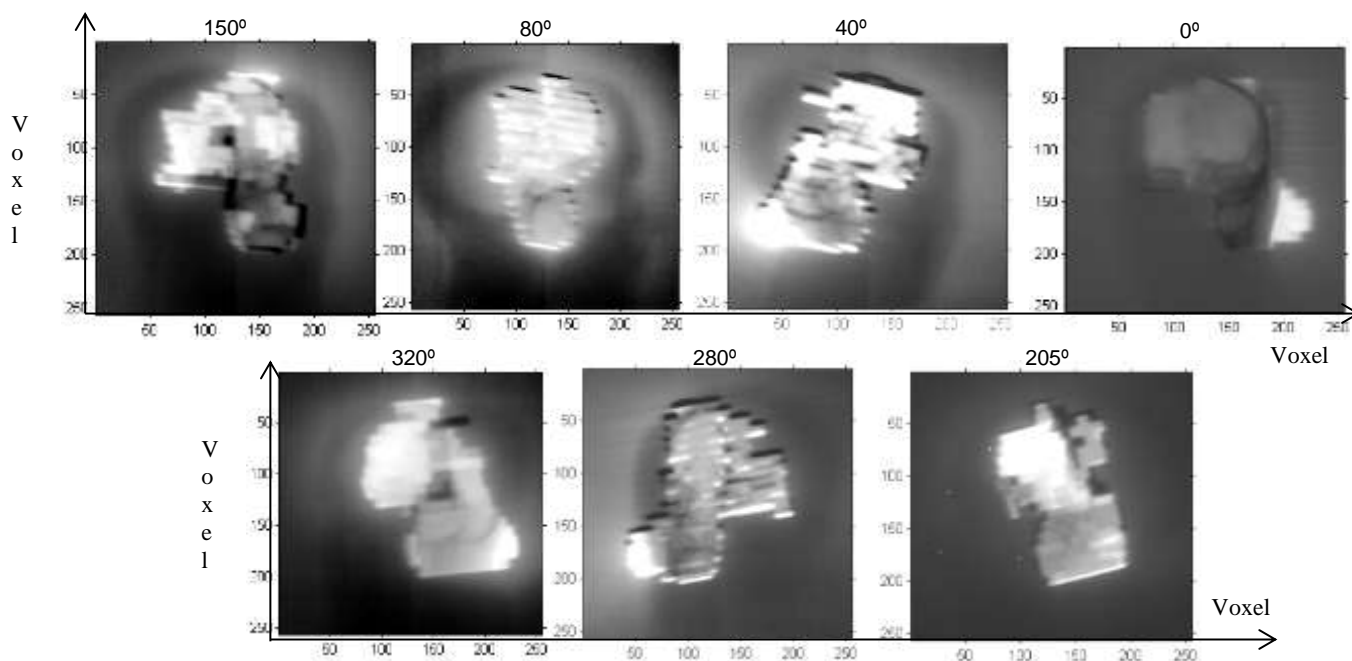
Figure 5-10: *The C-measured images of the head phantom.*

5.3.1.4   Study D and E

The images of the thorax (Study D) and head (Study E) phantoms were acquired and calibrated following the same procedures in the previous three studies (A, B, and C). The IMRT EPID image of the thorax and head phantom before calibration and the calibration phantoms image are shown in Figure 5-11(a, b, c, and d).
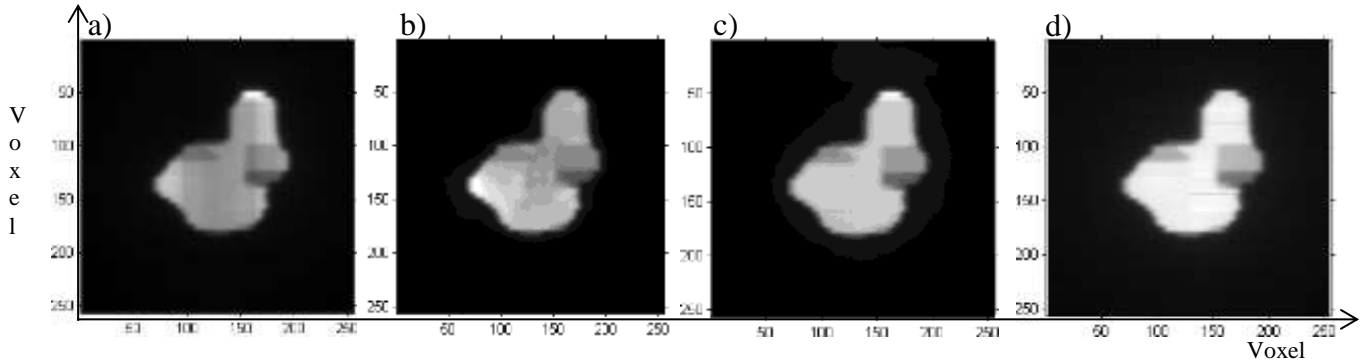
Figure 5-11: *a) The measured IMRT EPID image of the thorax phantom before calibration. b) The IMRT EPID image of the head phantom before calibration. c) The IMRT EPID image of the cylindrical solid water phantom (calibration phantom). d) The IMRT EPID image of the plastic water phantom (calibration phantom).*

1.   *Thorax phantom results (Study D):* the C-measured images of the thorax phantom at all gantry angles resulting from using the cylindrical calibration phantom are shown in Figure 5-12 (a, b, c and d). The C-measured images of the thorax phantom resulting from using the slab calibration phantom are shown in Figure 5-12 (e, f, g, and h). These illustrate that the beam modulations were removed from the images and the bone insert is visible. Visually it can be seen that both images show the same details in the corresponding images. The four sets of the C-measured images of the thorax phantom using the cylindrical calibration phantom were correlated with the thorax phantom C-measured images using the slab calibration phantom in Matlab. This correlation/matching was performed between these measured images since no simulated images were generated, and to investigate if the calibration shape will affect the quality of the calibrated measured images. These images were correlated to test the similarities between the two sets of images within the field edges. The *r*-value was calculated after masking all the pixels outside the field using that pixel value at the field edge as the threshold value. The calculated *r*-values indicated a

good similarity between these two sets of images (calibrated images by cylindrical phantom and calibrated images by slab phantom). The mean value of the correlation between the calibrated thorax images was 0.80 as shown in Table 5-5.

2.   *The head phantom results (Study E):* This study followed the same procedure as that of Study D. Figure 5-13 shows that the IMRT EPID images were calibrated successfully and the bone structure masked by the IMRT field was revealed and visible at all gantry angles used. Even at gantry angles of 90° and 115° the clip of the strap around the head phantom can be seen in both images. The resulting images using both calibration phantom methods show good quality images and visually the bone structure and other details can be seen. The correlation coefficients between these images are shown in Table 5-5. They indicate a good correlation between these images.

Table 5-5: *The correlation coefficients between the C-measured images of both thorax and head phantoms images calibrated by slab and cylindrical calibration phantoms.*

IMRT image gantry angles (θ°)	*r*-value of C-measured thorax images	*r*-value of C-measured head images
0	0.81	0.80
45	0.81	0.80
90	0.78	0.82
115	0.81	0.81
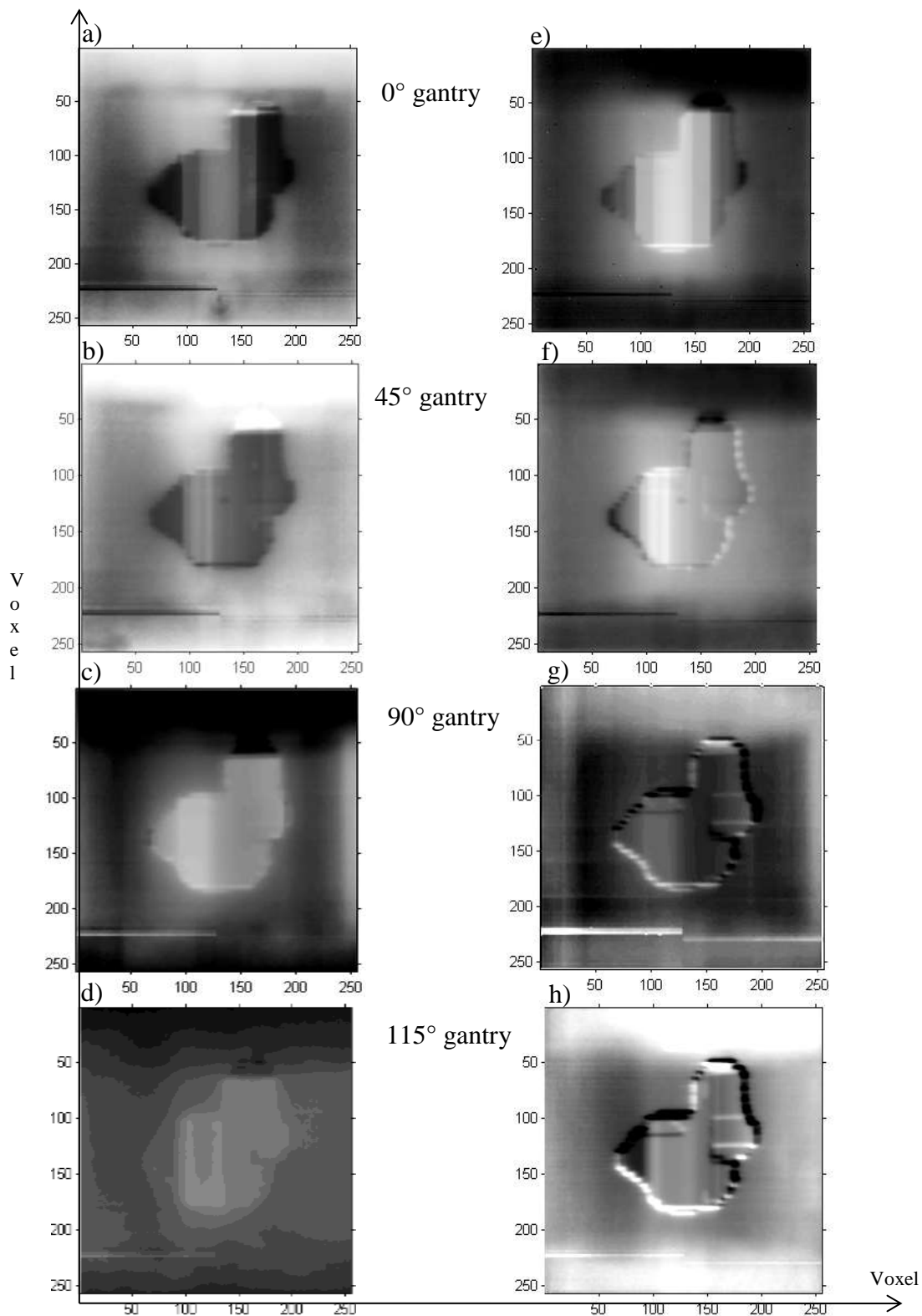
Figure 5-12: *The C-measured images of the thorax phantom calibrated by the cylindrical phantom (a, b, c and d), and the calibrated images by slab phantom (e, f, g and h).*

Figure 5-13: *The C-measured images of the head phantom calibrated by the cylindrical phantom (a, b, c and d) and the calibrated images by slab phantom (e, f, g and h).*

5.3.2 Simulations

5.3.2.1 Study A

After simulating the head geometry of the linac in BEAMnrc, and the phantom and model EPID in DOSXYZnrc, the simulated images were obtained and displayed. The images were calibrated using the division method. Figure 5-14(a) shows the simulated image of the 25×25 cm^2 of the pelvic phantom. This image shows the anatomy in the pelvic phantom. To test the calibration method on a uniform intensity image, the open field image of the pelvic phantom was divided by the simulated open field 25×25 cm^2 of the PMMA calibration phantom. The resulting calibrated simulated image of the open field of the pelvic phantom is shown in Figure 5-14(b). The bone anatomy is clearly shown and can be outlined as shown in Figure 5-14(c). Following the test of the calibration method using open field, the IMRT field was simulated and resulting image was calibrated. Figures 5-14 (d, e) show the simulated IMRT EPID images of the pelvic phantom and the calibration phantom (modified pelvic phantom) respectively. The calibration method was applied to the IMRT EPID image of the pelvic phantom using the PMMA phantom image and the modified pelvic image for calibration. The resulting C-simulated images are shown in Figure 5-14 (f, g). The C-simulated image of the pelvic using the PMMA image for calibration Figure 5-14 (f) shows the field edges and the bone anatomy despite the blurring artefacts that affected the image quality. The same calibration procedure used previously was followed here using the modified pelvic phantom calibration image. The C-simulated image resulting from using the simulated modified pelvic phantom as a calibration phantom shows a better quality calibrated image than the calibrated image using the PMMA phantom, as shown in Figure 5-14 (g). This calibration method using the modified calibration phantom approach was used in the subsequent studies (Studies B and C) and in the next chapter instead of using the simulated PMMA calibration phantom. This calibration image approach (modified calibration phantom) was selected for the subsequent studies, due to the better quality of the C-simulated image developed in this study. This approach showed a better bony anatomy and field edges visualisation than using the PMMA calibration phantom.
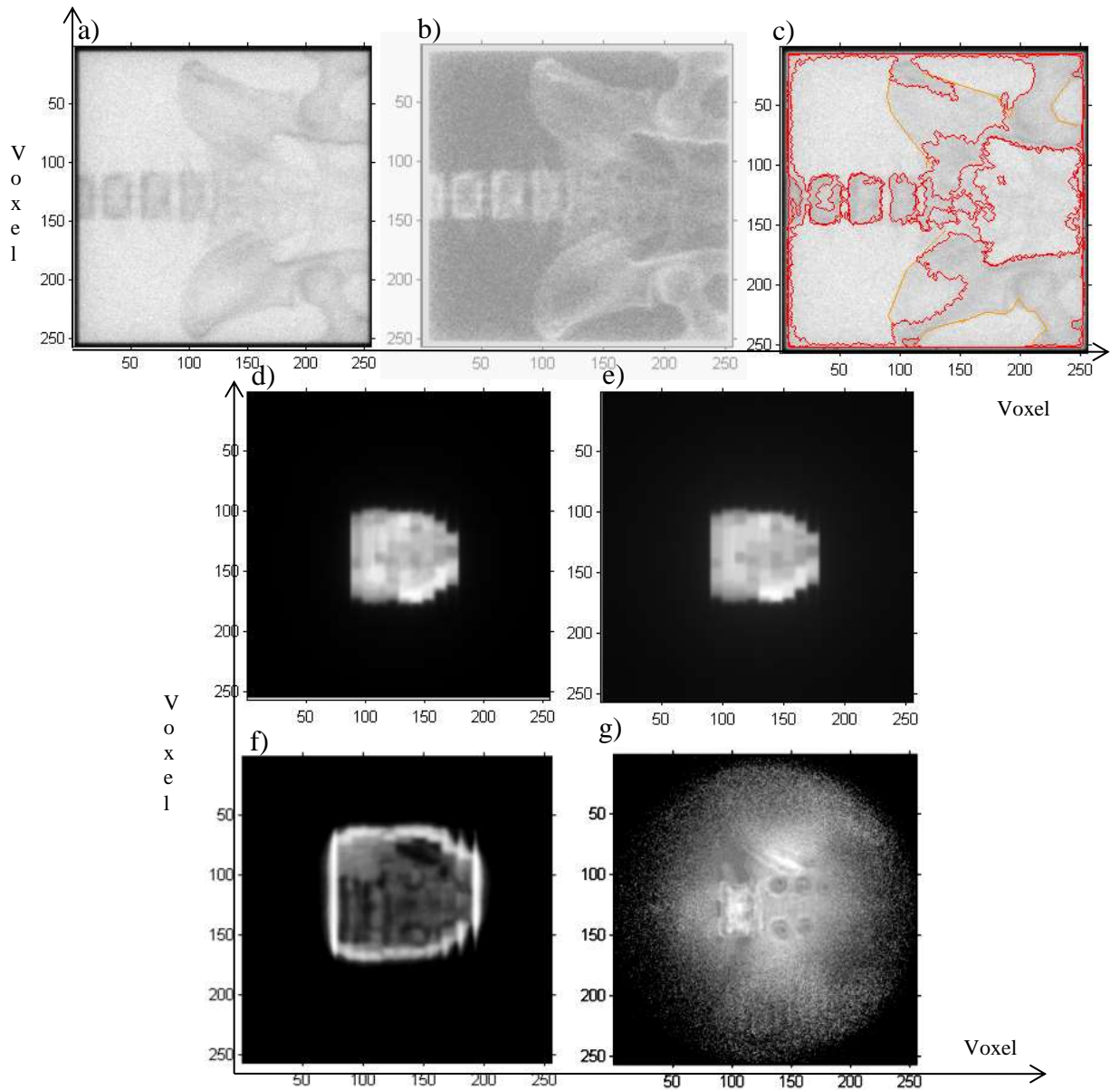
Figure 5-14: *a) The simulated 25×25 cm² pelvic phantom EPID (reference image). b) The simulated 25×25 cm² pelvic phantom EPID image after calibration inverted (performed only to show bone anatomy clearer). c) The field edge and bone anatomy were contoured in the calibrated image (b). d) The simulated IMRT field EPID image of the pelvic phantom before calibration. e) The simulated IMRT field EPID image of the modified pelvic calibration phantom (filled tissue). f) The C-simulated image of the pelvic phantom using the PMMA image for calibration. g) The C-simulated image of the pelvic phantom using the modified pelvic phantom of uniform density (tissue equivalent material) image for calibration.*

5.3.2.2 Study B

After testing the calibration method on simulated IMRT EPID images using single IMRT field (prostate field) as per study A by means of two different calibration phantoms (PMMA phantom and modified calibration phantom). The study was broadened into simulating full IMRT treatment (prostate treatment containing five fields). The simulated IMRT EPID images of the prostate treatment fields before calibration are shown in Figure 5-15. The simulations were repeated with a modified pelvic phantom (modified egsphant file) data file to simulate the calibration images. The calibration images were simulated with the same gantry as per the plan. The images were calibrated using the division method.
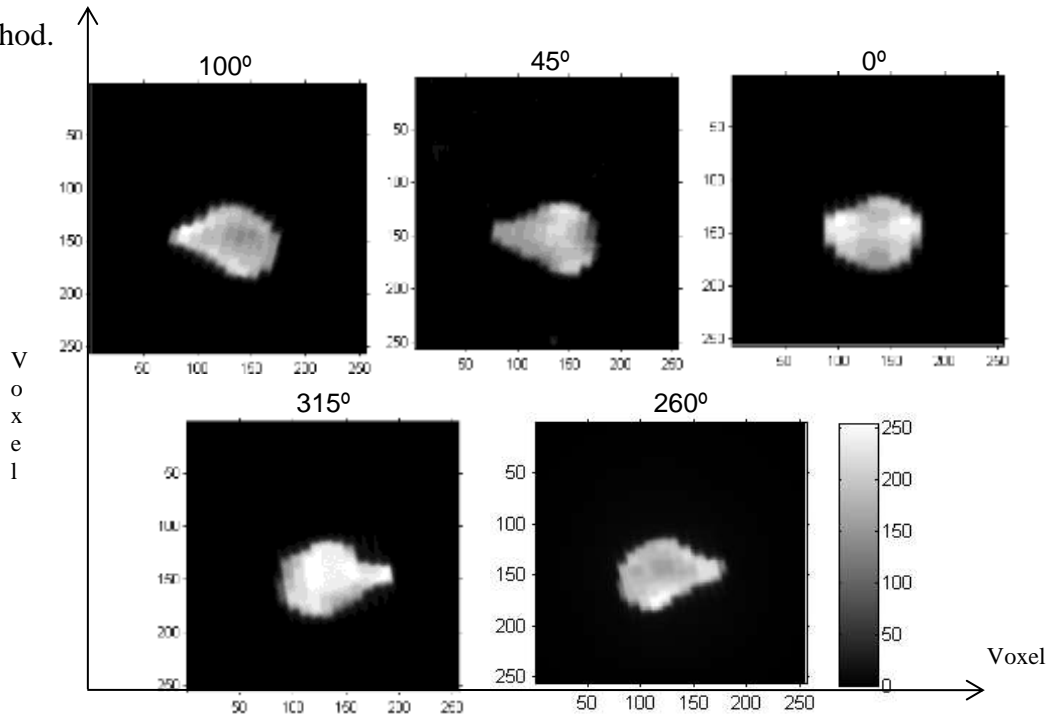
Figure 5-15: *Simulated IMRT image of the pelvic phantom before calibration showing the gantry angles.*

Figure 5-16 shows the results of calibration of the simulated IMRT EPID images. The calibration process successfully removed the beam modulations from the images. The masked bone structure in the pelvic phantom images was revealed. The bone structure and the field edges are clearly visible and can be outlined in all these images. They were used as a reference image in the phantom position verification investigation. There is also clear noise outside the IMRT field. To remove this noise, any pixel outside the field was masked and given a value of zero (black) as shown in Figure 5-17.
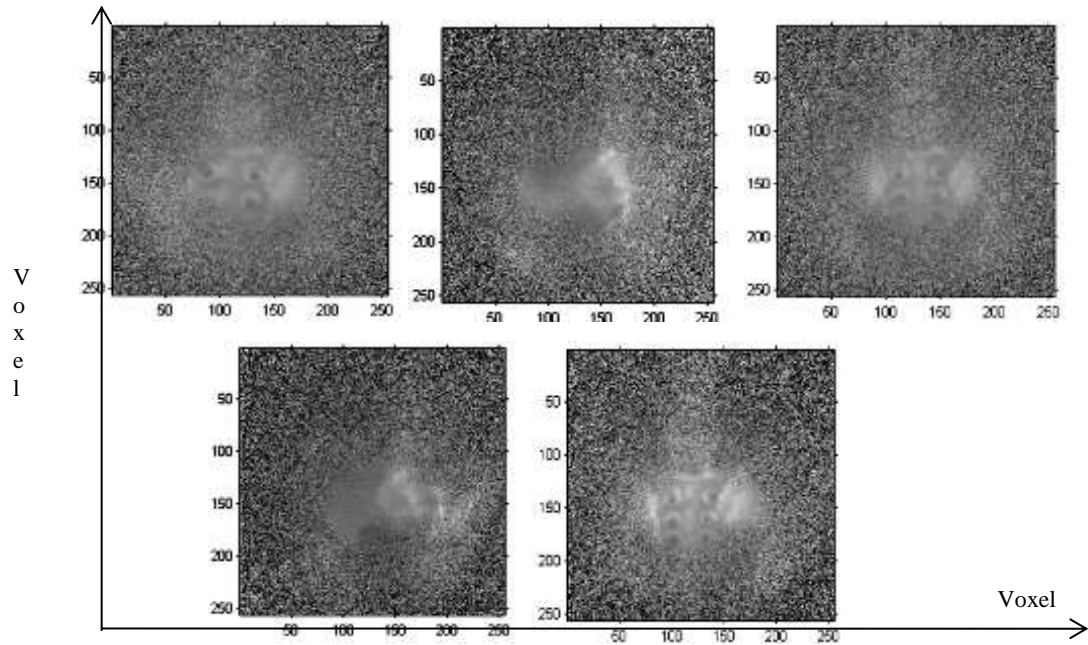
Figure 5-16: *The simulated prostate C-simulated images of the pelvic phantom*
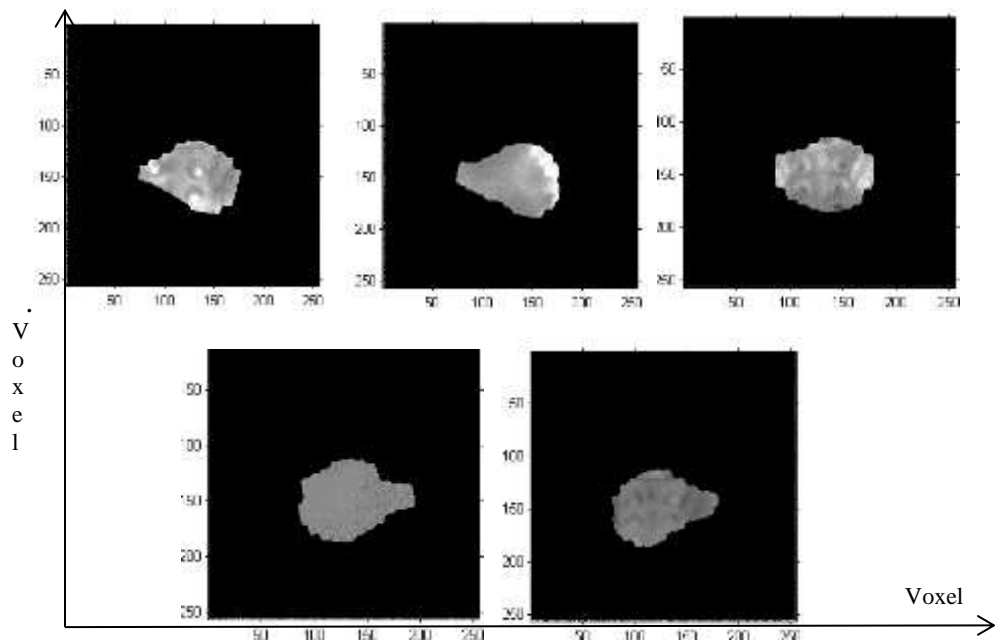
Figure 5-17: *The C-simulated images of the pelvic phantom after masking all the pixels outside the IMRT field.*

When comparing the calibrated measured and simulated images of the pelvic phantom, the C-simulated images show bone anatomy structure at any gantry angle, whereas the measured calibrated EPID images show the best results only at zero gantry angles.

5.3.2.3 Study C

Following the simulation of the measured data using MC, the simulated IMRT EPID images were calibrated. The calibration images were simulated using the same gantry angles as per the treatment plan. Figure 5-18 show all the simulated IMRT EPID images before calibration of the head and neck treatment fields. The simulations were repeated with the modified egsphant file of the head and model EPID phantom data file for calibration. Figure 5-19 show the results of calibration of the simulated IMRT EPID images of the head phantom. The calibration process successfully removed the beam modulations from the images making the bone structure inside the IMRT field visible as well as the field edges. These simulated images show visible bone structure that was not affected by the delivery gantry angles.
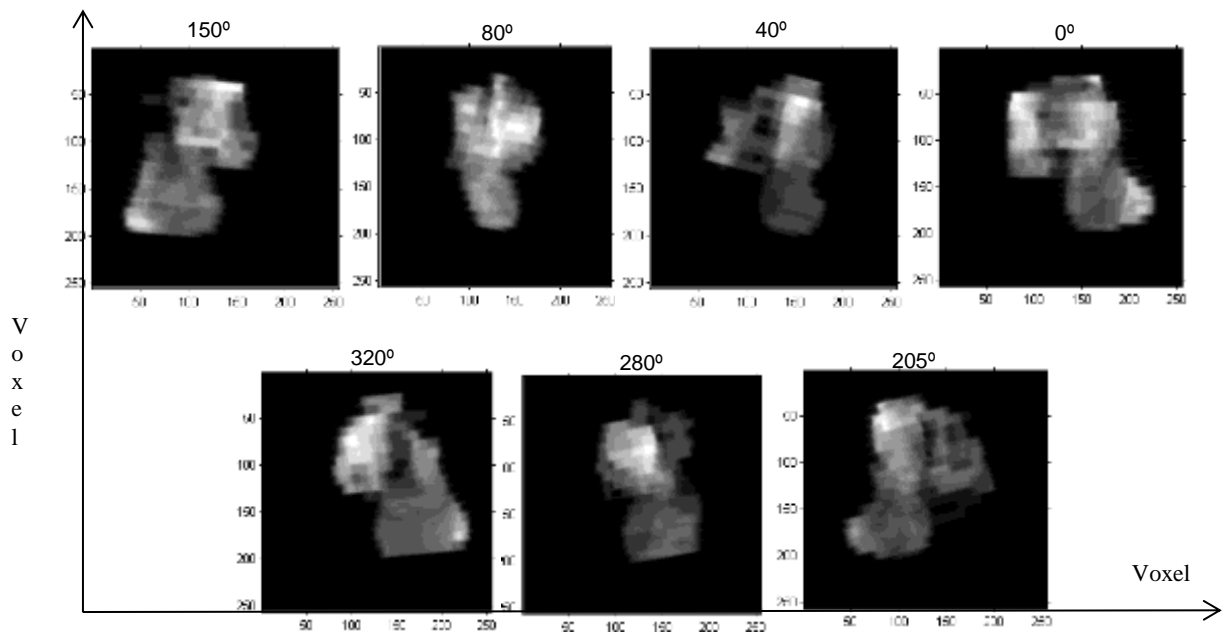
Figure 5-18: *Simulated head and neck IMRT images of head phantom before calibration.*
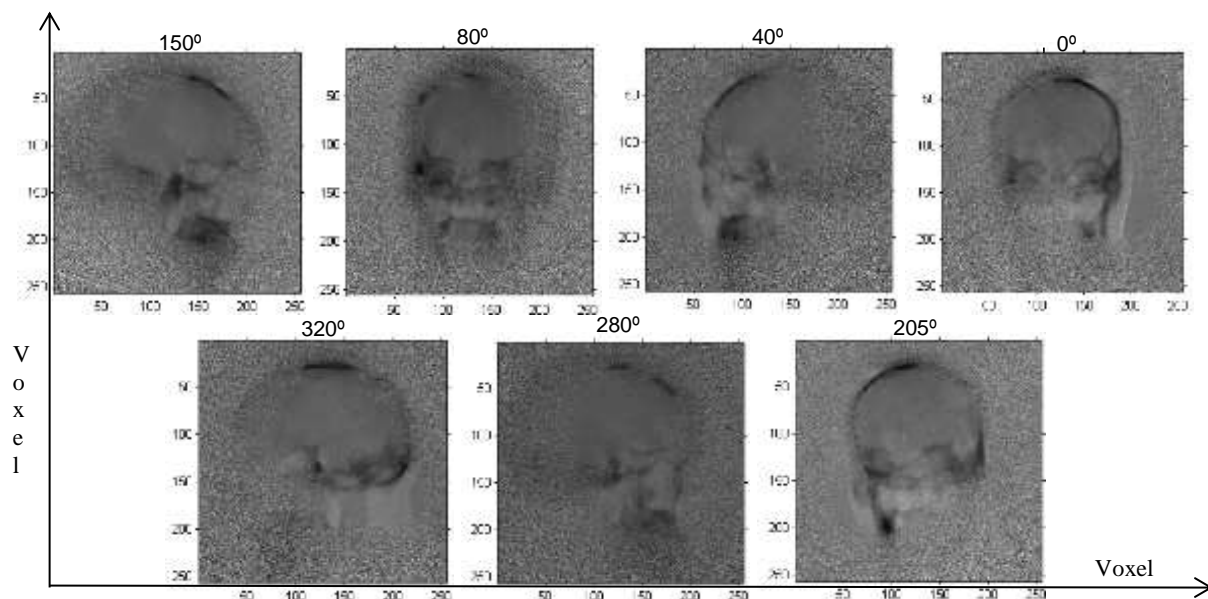
Figure 5-19: *The C-simulated images of head phantom (no masking for the pixels outside the field was applied because of the clear bony anatomy showing)*

5.3.3 Phantom position verification results

Subsequent to the calibration of the measured and simulated images, both images were matched to verify the phantom position. The C-simulated images in all studies (A, B, and C) were used as reference images for phantom position verification. The C-measured images were matched with corresponding reference images (MC image) using visual inspection and the clinical iView software. The matching process results of each study were analysed. This matching was performed to verify that the C-simulated image is of enough quality to be used as the reference image to verify the phantom position during the IMRT treatment. Figure 5-20 shows a screen shot of the matching process in the iView software.
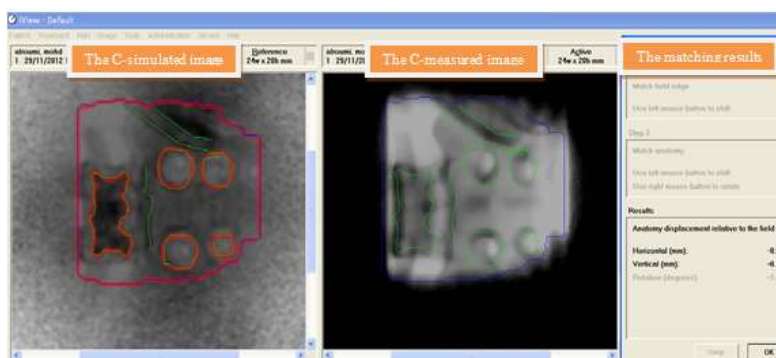
Figure 5-20: *Screen shot of the iView software shows the C-simulated image (reference image), C-measured image, and the matching results in millimetres.*

Study A: The C-measured and C-simulated images were matched using two different methods to verify the phantom reference position. Figure 5-21 and Figure 5-22 show the C-measured images overlaid on the C-simulated image (MC reference image). *The colours used in images in both figures are just for display only to help detect any shift in the field edges or the bony anatomy between the two images when overlaying the C-measured image over the C-simulated image.* Both images show no differences and no displacement can be detected visually between the C-measured image and reference image, neither in the field edges, nor in the bone anatomy. The correlation between the C-measured and MC images was calculated using Matlab and recorded $r = 0.80$. The r-value indicated a strong correlation between the two images and determines that there is similarity between both images.
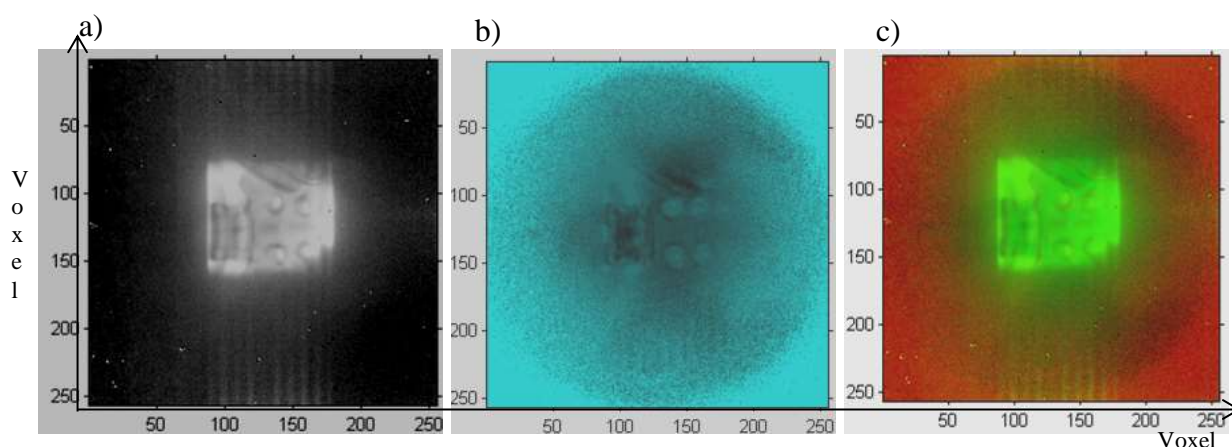
Figure 5-21: *a) The C-measured image. b) The C-simulated image (using modified pelvic calibration phantom). c) The C-measured image overlaid over the C-simulated image (reference image).*

The iView clinical software (Elekta) was used in this study to confirm the visual inspection results and to quantify the results by detecting any remaining set-up errors in the measured images of the pelvic phantom with respect to the MC image. The C-measured image was matched with the corresponding C-simulated image (reference image). This procedure was performed by four different users independently to allow for an estimation of the significance of the user variability error. The mean of detected displacement using the iView was recorded as shown in Table 5-6.
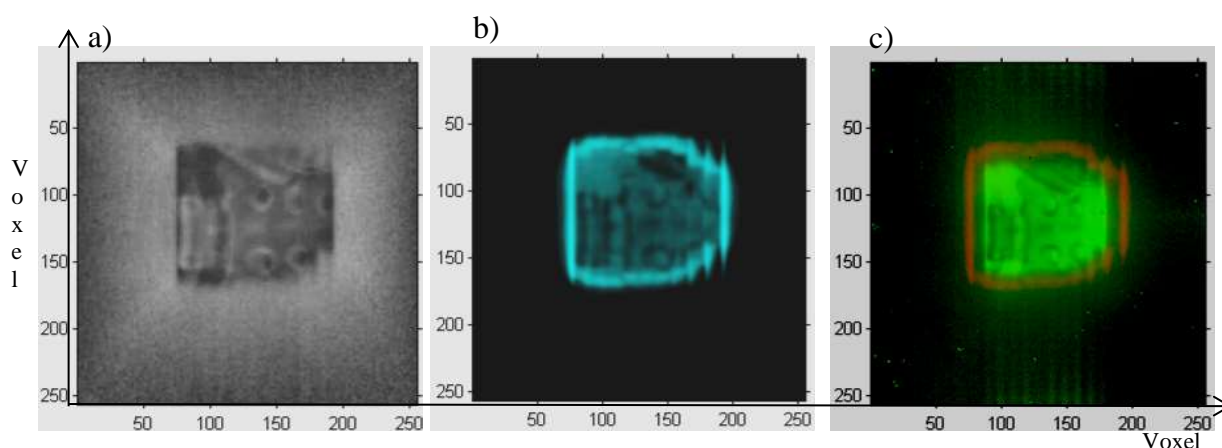
Figure 5-22: *a) The C-measured IMRT EPID image inverted. b) The C-simulated image (using PMMA calibration phantom). c) The C-measured image overlaid over the C-simulated image (reference image) the field edge was contoured.*

Table 5-6: *The iView matching results (Study A).*

MC reference position (mm).	Measured position (mm).	Detected horizontal shift (mm)	Detected vertical shift (mm).
		mean	mean
0.00	0.00	-0.50	-0.10
0.00	0.00	-0.50	-0.10
0.00	0.00	-0.40	-0.10
0.00	0.00	-0.50	-0.10

Study B: the results of the matching process in the iView are shown in Table 5-7. Each C-measured image was matched with the corresponding simulated reference image. The

matching was performed and repeated four times for each field image. The mean and standard deviation was calculated and recorded.

Table 5-7: *The results of matching the C-measured images with C-simulated images (reference image) of the pelvic phantom using iView clinical software (Study B).*

Field number	Horizontal shift (mm)		Vertical shift (mm)	
	Mean	SD	Mean	SD
Field 1	0.13	0.05	0.10	0.10
Field 2	0.10	0.10	0.06	0.11
Field 3	-2.83	0.29	0.80	0.35
Field 4	-0.40	0.17	0.10	0.17
Field 5	-0.36	0.32	0.16	0.20
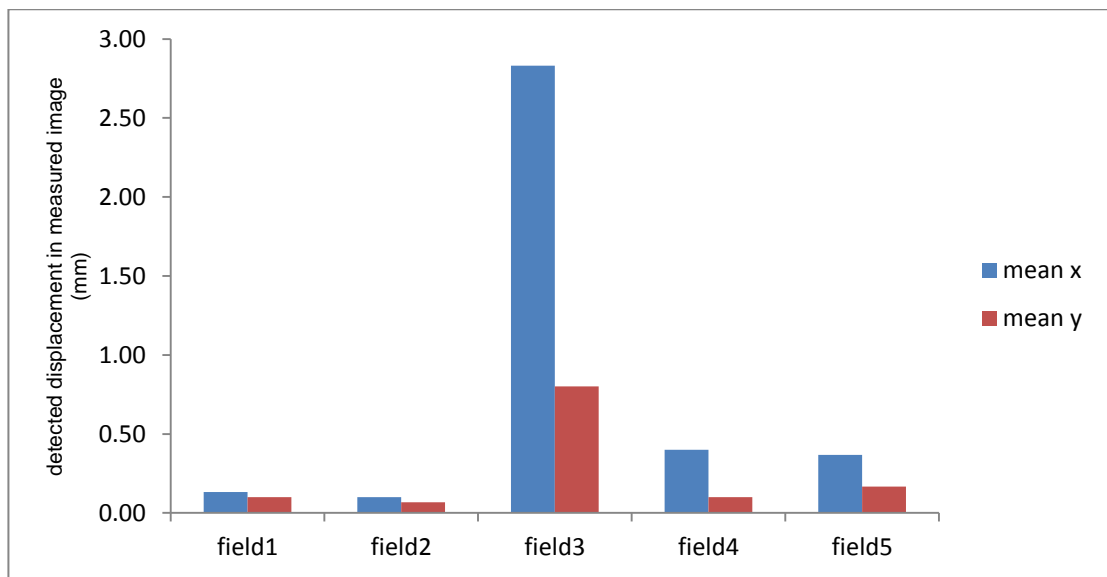
Figure 5-23*: The detected horizontal and vertical displacements in the C-measured images of the pelvic phantom using the iView.*

Study C: The C-measured and C-simulated images were matched using the iView software to verify the head phantom position. The same procedure followed in Study B was repeated in this study. The results of the matching process are shown in Table 5-8 for the head and neck IMRT fields. **Table 5-8:** *The results of matching the bone anatomy in the*

C-measured with C-simulated images (reference image) of the head phantom using iView
clinical software (Study C).

Field number	Horizontal shift (mm)		Vertical shift (mm)	
	Mean	**SD**	**Mean**	**SD**
Field 1	0.16	0.05	0.40	0.20
Field 2	-0.60	0.11	-0.60	0.10
Field 3	0.32	0.03	-0.46	0.11
Field 4	1.17	0.29	-1.00	0.01
Field 5	-0.26	0.05	-0.40	0.20
Field 6	0.00	0.00	0.23	0.05
Field 7	0.16	0.05	0.33	0.28
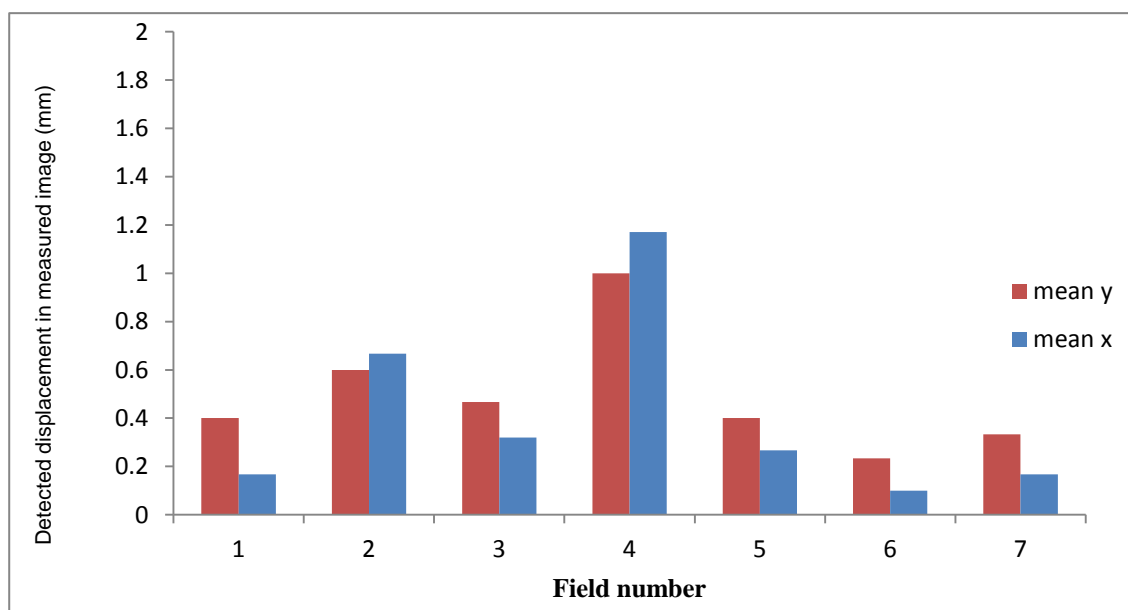
Figure 5-24: *The detected horizontal and vertical displacements in the C-measured*
images of the head phantom using the iView.

5.4 **DISCUSSION**

Studies A, B, and C investigated anatomical imaging in IMRT EPID images during the treatment and the feasibility of using C-simulated images as a reference image for offline patient position verification during IMRT. The calibration method was applied to both simulated and measured IMRT EPID images. Following the calibration of the images, the phantom position was verified visually first, then the Elekta clinical software iView was used for qualitative and quantitative analysis. The phantom position verification procedure was performed to evaluate the use of the C-simulated image as a reference image during IMRT and the feasibility of the calibration method in measured and simulated images. In these studies there were no intentional errors introduced to either measured or simulated images.

Study A investigated a prostate IMRT field delivered at zero gantry angles. The results of this study showed that applying the calibration procedure to the IMRT EPID images has removed the beam modulations from the images. Consequently, the bone structure in the pelvic phantom within the field was clearly visible in both sets of images (measured and simulated images) as shown in figure 5-14, 5-21, and 5-22. The field edges were detected and outlined as shown in 5-22. The measured IMRT EPID image of the pelvic phantom was calibrated using PMMA calibration phantom image. The simulated IMRT EPID image of the pelvic was calibrated firstly using the simulated PMMA phantom image and secondly, using the modified pelvic phantom image. The C-simulated image resulting from using the PMMA calibration image was of a poorer quality than the C-simulated image resulting from using the modified pelvic phantom calibration image. The correlation between the C-measured image and the C-simulated image using the PMMA calibration phantom and the modified pelvic calibration phantom was $r = 0.1$ and $r = 0.7$ respectively. These values indicate that there was a stronger match or similarity within the field between the two images when the modified pelvic calibration phantom image approach was used for calibration than when the PMMA calibration phantom image was used in the calibration. Therefore, the second calibration image approach was used for verifying the phantom position.

Both images were inspected visually showing no displacement that could be detected. The results of the position verification using the iView software (Table 5-6) shows that there was small residual horizontal displacement detected of ~ 0.5 ± 0.06 mm and 0.0 mm of

vertical displacement. These values were the estimated mean of the values of the four individual trials used to detect each error. Since there was no intentional error introduced to measured images, these displacements were caused possibly by other factors. The first possible cause was a residual error introduced by the phantom setup preparation procedure for fields delivery in the treatment room, lasers, or couch movement. Another possible factor is the inherent uncertainty in the matching process between the C-measured and C-simulated images using the iView software. The inherent uncertainty is an error caused by the software precision method of measuring these values. Different users could estimate this error using multiple trials or checks in performing the same measurement. On the other hand, contouring the bone structure and the field edges on the C-simulated image is a user subjective process. All these factors together could have contributed to the small residual displacements found. The four checks performed on both images showed that the anatomy displacement relative to the field edges was very small and close to the reference position. These results of the iView matching process agree with the visual inspection results.

Studies B and C investigated two entire IMRT plans. A prostate IMRT plan comprises five fields delivered to the pelvic phantom, and a head and neck IMRT plan contains seven fields delivered to the head phantom. Both IMRT fields were delivered at zero and non-zero gantry angles as per the plans using the step-and-shoot delivery technique. The IMRT fields were delivered to the calibration phantom at zero gantry angles. Both plans were simulated using EGSnrc. The results for measured images in both studies showed that the calibration procedure worked best at zero gantry angles C-measured images. They showed that it is possible to remove beam modulations from the IMRT images at all gantry angles. However, the C-measured images at zero gantry angles were of a superior quality images to the non-zero gantry angles in showing the bone structure clearly as well as the field edges. These images showed that beam modulations were removed, but no clear visibility of bone anatomy especially in Study B. This poor quality made it difficult to compare them with the C-simulated images. The correlation between these non-zero gantry angles C-measured images and the corresponding C-simulated images were in a range of $r = 0.2$ to 0.3. This indicates the poor match/similarity between the images within the field. The verification results in both studies showed good matching results in the iView using the

field edges in the MC reference image at least, despite the poor quality of the C-measured images at non-zero gantry angles.

The residual error detected in Study B and C for each field was very small, as shown in Table 5-7 and 5-8. In study B, the iView software was able to detect small displacements of ~ 0.1 mm horizontally and 0.06 mm vertically in the C-measured image with respect to the bone structure and field edges in C-simulated image (reference image). In study C, the smallest displacement detected was ~0.1 mm horizontally and ~ 0.2 mm vertically. The largest residual errors were detected at zero gantry angle fields delivery in both Studies B and C. The third field in study B, the horizontal displacement of the bone anatomy relative to the field edges reaches ~ 2.8 mm in x-direction and 0.8 mm in y-direction. In study C, the results (Table 5-8 and Figure 5-24) showed that the fourth field shows the largest horizontal displacement of the bone anatomy relative to the field edges, which was ~ 1.1 mm in x-direction and ~ 1.0 mm in y-direction. These displacements are most noticeable at $0°$, $90°$, $180°$, and $270°$ degrees. These detected displacements in both studies probably due to the setup process of the phantom in the treatment room attempting to achieve the same setup as the planning CT. The setup was performed separately for each field. This shows that there is a residual set-up error remaining in the measured EPID image caused by the lasers, couch movement, or the person performing the phantom setup on the couch in the treatment room.

The C-measured images at non-zero gantry angles in both studies B and C showed relatively poor quality images that were degraded by artefacts (i.e. blurring) affecting the visibility of bone structure within the field. These artefacts possibly caused by different possible issues:

1. The inaccuracy of the reproducibility of the EPID position is a main challenge especially using non-zero gantry angles for fields delivery. Moreover, the calibration images were acquired at zero gantry angles. Therefore, when applying the calibration procedure, possibly there was a mismatch between the IMRT EPID image of the phantom and the corresponding calibration image (field position mismatch). For the calibration procedure to work best, a high accuracy match between the treatment image (i.e. IMRT EPID image in these studies) and its corresponding calibration image must be sustained [4]. Hence, there were no similar artefacts observed in the zero gantry angles calibrated images that degraded the image quality. The mismatch

between the images indicates the sensitivity of the calibration method to any small displacement in the field position on the EPID (i.e. imager).

2. The artefacts (i.e. blurring) and degradation of soft tissue contrast in the images could be caused by X-ray scattering from the detector housing structure [150], and/or the sagging effect [151]. These images of non-zero gantry angles have a sag effect impacted on the quality of the C-measured images. The EPID sags due to its weight, and increases as a function of gantry angles. This EPID sag causes some small shifts in the radiation field position on the EPID [151, 152]. This shift in the radiation field position leads to discrepancies in the field's isocentre. In both Studies B and C, the EPID/gantry sag effect and/or MLC movement affected measured images at non-zero gantry angles. Therefore, when dividing these measured images of non-zero gantry angles by the calibration image (i.e. PMMA image) which had no sag effect due to the field's delivery at zero gantries, the images had some artefacts dominated the image that made the bone anatomy indistinctly visible at these angles. Hence, the zero gantry angle images showed better results due to the good match in the isocentre and field position in both images. The absence of the sag effect at zero gantry angle images (the IMRT EPID image of the phantom and the corresponding calibration image) justifies the good quality of the calibrated images in both Studies B and C, as well as for Study A, and supports the strong correlation between these images and the corresponding C-simulated images.

3. In study B, the pelvic phantom C-measured images showed poorer quality images than the C-measured images of head phantom in Study C. The head phantom (Study C) bony anatomy in the C-measured images can still be seen even in the worst quality image. The reason for this difference in quality, that the pelvis area is one of the most challenging regions to image using megavoltage energies radiation. This is due to the slight thickness of the bones in this region along with the large amount of soft tissue surrounding the bony structure. Consequently, bones and soft tissue absorb most of the low energies radiations that hold the effective contrast information, which leaves the intrinsically low-contrast megavoltage energies information [4]. As illuminated in Chapter Two, the contrast resolution of megavoltage EPID images is inherently lower in comparison with the kilovoltage images due to the reduced attenuation in the

images, as higher attenuation causes reduction in the contrast of the imaged anatomy. This supports the better images quality in the C-measured images of the head phantom in study C than the images in B study of the pelvic phantom at non-zero gantry angles. These images results also agrees with the previous studies recommendation of applying the calibration method to different disease sites other than pelvic will potentially give better results [4].

The calibrated simulated IMRT EPID images (C-simulated) in both studies B and C, were superior in quality to the C-measured images at all gantry angles. The C-simulated images did not show any artefacts similar to the C-measured images at non-zero gantry angles that degraded the image quality at any gantry angle. This indicates the high accuracy of field position match between the simulated IMRT EPID image and the corresponding calibration image (both images were simulated using the same gantry angles as per plan). Hence, the calibration procedure worked at all gantry angles. Another reason for the superior quality of the C-simulated images is that there is no electronic noise in the simulated images, since the electronics were not simulated. The calibration method removed beam modulations from the simulated images and the bone structure was clearly visible in addition to the detected field edges. These images were used as the reference image for the phantom position verification process. They were in qualitative agreement and of comparable quality with the C-measured images at zero gantry angles. The correlation between the C-measured and C-simulated images was calculated within the field and recorded at the zero gantry angles case in both studies. A strong correlation of $r = 0.83$ and $r = 0.80$ was found between these images in study B and C respectively. Figure 5-25 shows a comparison between the C-measured and C-simulated images at zero and non-zero gantry angles in both Studies B and C.

To improve the quality of the C-measured images at non-zero gantry angles, it is recommended some sag correction factors may be applied for both gantry and EPID to these images. Bone anatomy is expected to be more distinctly visible if these correction factors were applied. These correction factors were not applied to the measured images in this project, because these factors need to be calculated based on the reproducibility of values over a period using the same machine (linac). This was difficult to do due to the

limited access to the linac. Therefore, a different technique was used to investigate the poor quality of the C-measured images.
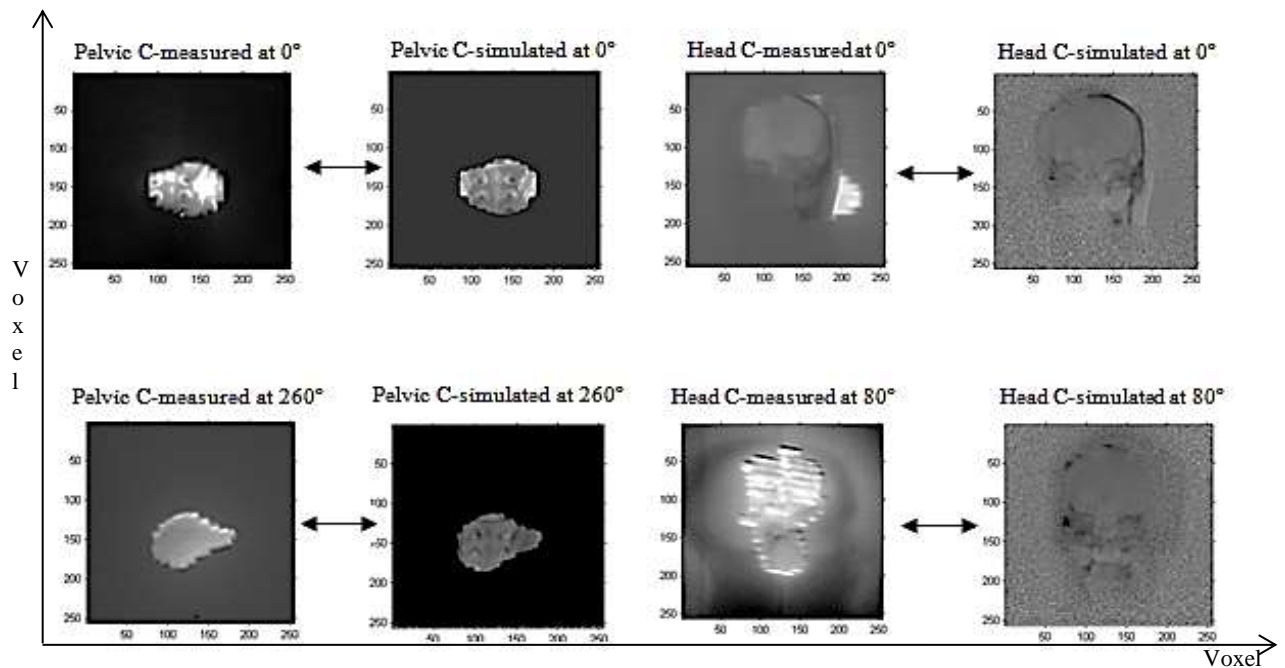
Figure 5-25: *Comparison between the C-measured and C-simulated images at zero and non-zero gantry angles resulting from Studies B and C.*

The results of Study D and E showed that measured IMRT EPID images could be calibrated via the division method at any gantry angle. Beam modulations have been removed from the images and the bone anatomy was visible in the thorax and head phantom images. There was a good agreement between the calibrated images of the same phantom using two different geometry (slab and cylindrical) calibration phantoms. These results were obtained using measured data of IMRT fields delivered via the Elekta Agility linac, which was recently installed and commissioned. These calibrated images signified that the poor quality of the C-measured images of the pelvic and head phantom at non-zero gantry angles in Studies B and C were caused by sag effects of the gantry, EPID, or MLC movement in the linac − and not because of the calibration method. Those sagging effects at non-zero gantry angles images caused a shift in the field isocentre with respect to the same field isocentre in the calibration images, since the calibration images were acquired at zero gantry angles, and therefore had no sag factor. The better quality images at all gantry

angles in study D and E are possibly justified by the different mechanical tolerances between the two linacs used. These tolerances were lower for the agility linac than the Elekta precise, because the agility was used for brain treatments. Therefore, more strict mechanical tolerances were required. The results of study D and E provides a justification for the poor quality of those C-measured images in study B and C. Moreover, the good quality images at zero gantry angles in those studies (A, B, and C) provide possible evidence of sag effect caused by the EPID. Consequently, a high level of accuracy in the treatment time image (phantom image during the fields delivery) and the calibration image field's isocentre is required for the calibration method to work effectively [4].

Based on the results of this study, the calibration method has removed beam modulation from the measured and simulated EPID images visualising the bony anatomy within the IMRT field as well as the field's boarders. The C-simulated images were in a superior quality to the measured images at all gantry angles. The C-simulated images were of useful quality for potential use as reference images for the set-up of the delivered treatment field verification during IMRT treatment using the visible stable bony anatomy as landmarks with respect to the field edges. These images showed clearly at least three visible stable bony structures within the field that could be outlined. These images are potentially useful for comparison with the treatment time images using offline patient position verification technique.

The bony anatomy in the pelvic in an anterior field, the sacrum, and part of the lumbar spine can be outlined in the C-measured images that were acquired during the IMRT treatment and compared with the corresponding C-simulated (reference image) of the same anterior field instead of using the simulated film image or the DRR image as a reference image. For the head phantom images, the orbital ridges, zygoma and frontal sinuses could be outlined and used for the set-up errors of the delivered treatment field. The other potential use of the C-simulated images is dosimetric verification of the delivered treatment field as well. To validate the results of this method and to test the sensitivity of using C-simulated images as a reference image for phantom position verification, intentionally introduced errors (translation and rotation errors) to the measured images were investigated and discussed in the following chapter.

Chapter 6: Detecting setup-errors in head and neck IMRT EPID images.

6.1 INTRODUCTION

In the previous chapter, the phantom's bone anatomy in the IMRT EPID images was revealed using a simple division method (pixel-by-pixel) for calibration. This chapter examines the ability to detect some intentionally introduced translation and rotation errors into the measured IMRT EPID images of a head phantom using the C-simulated image as the reference image. These introduced errors will be detected using three different methods. The measured image will be matched/compared with MC reference image. The sensitivity to detect these errors using each method will be investigated. Generally, EPIDs are used for the localisation imaging of bone anatomy with respect to the field in pre-treatment verification. The EPID images will be used in the verification process of the phantom position and set-up errors in this study.

In order to achieve dose escalation to the target volume using IMRT, it is important to reduce the uncertainties in the whole treatment process from the delineation of the target volume to the verification process of the patient set-up during treatment. The success of treatment is affected by delivery and positioning [3, 66, 153]. Target position uncertainties can be described in two forms: variations in the positioning of the patient's bone anatomy with respect to the beam are known as *set-up errors*, and variations in the position of the target within the patient with respect to bone structure are known as *organ motion*. This chapter investigates set-up errors using MC EPID images as a reference image.

The image-matching accuracy is a crucial part of QA programs implemented by radiation oncology departments, to ensure the images acquired are of a comparable quality for patient geometric verification [63]. Ideally, each part of the geometric verification process should be evaluated for any uncertainty within each part, to determine the total precision of the geometric verification process. Therefore, assessing the validity of the image-match data is a significant measure to calculate planning margins [154]. The geometric accuracy verification software/system can be evaluated in terms of the absolute accuracy, user accuracy, image registration technique, image processing and the consistency of output

[63]. The absolute accuracy can be measured by testing intentionally introducing known displacements data into the measured images and compare them with reference image (this case was investigated in this study). The user accuracy is evaluated to estimate the accuracy of the measurements among different users. The registration technique is used to measure the effect of different available registration algorithms on the accuracy of registration process. The image processing is used to assess how they affect the displacement results sometime. The consistency of output resulting from the verification systems is evaluated to measure how the accuracy of the conversion from 2D information to 3D movements and how limiting is the accuracy of the couch movements [63].

6.2 MATERIALS AND METHODS

6.2.1 Experimental Details

The same experimental materials and method used in the previous chapter for Study C was used in this study. The head phantom was scanned and the CT data consisted of 157 slices. The head phantom was irradiated with a 25×25 cm^2 square 6 MV photon field, and an IMRT field. For this study, field number four only from Study C involves 14 segments and 89 MU, was used and delivered using the step-and-shoot technique at zero gantry. As described previously, calibration EPID images were also acquired for the treatment field using a uniform density phantom of PW slab. Plastic water (PW) phantoms of different thicknesses were used to form approximately the same thickness of the head phantom, which was 15 cm. A reference EPID image of the head phantom using a 25 × 25 cm^2 field was acquired. The IMRT field was delivered to the phantom in the reference position (with no errors introduced). This image was the measured IMRT reference image. The phantom position was then translated laterally and longitudinally, and then rotated clockwise. First set of measurements comprised lateral errors of 1, 2, 5, and 10 mm were introduced by shifting the couch with the phantom to the left (–x direction). The second set of measurements involved introducing longitudinal errors of 1, 2, 5, and 10 mm by shifting the couch with the phantom forward (+y direction). The final set of measurements involved introducing rotation errors of 1° and 2° by rotating the couch clockwise.

These measured IMRT EPID images were acquired during the delivery of the IMRT field and then calibrated following the same calibration procedure detailed in Section 5.2.1.1.

Detecting setup-errors in head and neck IMRT EPID images.

The calibrated measured IMRT EPID images (C-measured) were compared/matched with the MC reference images (C-simulated) using various methods.

6.2.2 Monte Carlo Simulations

The main purpose in this section was to simulate the head phantom in the reference position. These simulation procedures are the same as in the previous chapter. The BEAMnrc code was used to model the linear accelerator head geometry used for delivering the IMRT fields. The phantoms were simulated in DOSXYZnrc. As with the previous chapter, the calibration phantom was the CT data egsphant file of the head phantom modified to create the egsphant file with a uniform density phantom. The same calibration method was used for the simulated IMRT image (detailed in Chapter Four).

6.2.3 Phantom position verification

The calibrated images (measured and simulated) were saved as PNG format files with 256 × 256 pixels, 8-bit images to allow them to be read and matched. The C-measured images of the phantom with translation and rotation errors were compared with the MC IMRT reference image using three different methods:

1. Visual inspection

This method was used to visually inspect and compare both the un-calibrated measured IMRT EPID images, calibrated images with the un-calibrated image, and calibrated reference image respectively. A group of five individuals (postgraduate students and a medical physicist) were asked to perform the visual inspection for all images by comparing the measured IMRT images with the MC reference image to detect any errors or differences between the images. Five individuals inspected these images to estimate the accuracy of the inter-user variability in the results of the visual inspection method.

A further visual inspection procedure was applied and performed by the same five individuals. The MC reference image was displayed and then the C-measured images with longitudinal errors were aligned with the MC reference image and a horizontal line was placed just above the maxilla bones in the reference image and extended to the measured image. The measured EPID image with 10 mm longitudinal shift was visually compared with the reference image. This procedure was repeated for 5, 2 and 1 mm longitudinal errors (+y direction). The same procedure was followed with lateral errors (-x direction).

The measured calibrated images with lateral errors were aligned with MC reference image. The vertical line was placed near the nasal bone, close to the eye outline towards the nose in MC image, and extended to the measured image.

2.   Maximum Linear Pearson Correlation (MLPC)Method

Analysis was performed using the same MLPC routine used and published previously by Fielding et al. to detect the errors in measured IMRT EPID images [3]. To summarise this procedure, the IDL (IDL version 6.3, Research Systems Inc. Boulder, Colorado, USA) code was modified to read two PNG format images where the first image was the C-simulated image (reference image) and the second image was the C-measured image. The MLPC routine was used to register and correlate the calibrated images. The region of interest (ROI) was defined by the user in the MC reference image within the field and away from the penumbra region, in order to make the bone anatomy dominant for the registration and not the field edges [3, 155]. The procedure was performed three times for each translation and rotation error and the mean and standard deviation were calculated. Each time the start point chosen (ROI) in the C-simulated image was in a different location, but still within the field, and the bone anatomy was chosen away from the field edge. The MPLC method performs a search of translation and rotation space to determine the best match defined in terms of the maximum correlation coefficient. This procedure performs the search for translation and rotation between the C-measured with respect to the C-simulated reference image by ± 20 pixels (1 pixel steps) and rotated by ± 2° in 0.25° steps. As a result, this procedure returns the longitudinal errors in pixels and centimetres, lateral errors in pixels and centimetres and rotation errors in degrees respectively. Moreover, it returns the maximum correlation between the reference image and the C-measured image that was caused by any translation or rotation of the phantom with respect to the IMRT field for the registration purposes of both images. Figure 6-1 shows a screen shot of the correlating process of the images using this method.

3.   The iView Software method

The iView clinical software was provided by Elekta for acquiring and matching EPID images. The image matching using this software has been described in detail in Section 5.2.3. The C-measured images with translational and rotational errors introduced were matched individually with the MC reference image to detect translation errors. No

rotational errors will be assessed in iView since it wasn't activated in the iView copy we had on hand. Figure 6-2 shows a screen shot of the images matching process using iView. The automated matching of both images in the iView returns quantitative values of the displacement between the reference image and the measured EPID image. The matching process uses the stable bony anatomy with respect to the field edges contoured in the reference image. Clinically, based on the position verification results of the iView the patient is adjusted to align into the reference position as required to deliver maximum dose to the target volume. The aim of this and the previous method is to test the sensitivity of the method to translation and rotational set-up errors using the C-simulated image as the reference image.

Figure 6-1: *a screen shot of MLPC method used for correlating the measured IMRT EPID image (right) with the MC reference image (left), showing the region of interest defined using a rectangle away from the edges of the field.*
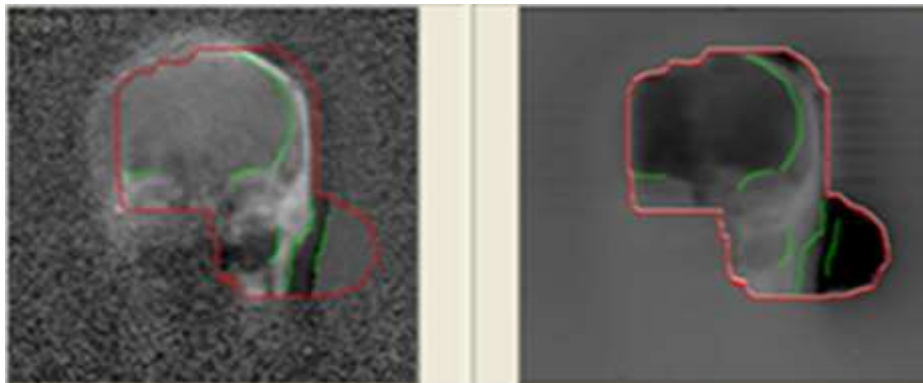
Figure 6-2: *screen shot shows the process of matching the anatomy and field edges in the measured image (right) with the MC reference image (left) using iView.*

6.3   RESULTS

6.3.1   Measured EPID images

The IMRT beam was first delivered to the phantom without introducing any translation or rotation errors, then 1, 2, 5 and 10 mm translation and 1° and 2° rotation errors were applied to the phantom. Figure 6-3(a) shows the un-calibrated measured IMRT EPID image with the intensity modulations of the beam mask the bone anatomy in the phantom. Figure 6-3(b) shows the un-modulated (open field) image which shows the entire head

phantom and the anatomy within. This image was used just to show the bony anatomy the head phantom comprises. Figure 6-3(c) shows the same reference measured IMRT EPID image after calibration using the division method (pixel-by-pixel). The greyscale pixels values in the calibrated images were inverted to improve the contrast of the bony anatomy. The C-measured images show the bony anatomy clearly as well as the field edge. The orbital ridges, zygoma, and nasal septum bones can be seen in the IMRT calibrated image Figure 6-3(c).
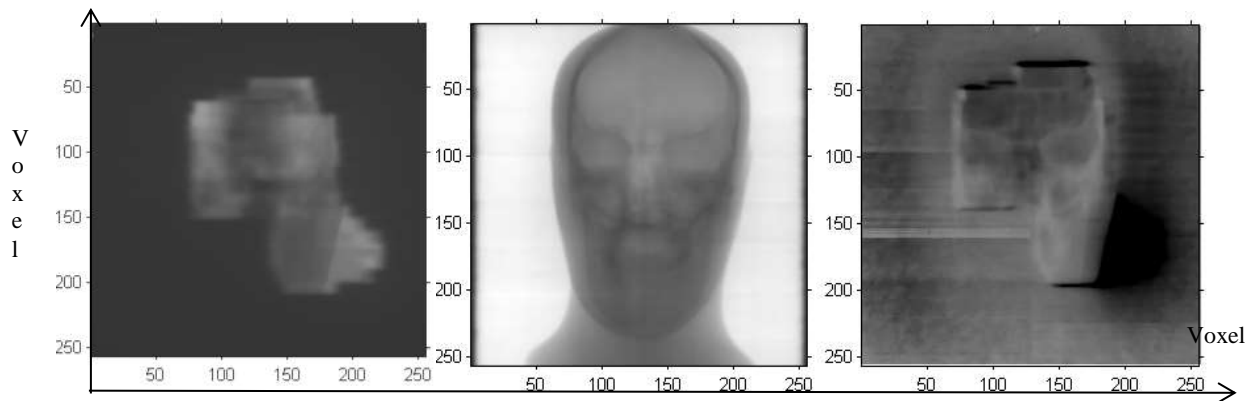
Figure 6-3: *a) IMRT un-calibrated measured image of the head. b) Measured image of the head phantom using 25×25 cm² field. c) IMRT calibrated measured image of the head phantom (no errors). The bony anatomy shown*

6.3.2   Simulated IMRT EPID images

Figure 6-4 shows the simulated IMRT EPID images of the head phantom before and after calibration. This C-simulated image is used as the reference image in this study. The bone anatomy in the head phantom that was masked by beam modulations was revealed after calibration.
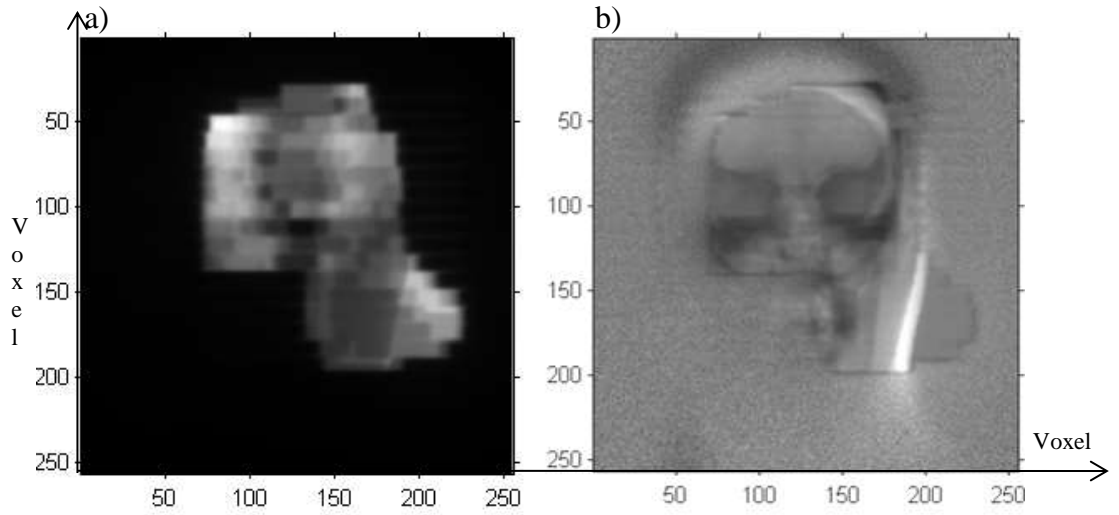
Figure 6-4: *a) simulated un-calibrated IMRT reference image of the head phantom. b) Simulated calibrated IMRT EPID image of the head phantom (MC reference image).*

6.3.3 Phantom position verification results

The C-measured images with translation and rotation errors were inspected and matched with the C-simulated reference image using the three methods detailed above:

6.3.3.1 Visual inspection

Figure 6-5(a) shows the MC un-calibrated reference image of the head phantom with the field edge contoured. The measured un-calibrated reference image 6-5(b), measured un-calibrated image with 10 mm lateral error Figure 6-5(c) and the measured un-calibrated image with 10 mm longitudinal error 6-5(d) are also shown. In all these images, the field edges were contoured and inspected visually. This inspection showed that even with the maximum translation error (10 mm) there was no observable difference between un-calibrated measured images and un-calibrated MC reference image.
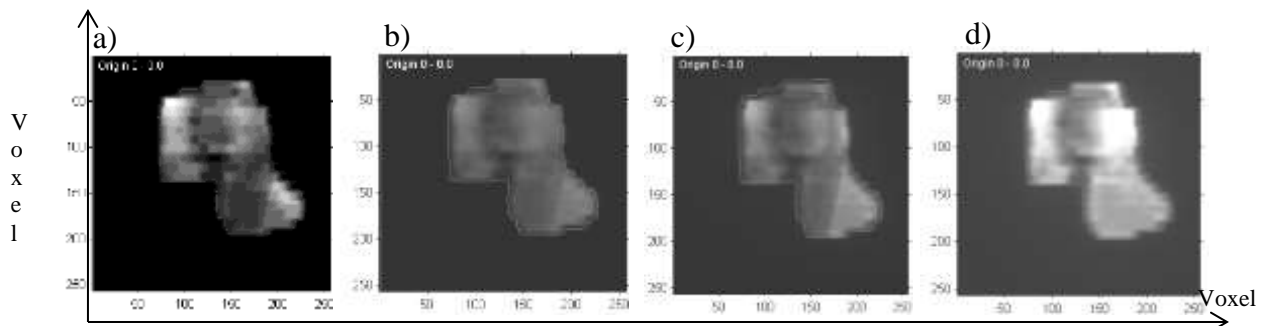
Figure 6-5: *a) MC un-calibrated IMRT image (reference image). b) Measured un-calibrated IMRT image (no errors). c) Measured un-calibrated IMRT 10 mm lateral error. d) Measured un-calibrated IMRT 10 mm longitudinal error.*

The images show no visible anatomy within the field due to beam modulations. Therefore, these images were calibrated as shown in figure 6-6. The calibrated measured and simulated images show the bony anatomy within the field clearly. The calibrated measured IMRT images with 10 mm translation error and the C-simulated (reference image) were contoured and visually inspected for any visible displacements. They showed no difference between images in terms of bone anatomy shift, even at the largest translation error of 10 mm as shown in Figure 6-6(a, b, c).
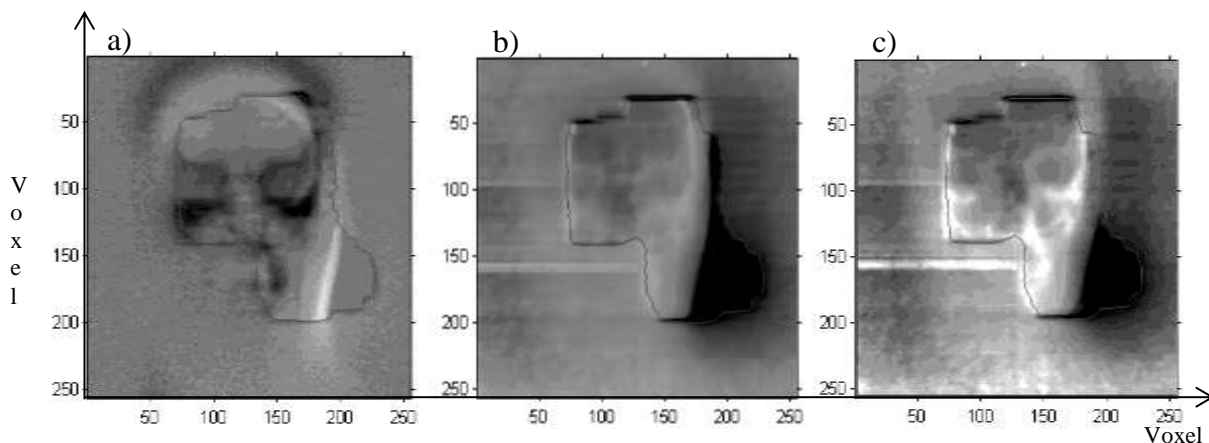
Figure 6-6: *a) The MC calibrated IMRT image (reference image). b) The C-measured image with 10 mm lateral error. c) The C-measured image with 10 mm longitudinal error.*

The C-measured images with longitudinal and lateral errors were aligned with the MC reference image. Figure 6-7(a) shows the reference image (no errors). Figure 6-7(b) shows the C-measured image with 10 mm longitudinal error. Figure 6-7(c) shows the C-measured image with 10 mm lateral error.

Horizontal and perpendicular reference lines (blue line) were placed at the left eye orbital ridges and the nasal septum as the reference points; to visually check for any lateral and longitudinal displacements. The position of the bone structure within the field has shifted up (+y direction) in the case of longitudinal errors with respect to the reference position (orbital ridge) in MC image as shown in Figures 6-7 (10 mm error). The same applies to the lateral errors, where it was visually observable that the position of the bone structure in the measured images shifted to the left (-x direction) in comparison with the reference position (nasal septum) in MC image as shown in Figures 6-8 (5 mm error). The visual method showed that shifts at 5 mm and greater were detectable visually as shown in the images in Figures 6-7 and 6-8. Translational errors of 1 and 2 mm were not observable

visually by our observers. Applying the visual analysis to the images containing rotation errors showed that rotations at 1 and 2 degrees were not observable.
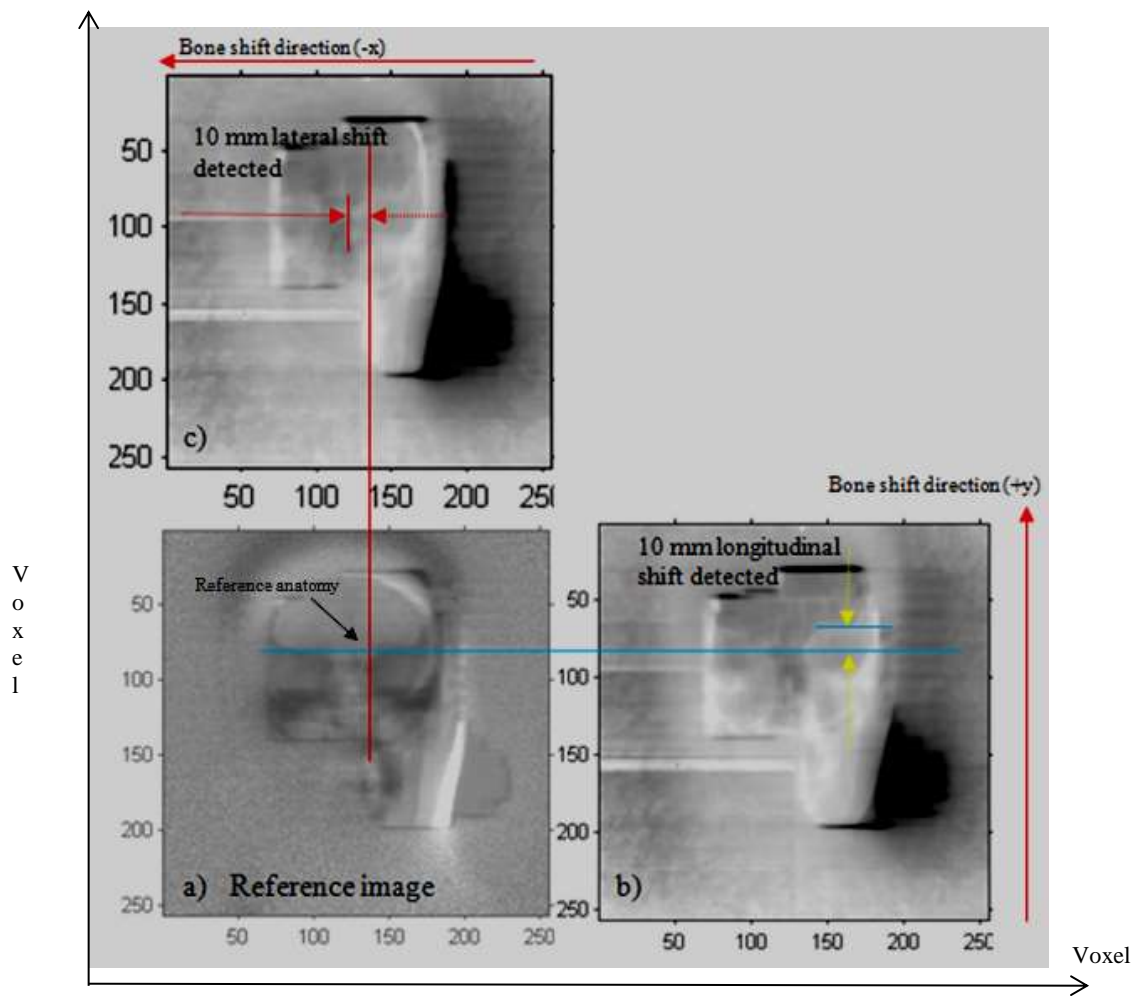
Figure 6-7: *a) MC calibrated IMRT image (reference image). b) Measured calibrated IMRT 10 mm longitudinal error. c) Measured calibrated IMRT 10 mm lateral error.*
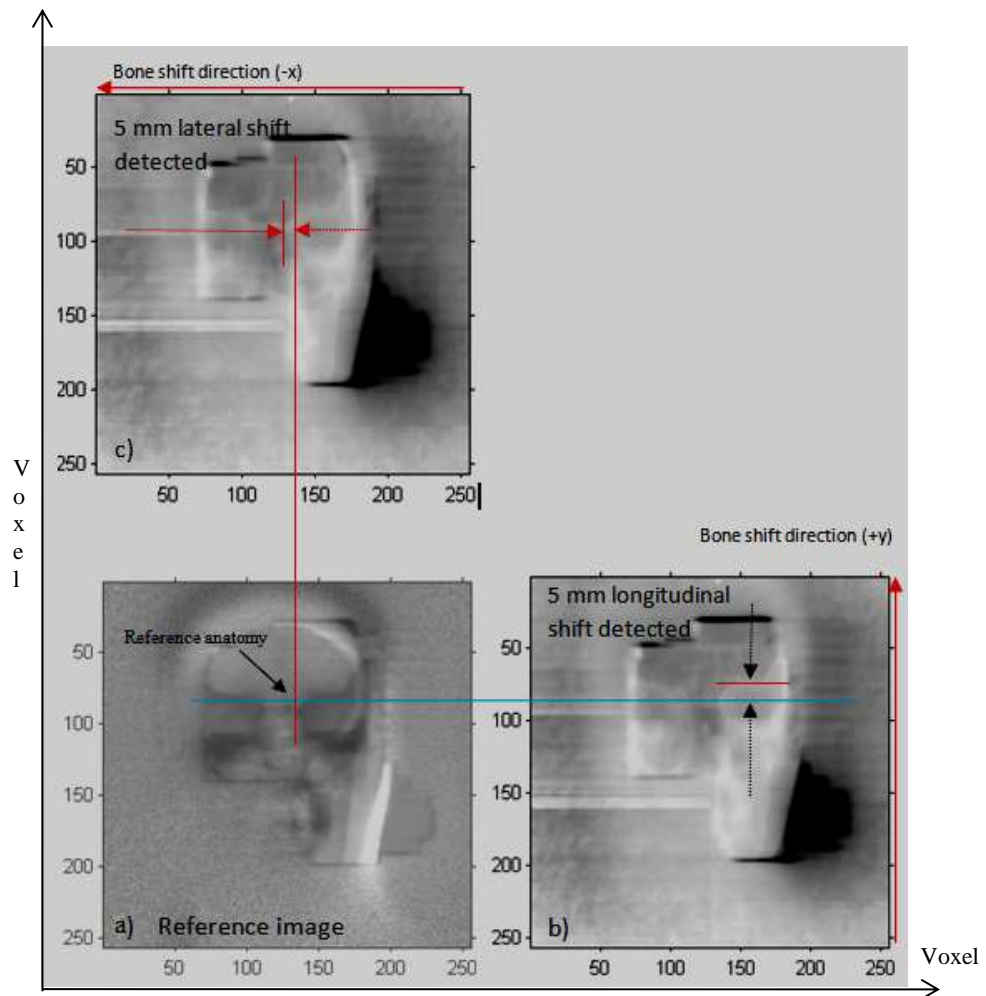
Figure 6-8: *a) MC calibrated IMRT image (reference image). b) Measured calibrated IMRT 5 mm longitudinal error. c) Measured calibrated IMRT 5 mm lateral error.*

6.3.3.2   MLPC method

The Maximum Linear Pearson Correlation (MLPC) method was used to detect translation and rotation errors in the C-measured images with respect to the MC reference EPID image. The C-measured images with the translation (10 images with: 0, 1, 2, 5 and 10 mm longitudinal errors, 0, 1, 2, 5 and 10 mm lateral errors) and rotation errors of 1° and 2° were correlated with the C-simulated reference image. The mean of these three values was calculated as well as the standard deviation (SD). The maximum Pearson Correlation values during the registration were recorded. The results of the detected translation errors are shown in Table 6-1, Table 6-2 and the detected rotation errors in Table 6-3.

Detecting setup-errors in head and neck IMRT EPID images.

Table 6-1: *The results of the Maximum Linear Pearson Correlation Method (MLPC) detecting lateral errors.*

MC Lateral shift (reference)	Introduced lateral shift	Detected lateral shift by MLPC (mm)		Pearson correlation between measured and MC
X (mm)	X (mm)	Mean	SD	r
0.0	0.0	0.0	0.0	0.89
0.0	1.0	-1.0	0.1	0.84
0.0	2.0	-2.1	0.0	0.78
0.0	5.0	-5.0	0.0	0.85
0.0	10.0	-10.0	0.2	0.81

Table 6-2: *The results of the Maximum Linear Pearson Correlation Method (MLPC) detecting longitudinal errors.*

MC longitudinal shift (reference)	Introduced longitudinal shift (mm)	Detected longitudinal shift by MLPC (mm)		Pearson correlation between measured and MC
Y (mm)	Y (mm)	Mean	SD	r
0.0	0.0	0.0	0.0	0.89
0.0	1.0	1.0	0.0	0.75
0.0	2.0	2.1	0.1	0.74
0.0	5.0	5.0	0.0	0.76
0.0	10.0	10.0	0.0	0.71

Table 6-3: *The results of the Maximum Linear Pearson Correlation Method (MLPC) detecting rotation errors.*

MC rotation error (reference)	Introduced rotation errors	Detected rotation by MLPC θ^o		Pearson correlation between measured and MC
(θ^o)	(θ^o)	Mean	SD	r
0.0	0.0	0.0	0.0	0.89
0.0	1.0	1.0	0.0	0.81
0.0	2.0	2.0	0.0	0.80

6.3.3.3 The iView software method

Finally, iView software was used to match the field edges and bone anatomy from the MC calibrated reference image and C-measured images with translation errors only, since the iView software is not capable of detecting rotation errors. The results of iView for detecting the translational errors are shown in Table 6-4 and Table 6-5. Each C-measured image was matched with the MC reference image three times. The translation errors detected using the iView method showed that there was agreement between the errors detected and the translational errors introduced to the measured images using the MC calibrated image as a reference image.

Table 6-4: *The results of the iView Method detecting lateral errors.*

MC Lateral shift (mm)	Introduced lateral errors in measured IMRT image	Detected lateral errors by iView method (mm)	
X (mm)	X (mm)	Mean	SD
0.0	0.0	0.0	0.0
0.0	-1.0	-1.0	0.1
0.0	-2.0	-2.0	0.0
0.0	-5.0	-5.1	0.0
0.0	-10.0	-10.0	0.0

Table 6-5: *The results of the iView Method detecting longitudinal errors.*

MC longitudinal shift (mm)	Introduced longitudinal errors in measured IMRT image (mm)	Detected longitudinal errors by iView (mm)	
Y (mm)	Y (mm)	Mean	SD
0.0	0.0	0.0	0.0
0.0	1.0	1.3	0.1
0.0	2.0	2.3	0.0
0.0	5.0	5.1	0.0
0.0	10.0	10.3	0.2

6.3.4 Comparison between MLPC and iView phantom position verification results

A comparison between the results of the MLPC and the iView was performed. Both methods successfully provided quantitative information on translation errors introduced to the measured phantom images. The means of detected translation errors from each method were plotted against the actual introduced translation errors to the measured images. The error bars are shown on the graphs as ± SD as shown in Figures 6-9 and 6-10.
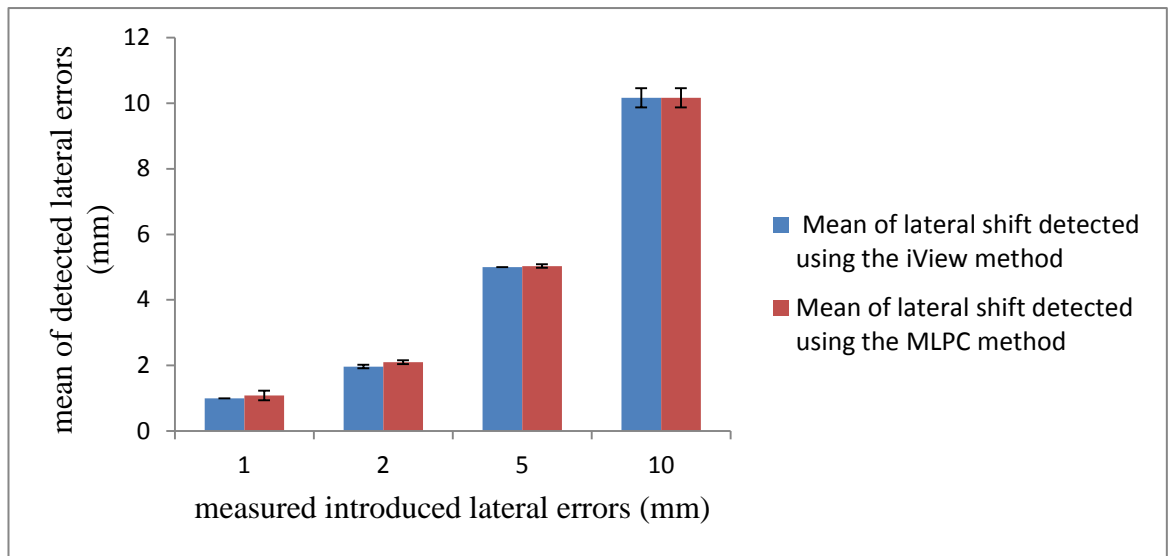
Figure 6-9: *Comparison between the introduced lateral errors means and the detected lateral errors means by MLPC and iView methods (±SD).*
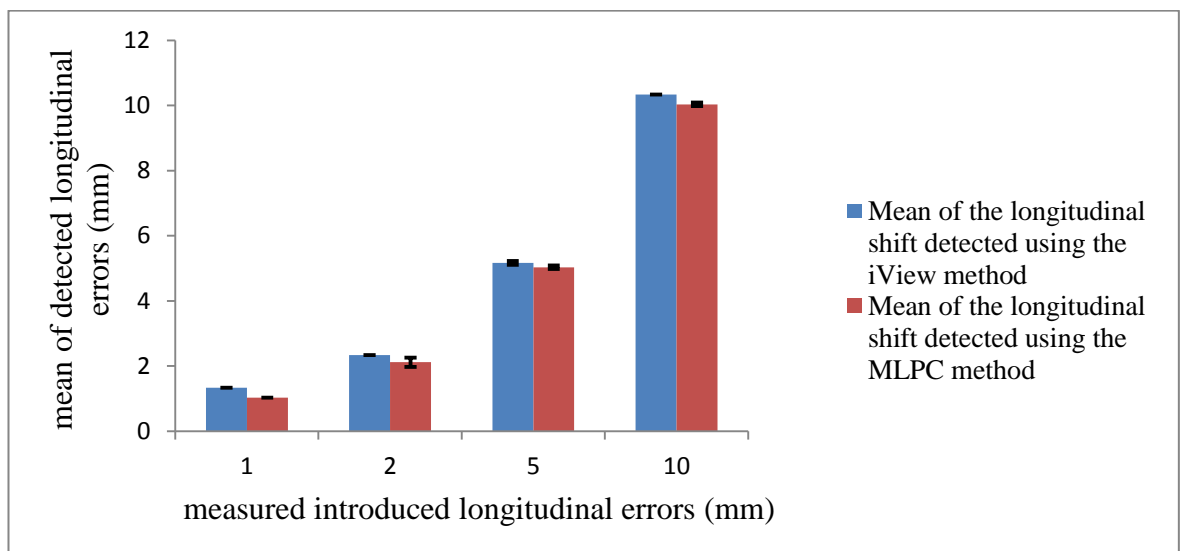
Figure 6-10: *Comparison between the introduced longitudinal errors means and the detected longitudinal errors means by MLPC and iView methods (±SD).*

Linear regression analyses were performed between the translation errors introduced to the measured images and the detected translation errors using both methods. The R^2, standard error, and the p-value were recorded for each method as shown in Table 6-6. The translation errors fit plots for each translation error from each method were plotted as shown in Figure 6-11.
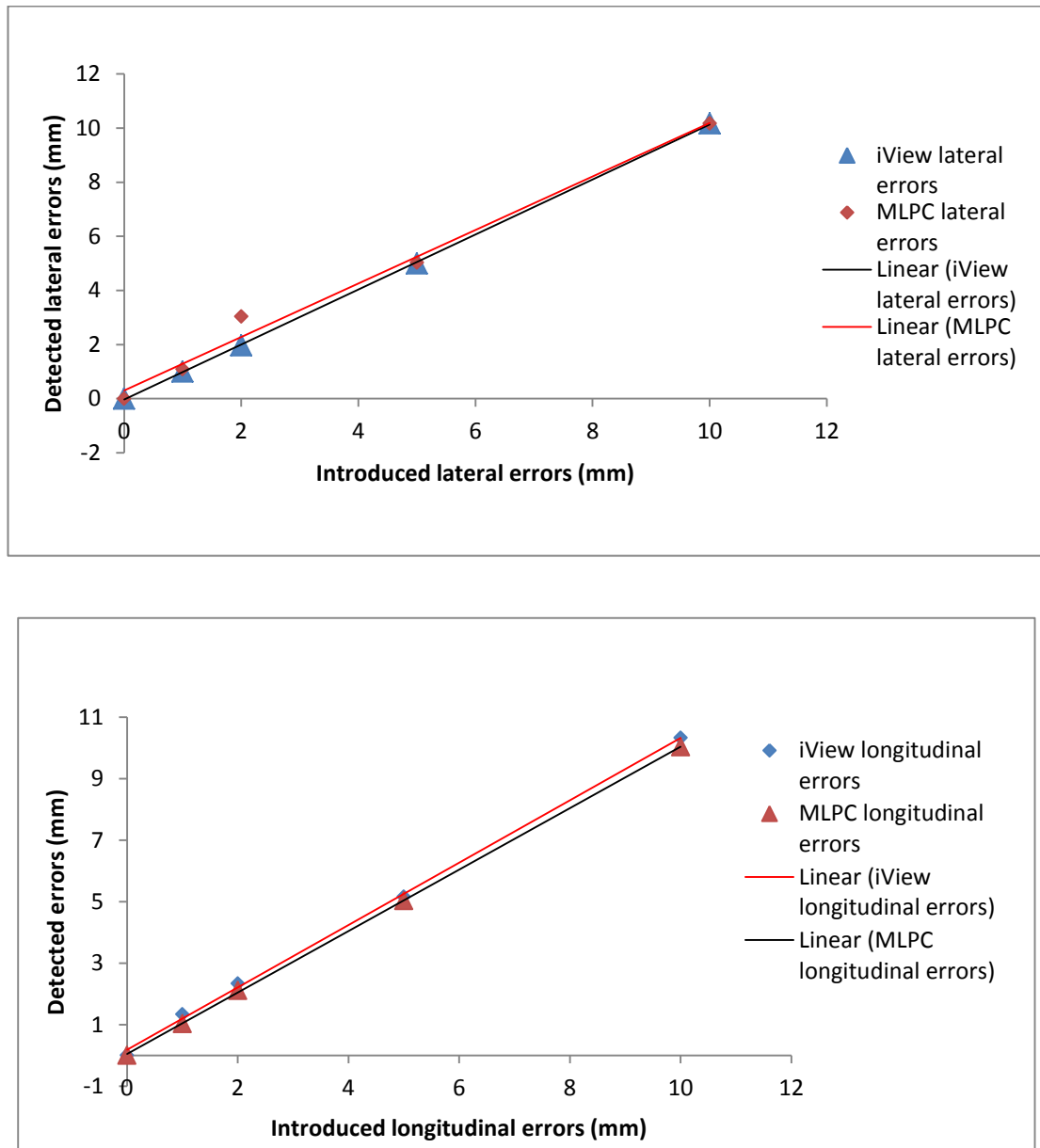
Figure 6-11: *The line fit plots of all the detected translation errors resulting from the iView and the MLPC methods against the actual introduced translation errors.*

Table 6-6: The linear *regression analysis between the actual translation errors introduced to the measured images and the detected translation errors using the iView and the MLPC methods.*

Regression statistics	Longitudinal error/MLPC	Longitudinal error/iView	Lateral errors/ MLPC	Lateral errors/ iView
R^2-value	0.99	0.99	0.99	0.99
Standard error	0.002	0.150	0.500	0.030
p-value	<0.005	<0.005	<0.005	<0.005

6.4   DISCUSSION

Measured IMRT field images of the head phantom with translation and rotation errors were acquired using the Elekta iView GT a-Si EPID during the delivery of the IMRT field. The predicted portal image of the IMRT field in the reference position was calculated. The measured and simulated images were calibrated using the division method.

The measured images with translation and rotation errors were visually compared with the simulated image after calibration for any observable shift in the bony anatomy or field edge in the measured image with respect to the reference image. The results showed that no translation errors were visually observable, until a reference line was placed on a reference anatomy point in the C-simulated image; then the C-measured images were aligned with the reference image, as shown in Figures 6-7 and 6-8. Translation errors of 5 mm and 10 mm were then observed in the C-measured images with respect to the C-simulated image. However, translation errors of 1 mm and 2 mm and rotation errors of 1° and 2° were not visually observable. The visual inspection proved that large translation errors of 5 mm or greater were observable, but this method did not provide any quantitative information. Therefore, the MLPC and iView methods were used to compare/match the C-measured images with the C-simulated image (reference image) to provide quantitative information.

The MPLPC method was first used to determine the quantative information of translation and rotation errors in the measured images. This method successfully was able to detect the smallest translational errors to an accuracy of 1 mm. Moreover, the method was able to detect the smallest rotational error introduced to an accuracy of 1° without affecting the results of the translation errors. The iView method then was used to detect the magnitude

of the translation errors in the measured images using MC reference image and to confirm the quantative results of the MLPC method. This method was successfully able to detect all translation errors introduced to the measured images to an accuracy of 1 mm. The phantom position verification results of both methods were in agreement with the results of similar previous study [3]. The difference between this study and the previous study was the reference image used for phantom position verification, which was the calibrated MC predicted portal image in this study.

A comparison between the results of both methods was carried out. The measured translation errors detected by both methods were in excellent agreement, as the results show in Table 6-1, 6-2, 6-4, 6-5 and Figure 6-11. The correlation between the detected translation errors from each method and the introduced errors data was 0.99 and 1 respectively. These values indicate the strong agreement between the results of both methods. The error bars shown on both graphs 6-9 and 6-10, overlap indicating that the difference between the means of detected translation errors and the introduced translation error is very small. Therefore, the results of both methods were in good agreement. However, one point at 2 mm lateral error in the MLPC method shows a difference of ~ 1mm as shown in Figure 6-9. The reason for this difference could be that when defining the ROI with the bone anatomy in MC reference image in MLPC method, the area could have been outlined closer to the penumbra region of the image. The linear regression analysis shown in table 6-6 indicate that the good agreement between the detected translation errors and the introduced errors of both methods.

The results of the phantom position verification in this study using MLPC and iView methods signify the comparable quality of the calibrated measured IMRT EPID images and the calibrated calculated MC predicted portal image for phantom position verification during IMRT treatment. Clinically, the daily geometric errors (systematic and random errors) calculations are used to develop offline and online correction protocols to ensure maximum dose delivery to the target volume and minimal dose to surrounding normal structure [3]. This is usually performed using two orthogonal EPID images to evaluate the systematic errors [63, 68, 154] with respect to reference image (DRR or simulator image). The orthogonal images usually acquired immediately before the treatment within minor frame from each other to verify the accuracies in all three directions. The ideal information about the patient position is that reported during the treatment. The measured images in

this study were acquired during the field delivery. These calibrated images (treatment time images) were of a comparable quality to the pre-treatment orthogonal images. These images contain useful anatomy information that could be potentially used to detect the displacements and used to determine the corrective couch movements needed for repositioning the patient similar to the pair of orthogonal images [63].

The calculated predicted portal image of MC was calibrated and used as the refrence image for the phantom position verification. The C-simulated image and the C-measured images were of a comparable quality enough to detect the intentionally introduced translational and rotational errors. In both images after calibration, they contained visible stable bony anatomy along with the field edges that were used to detect the translation and rotation errors.

The localisation accuracy is controlled by the imaging information such as the phantom positioning and repositioning for imaging [82]. This accuracy could be influenced by the imaging software that is used for the position verification. Therfore, the absolute accuracy of the methods used to verify the phantom position in this study was tested by analysing known translations and rotations introduced to the measured images through the couch movement with the phantom on it. Both phantom position verification methods were able to detect translations errors to an accuracy of 1 mm. The MLPC method was able to detect the rotations errors with an accuracy of 1°. The results of translations errors detection accuracy of 1 mm, were comparable with the geometrical accuracies that could be detected by various IGRT technologies [81]. In 2013 a pubished report reviewd the localization and delivery in radiotherapy using radiation and non-radiation based IGRT technologies [81]. For radiation-based systems, it was reported that the geometric accuracy using EPID kV 2D planner is 1-2 mm when bony anatomy is used as landmarks for setup verification. The steroscopic kV imaging (Cyberknife, BrainLAB/Novalis) geometric accuracy is < 1mm, when bony anatomy are a good surogate for target localization. The kV or MV CBCT geometric accuracy is ≤1 mm [81, 156]. For non-radiation- based systems, ultrasound system (BAT, SonArray) images are used to align the target to decrease the interfraction set-up errors with geometric accuracy of 3-5 mm. the camera-based systems (AlignRT) is used for surface-based localization with geometric accuracy ranges from 1-2 mm. The non-X-ray 4D tracking systems (Calypso) use electromagnatic transponders implanted in the

target volume (e.g. prostate) to improve the set-up accuracy and to monitor the intrafraction motion of the target [81].

Based on the results of the set-up errors detected using the methods presented in this study, the methods (MLPC and iView) are suitable for the verification of IMRT field of Head and neck in this study. Both methods were sensitive enough to detect the same translation errors of 1 mm. The MLPC method was sensitive enough to detect rotation errors of 1°. These results were detected in the calibrated measured IMRT EPID images using calibrated MC predicted portal image. Therefore, the quality of the calibrated measured and simulated images were of enough comparable quality to detect the translation and rotation errors during IMRT treatment. The results of this study signifies the potential use of the methods in off-line or on-line patient position/set-up errors verification during IMRT.

6.5 SUMMARY

This chapter has investigated the sensitivity of phantom position/set-up errors verification during IMRT delivery using the step-and-shoot delivery technique of head and neck IMRT field EPID images. Translation and rotation errors were introduced to the field images and acquired during the field delivery. The simulated IMRT field image of the head phantom was calculated in the reference position (predicted MC image). These images were calibrated using the division calibration method. The measured calibrated images were compared with the predicted calibrated image of MC (reference image) to detect the introduced set-up errors using visual inspection, MLPC and the iView method.

On visual inspection, no translation or rotation errors were observable, even at the maximum translation errors (10 mm). When a reference line was placed on a reference bone anatomy and the visual inspection was repeated, translation errors of 5 mm and above were observable. The MLPC and iView used for phantom position verification showed that both methods were sensitive enough to detect the smallest translation error of 1 mm. The MLPC method was sensitive enough to detect the smallest rotation error of $1°$. These results make the MLPC method a potential useful tool for position verification alongside the iView and other currently available tools for patient position verification. The quality of the C-simulated image qualifies it to potentially be used as the reference image in patient position verification during the IMRT. This image and the software tools used in

the position verification in this study have the potential to be used as an extra verification tool along with currently available protocols for patient position verification.

Chapter 7: Conclusions and Future Work

7.1 DISCUSSION AND CONCLUSIONS SUMMARY

IMRT has in the past decade become the state of the art of radiotherapy modalities used in cancer treatment. The escalated dose to the target and the reduced toxicity that can be achieved make it the treatment of preference for many cancers. The complexity of treatment requires more complicated procedures for the entire treatment process; from planning to the delivery. Planning procedures are required to ensure the delivery of the intended dose to the treated volume. This is achieved via dosimetric and geometric verification. The latter was the concern of this study.

Verification images acquired pre/post and ideally during treatments are very informative of the patient's position at the time of treatment. They give information about any changes in the size of the tumour, set-up errors and patient position, and internal organs motion. The patient's position/set-up errors verification process ensures the geometric accuracy to deliver the maximum dose to the target and provide better protection of vital organs and healthy neighbouring tissue. This issue is more important in IMRT than conformal radiotherapy because of the escalated doses via this modality. IGRT has reduced the toxicity and improved the intended dose delivery to the target volume via different imaging technologies (kV and MV- based CT or non-radiographic techniques) coupled with the linacs [84].

The aim of this study was to generate a calibrated MC predicted portal image using a-Si flat panel EPIDs as a verification image during the IMRT treatment. Making this image available allows it to be used as a potential reference image for patient position/set-up errors verification during IMRT treatment. This image and the phantom position verification methods used in this study should complement currently available patient's position verification procedures in IMRT treatment.

The motivation behind this project is that anatomical imaging during IMRT treatment is difficult due to beam modulations that mask the internal anatomy of the patient, making the imaging difficult. Previous studies by Fielding et al. in 2002 and 2004 [3, 4] showed the feasibility of imaging and calibrating the measured IMRT EPID images during IMRT.

The calibration method successfully removed beam modulations from those images, but Fielding did not have a reference image to compare them with. Fielding et al. suggested the use of a DRR image from the planning CT data or the use of predicted portal image using MC techniques for the analysis of systematic errors in patient set-up verification [4]. Therefore, this project aimed at generating this predicted portal image (C-simulated image). Moreover, the MC methods and the images are known as the "gold standard" for improving the accuracy of dose delivery in radiotherapy. This MC image could be used in the dosimetric verification process pre/post the treatment in addition to geometric verification use as shown by previous studies [157-159]. On the other hand, IGRT technologies are associated with expensive costs and the need for expertise in their use that limit their availability in many clinical environments around the world [84].

This project involved three stages where seven studies in total were carried out investigating the calibration of IMRT EPID images, both measured and simulated. The first stage investigated the ability of MC codes to simulate simple and clinical IMRT fields EPID images via step-and-shoot delivery technique. This stage was a proof of principle for developing IMRT field EPID images and the calibration of these images using the division method. The calibration image used was a PMMA slabs phantom with a thickness corresponding to the phantom thickness. The MC code EGSnrc and its associated user codes BEAMnrc and DOSXYZnrc were used to generate a simple IMRT field (square fields) and a clinical IMRT field (prostate IMRT segments) image. The simulated images were calibrated providing an evidence that the calibration of those simulated images was feasible and beam modulations that masked the lung anatomy were removed visualising the lung anatomy clearly from the model lung phantom used. The quality of both calibrated MC images showed a visible lung anatomy in the calibrated MC images as well as the fields edges. These images were of a quality that allowed for a clear visual outline of the lung and the field edges. The results of this stage were a proof of principle of developing a MC image of a comparable quality to be used as a reference image.

The second stage involved five studies (A, B, C, D, and E) investigating more complex clinical IMRT fields using various humanoid phantoms (i.e. head and pelvic) and different calibration phantoms geometries (PMMA slab, PW slab, cylindrical geometry). The effect

of delivery at zero and non-zero gantry angles on the calibrated images, both measured and simulated was investigated as well.

Study A investigated a prostate IMRT field delivered at zero gantry angles to a pelvic phantom and PMMA calibration phantom. The field was simulated as well as the PMMA calibration phantom. Another approach of calibration phantom (modified CT data of the pelvic phantom) was simulated and the images resulting from both calibrations using both calibration phantoms were compared. The results showed that the quality of the C-simulated image resulting from using the modified CT data as a calibration phantom was of a better quality than the calibrated image resulting from using the PMMA calibration phantom. The pelvic phantom position was verified using C-simulated image as a reference image in the iView. The results showed that there was an estimated mean of ~ 0.5 mm residual error of horizontal displacement detected and an estimated mean of ~ 0.1 mm of vertical displacement. These displacements could be justified as a residual error caused by either setting up the phantom in the treatment room, lasers, or couch movement.

Studies B and C investigated two IMRT plans prostate (five fields) and head and neck (seven fields). Both treatment fields were delivered to head and pelvic phantoms respectively. The resulting images were calibrated using PW slabs phantoms of uniform density material. Both treatments were simulated and the calculated images were calibrated using the modified CT data of each phantom. The measured results showed that it was feasible to remove beam modulations from the IMRT EPID images. The field edges were detectable and were outlined. The C-measured images at zero gantry angles were of a superior quality to those measured at non-zero gantry angles. The C-measured images at non-zero gantry angles in both studies showed poor quality images. The poor quality of these images made it difficult to compare them with C-simulated images. the feasibility of the calibration of those images were in agreement with previous studies [4, 142].

The head and neck fields (Study C), showed that the bone anatomy could still be seen even in the worst quality image due to less tissue structure and more bone anatomy in the head region in comparison with the pelvic phantom images (Study B). The reason for the better quality images of the head phantom at non-zero gantries in comparison with the pelvic phantom images is that contrast in the pelvic images is inherently poorer than the head images. That is because the pelvic region is one of the most difficult regions to image due

to the large tissue structure surrounding a relatively thin bone structure, causing low contrast in the pelvic images. There were other possible factors causing the poor visibility of the bone anatomy in the images, including EPID and gantry sags and/or MLCs assembly movement. The artefacts left in the C-measured images possibly were due to the inaccurate reproducibility of the EPID position as well. Previous studies showed that the EPID could sag on due to its weight and gravitational forces, causing some small shifts in the radiation field position on the EPID [151, 152]. This sag effect was found to be a function of the gantry angles. The studies found that the maximum gantry sag varied from 0.7 to 1.0 mm when the movement was inferior to the source with rotation from 0º to 180º, depending on the linac and the collimator angle, which leads to variation in the field isocentre [151, 152]. Another study was carried out in 2010 by G. Herman [160] studied MV and kV images, showed that the mechanical flex of the gantry and the imager attached (i.e. EPID) leads to certain offsets in the isocentre localisation images as a function of gantry angles. Both kV and MV offsets ranged between 1.5 mm and 0.5 mm. The agreement between both images was in the order of 0.7 mm. These previous studies relate to this study in the point that the imager could sag due to the gravitational forces and impact on the EPID image quality, in addition to the accuracy of the EPID position reproducibility. Therefore, the method worked best at zero gantries for the measured image calibration since no sag effects were noticeable and the bone anatomy was clearly visible in those images.

The C-simulated images in both studies were superior in quality to the C-measured images at all gantry angles. The bone structure was visible and field edges were detectable and could be outlined. These images were used as the reference image for the position verification of the phantom. A stronger correlation between the C-measured and C-simulated images has been found at the zero gantry angles case in both studies. The phantom position verification results in both Studies B and C showed good matching results in iView with respect to the field edges in the MC reference image. These results showed that despite no introduced set-up errors, a small residual error for each field was detected using the iView software. This error was caused either by the couch movement, lasers, or during the setup process of the phantom in the treatment room. The matching process in the iView and the manual contouring of main bone structure and field edges was another possible cause for the residual errors detected.

Studies D and E investigated further the poor quality of the C-measured images at non-zero gantries. IMRT fields were delivered to thorax and head phantoms. Two different geometries calibration phantoms were used, a slab phantom and a cylindrical geometry phantom. The IMRT EPID images of the thorax and head phantom were calibrated using both calibration phantoms in the division method. The resulting images of the calibration in each case using the different calibration phantoms gave comparable quality images. The C-measured images showed the bone anatomy and the field edges. The linac used in this study was an Elekta Agility, which was recently installed and commissioned. The results showed that it was feasible to calibrate the measured IMRT EPID images at any gantry angle as per the simulated images in Studies B and C using a uniform density material calibration phantom with thickness corresponding to the phantom thickness used.

When comparing the results of Studies D and E with the measured results of Studies B and C, there was a strong indication that the C-measured images of B and C at non-zero gantry angles were of poor quality due to some sag effects that caused a mismatch between the field's isocentre in the humanoid image and the calibration image. The sag effect was not noticeable in the non-zero gantry angle images in Studies D and E. The reason is possibly that the machine used in Studies D and E was new technology and recently installed and commissioned. In addition, the isocentre and mechanical tolerances of the Agility was better than the Elekta precise because it was used for stereotactic treatments.

The final stage of this project investigated the sensitivity and the absolute accuracy of the phantom verification methods (MLPC and iView) by introducing translational and rotational errors into the measured IMRT EPID images. The C-simulated image was used as a reference image to detect these introduced errors using three different methods – visually, MLPC, and the iView – and their sensitivity in detecting these errors. The results of this study showed that, visually, translational errors of 5 mm and 10 mm were observable in the images with a reference line on reference bone anatomy used, but neither rotational errors nor 1 mm or 2 mm translation errors were visually observed. The MPLC method was able to detect the smallest translation and rotation errors of 1 mm and $1^{°}$ respectively. The iView method was able to detect the smallest translation error of 1 mm. When the quantitative results of MLPC and the iView were compared, the correlation between the results data was $r \approx 1$, which indicates an excellent agreement between both methods. This signifies that both methods are reliable methods for position/set-up errors

verification using C-simulated images as reference images. The results in the final study of the MPLC method were in agreement with the results previous researchers showed in 2004, when the method used by Fielding et al [3] was able to detect the smallest translation and rotation errors introduced to the IMRT measured image. The accuracy of these methods in detecting the smallest set-up errors introduced into the measured images was comparable with geometrical accuracies of various IGRT systems reported in the literature [81, 156, 161]. The kV EPID systems have a geometrical accuracy of 1-2 mm, stereoscopic kV imaging systems (Cyberknife, BrainLAB/ Novalis) geometrical accuracy < 1mm, Cone-beam CT $\leq$ 1 mm, CT-on-rails and MVCT $\leq$ 1 mm. Ultrasound 3-5 mm, Camera based system 1-2 mm and Calypso < 2 mm [81, 156, 161]. These results imply the good comparable quality of the calibrated measured IMRT EPID images acquired during the field delivery (treatment time images) and the calibrated MC IMRT EPID images (reference image). Therefore, the proposed imaging procedure and the calibration method followed in this study has the potential use clinically to complement the available off-line verification imaging protocols for analysing the systematic errors of patient set-up during the treatment and adjust the patient position if needed in the subsequent fraction.

Systematic set-up errors (SSE) are very important to review accurately within an appropriate number of fractions in order to estimate true systematic error and correct it. By implementing the proposed verification procedure in this study clinically, potentially the SSE can be evaluated over a number of fractions during the IMRT for geometrical accuracy. This can be achieved from this procedure by turning the EPID on during the treatment for the IMRT field images to be acquired. These measured images can then be calibrated using the division method. These images will be collected over 3-4 fractions so that systematic errors can be calculated and corrected.

To correct for SSE, two possible strategies are used, the no action level (NAL) and the shrinking action level (SAL) [63]. In NAL, the systematic error is calculated after 3-4 fractions and the correction is performed. This approach does not define an action level for corrections. However, an extended NAL recommends acquiring a weekly image in addition to the images of the first 3-4 fractions. If the verification results of set-up errors are within tolerance there will be no action, otherwise, more images are acquired to calculate the systematic error. SAL uses an action level that reduces depending on the

numbers of fractions imaged. The mean error over all the images acquired is compared with the current action level. The set-up for the treatment will be adjusted if the mean error is larger than the action level [63].

7.2 IMPLEMENTATION OF THE PROPOSED VERIFICATION PROCEDURE

The patient position/set-up errors verification during IMRT using calibrated MC predicted portal images as reference images has the potential use and implementation clinically. This procedure would support and complement available patient position/set-up errors verification procedures during the treatment course offline. The implementation of this proposed imaging procedure potentially will allow the SSE to be evaluated over a number of fractions during the IMRT patient set-up. Firstly, the MC predicted portal images need to be simulated and calibrated to be used as the reference image. Then, once the IMRT treatment commences the EPID need to be turned on for the duration of the fraction to acquire the IMRT field images of the patient. These images to be calibrated by a calibration image, which should have been prepared before the treatment commences. These images will be collected over 3-4 fractions so that systematic errors can be calculated and the patient position corrected as needed in the subsequent fraction. The clinical implementation of this imaging procedure for geometrical accuracy of the patient is shown in figure 7-1.

PRETREATMENT

Simulate the IMRT fields, simulate the EPID images and calibrate the image of each IMRT field (C-simulated image). Use the C-simulated image as a reference image

Acquire IMRT EPID calibration images before the treatment starts using the treatment IMRT fields.
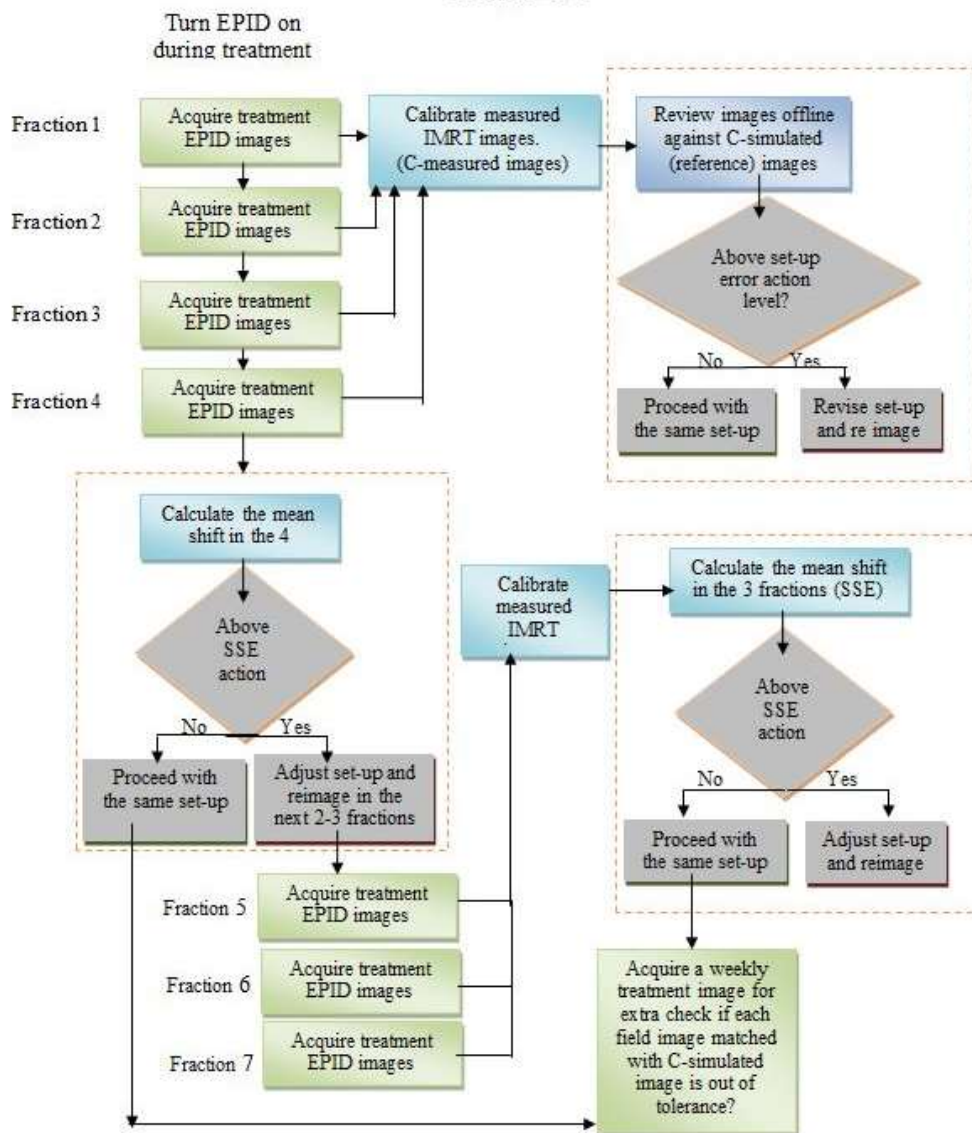
Figure 7-1: *The proposed patient position/set-up errors verification during IMRT using the C-simulated images as a reference image.*

Finally, the results of all the studies in this thesis showed the feasibility of calibrating measured and simulated IMRT EPID images using the division calibration method. Both images contained a useful bone anatomy and field edge of sufficient comparable quality to verify the patient position during IMRT treatment off-line, using the verification methods described in this thesis. The calibrated MC predicted portal images were of a superior quality to the calibrated measured IMRT EPID images that qualifies them to be used as a reference image. The geometric verification methods used in this study to verify the phantom position showed a geometric accuracy of 1 mm (translation error) and 1° (rotation error), that is comparable to various available IGRT systems. These images and verification methods should potentially complement currently available position verification protocols to assist in evaluating the systematic set-up errors using the proposed imaging procedure described in this thesis. Moreover, these MC portal images generated in this study could be used in dose verification pre/post the treatment since they also carry dose distribution information at different depth in the patient.

7.3   FURTHER WORK

1. Use the methods and procedures in this study on more tumor sites such as breast, brain, and lungs and investigate more IMRT plans.
2. Investigate the evaluation of SSE for patient set-up using the proposed verification imaging procedure described in this thesis.

Appendices

APPENDIX 1

The MC model of the Elekta Precise linear accelerator was commissioned using 6 MV energy with all the head geometry included as per the manufacturer specifications. The equivalent energy was found to be 6.2 MeV with 1% uncertainty based on the agreement between the measured and simulated results match using the Chi square statistical method for the evaluation of agreement. The PDDs and profiles of both measured and simulated images were matched in the reference field (10×10 cm^2) first. To verify the results of matching of the reference field, a set of square fields (3×3, 5×5, 15×15, 20×20, and 25×25 cm^2) were simulated and the results were matched with measured data as shown below. The PDDs and the profiles of the square fields were matched as shown below.
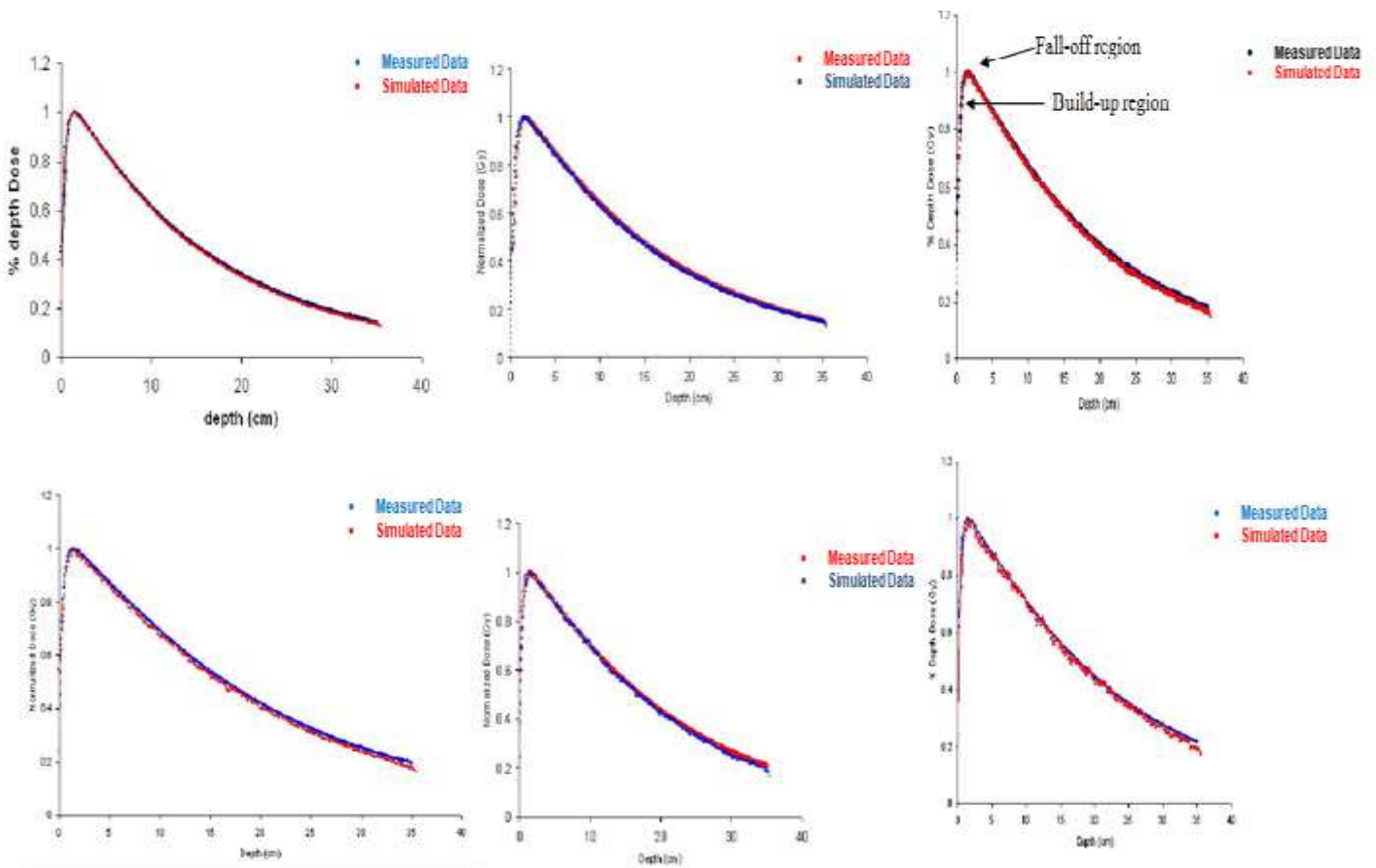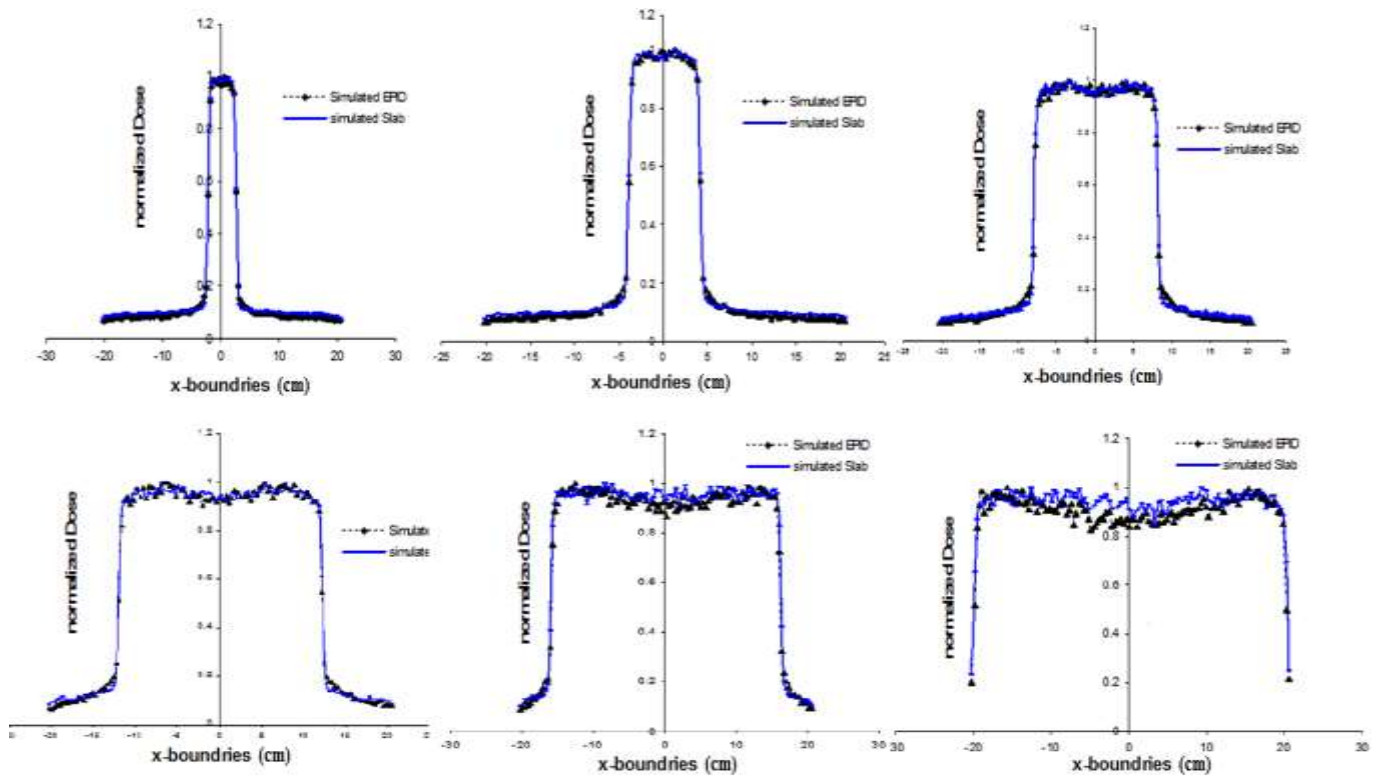
APPENDIX 2

This in-house matlab code is written to sum 3ddose files resulted from simulating each segment of the IMRT field and writes the output combined 3ddose in the same format of the 3ddose file. This file was used to extract the simulated IMRT EPID image of each field.

```
================================================================
[filename,pathname,filterindex] =
uigetfile({'*.3ddose'},'MultiSelect','on')

nsegments = length(filename);
fprintf('Reading file 1: %s\n',filename[1]);
[dose,dose_error,vx,vy,vz] = read_3ddose([pathname,filename[136]]);

nx0 = length(vx)-1;
ny0 = length(vy)-1;
nz0 = length(vz)-1;

nx = nx0;
ny = ny0;
nz = nz0;

doseSumError = dose;
doseSum = dose_error;

ix = 2;
```

```
while (ix < nsegments)
    fprintf('Reading file %d: %s\n',ix,filename{ix});
    [dose,dose_error,vx,vy,vz] = read_3ddose([pathname,filename{ix}]);

    nx = length(vx)-1;
    ny = length(vy)-1;
    nz = length(vz)-1;

    if (nx ~= nx0) || (ny ~= ny0) || (nz ~= nz0)
        disp('the 3ddose file size does not match ...\n');
        break;
    end

    doseSum = doseSum + dose;
    doseSumError = doseSumError + dose_error;
    ix = ix + 1;
end

%outfile = './IMRT_PMMA266cm7ThlayerCombined.3ddose';
outfile = './HeadFirstFieldCombinedPWater.3ddose';
write_3ddose(outfile,dose,dose_error,vx,vy,vz);
=================================================================
function write_3ddose(filename,dose,dose_error,vx,vy,vz)
fid=fopen(filename,'w');
dim=size(dose);
fprintf(fid,'%d %d %d\n',dim);
fprintf(fid,'%0.5f %0.5f %0.5f %0.5f %0.5f\n',vx);
fprintf(fid,'\n');
fprintf(fid,'%f %f %0.5f %0.5f %0.5f\n',vy);
fprintf(fid,'\n');
fprintf(fid,'%f %f %f %f %f\n',vz);
fprintf(fid,'\n');
for i=1:dim(3)
    fprintf(fid,'%1.15E %1.15E %1.15E\n',dose(:,:,i));
end
fprintf(fid,'\n');
for i=1:dim(3)
    fprintf(fid,'%1.15E %1.15E %1.15E\n',dose_error(:,:,i));
end
fclose(fid);
=================================================================
```

APPENDIX 3

This is a matlab code to read the egsphant file and return the x-z slice that contains the Gadox layer where the image is collected.

```
function [images,slicenums] =
GetSlices(fileNameEGS,fileName3ddose,material)

% READEGSPHANT returns the x-z slices that contain the given material
str = '123456789'
fid = fopen(fileNameEGS,'r');
numMaterials = fscanf(fid,'%d',[1,1]);
```

```
MaterialNames = cell(9,1);
for i=1:numMaterials
    MaterialNames(i) = textscan(fid,'%s',[1]);
end
for i=1:numMaterials
MaterialNames{i}
end


fscanf(fid,'%f',[numMaterials]);
xyzdims = fscanf(fid,'%d',[3]);
xCoords = fscanf(fid,'%f',[xyzdims(1)+1]);
yCoords = fscanf(fid,'%f',[xyzdims(2)+1]);
zCoords = fscanf(fid,'%f',[xyzdims(3)+1]);
data = fscanf(fid,'%c',[xyzdims(1),xyzdims(3)]);
fclose(fid);
i=1;
while(~strcmp(material,MaterialNames{i}))
    i=i+1;
end

s = data(1,:);
slices = find(s==str(i));
fid = fopen(fileName3ddose,'r');
XYZdims = fscanf(fid,'%d',3)
Xcoords = fscanf(fid,'%f',XYZdims(1)+1);
Ycoords = fscanf(fid,'%f',XYZdims(2)+1);
Zcoords = fscanf(fid,'%f',XYZdims(3)+1);
Vol = zeros(XYZdims(1),XYZdims(2),XYZdims(3));
for i=1:XYZdims(3)
    Vol(:,:,i) = fscanf(fid,'%g',[XYZdims(1),XYZdims(2)]);
end
fclose(fid);

images = zeros(XYZdims(1),XYZdims(3),length(slices));
slicenums = slices;
for k=1:length(slices)
    for i=1:XYZdims(1)
        for j=1:XYZdims(3)
            images(i,j,k) = Vol(i,slices(k),j);
        end
    end
end
```

APPENDIX 4

This is a matlab code was written to perform the calibration of the measured IMRT EPID images of the IMRT field, using the division method. This code first reads the dark field image, then reads the IMRT measured image of the phantom, averages this framed image and subtracts the dark field from it. The same procedure is done for MRT field calibration image of the calibration phantom. Finally it performs the calibration using the division method by dividing the IMRT phantom image by the IMRT calibration phantom image.

Appendices

```matlab
function image = plasticcorrect()

    phantomimage = darkcorrect();
     %figure;
    imshow(phantomimage,[]);
    title('Phantom Measured');
    plasticimage = darkcorrect();
    %plasticimage = imrotate(plasticimage,-75);
   % figure;
    imshow(plasticimage,[]);
    title('plastic water phantom');


    cal_image = double(phantomimage)./double(plasticimage);

    calmin =  min(cal_image(:))
    calmax = max(cal_image(:))
    cal_norm = (cal_image - calmin)/(calmax - calmin);

    image = cal_norm; %uint8(floor(cal_norm*255));
    image = imresize(image,[256 256]);
    [name,path] = uiputfile();
if name ~= 0
    imwrite(cal_norm,[path,'/',name])
end
   % imshow(image,[]);
    imtool(image,[]);
    %figure; imshow(image,[]);
    title('measured Calibrated Plastic water');
   % improfile;



================================================
function [image,dark] = readhis()
% IMAGE = READHIS(FILENAME,DC,DARKFILENAME) reads a .his data file,
performs
% dark current correction is DC is set to 1.
%
% AUTHOR: David Warne (david.warne@qut.edu.au), Mohd Al-roumi,
% (m.al-roumi@student.qut.edu.au)
% HPC & Research Support Group (Queensland University of Technology)
% Queensland University of Technology
% Based on IDL code written by Andrew Fielding (QUT)

% Read His file
[filename,hpath] = uigetfile();
% Read dark file
[darkfilename,dpath] = uigetfile();
machineformat = 'native';
header = uint8(zeros(100,1));
frame = uint16(zeros(1024,1024));
fsum = int32(zeros(1024,1024));

% Do dark correction always
dc = 1;
```

```
% read dark file if dark current correction is required
if dc == 1
    dark = readdarkhis([dpath darkfilename]);
else
    dark = int32(zeros(1024,1024));
end


%open file for reading
fid = fopen([hpath filename],'r',machineformat);
% read the header
header = fread(fid,100,'*uint8',0,machineformat);
iframe = 0;
while ~feof(fid)
    frame = fread(fid,[1024,1024],'*uint16',0,machineformat);
    if ~isempty(frame)
        fsum = fsum + int32(frame);
        iframe = iframe + 1;
    end
end
fclose(fid);


% frame average
fsum = fsum/iframe;
%subtract frame averaged offset image
fsum = fsum - dark;
% Unaverage by multiplying by number of frames
fsum = fsum*iframe;


%image = fsum;
image = imresize(fsum,[256 256]);
%imtool(image,[]);
imshow(image,[]);
title('PW phantom');
%imwrite(image,'PHANTOMMEASURED.PNG');


function dark = readdarkhis(filename)
% IMAGE = READDARKHIS(FILENAME) reads a .his dark file
%
% AUTHOR: David Warne (david.warne@qut.edu.au)
%   HPC & Research Support Group (Queensland University of Technology)
%
% Based on IDL code written by Andrew Fielding (QUT)

machineformat = 'native';
header = uint8(zeros(100,1));
frame = uint16(zeros(1024,1024));
fsum = int32(zeros(1024,1024));
fid = fopen(filename,'r',machineformat);
% read the header
header = fread(fid,100,'*uint8',0,machineformat);
iframe = 0;
while ~feof(fid)
    frame = fread(fid,[1024,1024],'*uint16',0,machineformat);
    if ~isempty(frame)
        iframe = iframe + 1;
        fsum = fsum + int32(frame);
    end
end
fclose(fid);
```

```
% frame average
fsum = fsum/iframe;
dark = fsum;
```

```
function [image,dark] = darkcorrect()
% IMAGE = READHIS(FILENAME,DC,DARKFILENAME) reads a .his data file,
performs
% dark current correction is DC is set to 1.
%
% Read His file
[filename,hpath] = uigetfile();
% Read dark file
[darkfilename,dpath] = uigetfile();
machineformat = 'native';
header = uint8(zeros(100,1));
frame = uint16(zeros(1024,1024));
fsum = int32(zeros(1024,1024));

% Do dark correction always
dc = 1;

% read dark file if dark current correction is required
if dc == 1
    dark = readdarkhis([dpath darkfilename]);
else
    dark = int32(zeros(1024,1024));
end

%open file for reading
fid = fopen([hpath filename],'r',machineformat);
% read the header
header = fread(fid,100,'*uint8',0,machineformat);

iframe = 0;
while ~feof(fid)
    frame = fread(fid,[1024,1024],'*uint16',0,machineformat);
    if ~isempty(frame)
        fsum = fsum + int32(frame);
        iframe = iframe + 1;
    end
end
fclose(fid);
% frame average
fsum = fsum/iframe;
%subtract frame averaged offset image
fsum = fsum - dark;
% Unaverage by multiplying by number of frames
%fsum = fsum*iframe;

%image = fsum;

image = imresize(fsum,[256 256]);
%image = imrotate(image,180);
figure, imshow(image,[]);
title('measured phantom');

function dark = readdarkhis(filename)
```

```
machineformat = 'native';
header = uint8(zeros(100,1));
frame = uint16(zeros(1024,1024));
fsum = int32(zeros(1024,1024));
fid = fopen(filename,'r',machineformat);
% read the header
header = fread(fid,100,'*uint8',0,machineformat);
iframe = 0;
while ~feof(fid)
    frame = fread(fid,[1024,1024],'*uint16',0,machineformat);
    if ~isempty(frame)
        iframe = iframe + 1;
        fsum = fsum + int32(frame);
    end
end
fclose(fid);
% frame average
fsum = fsum/iframe;
dark = fsum;
```

APPENDIX 5

This is a matlab code written to perform the calibration of the simulated IMRT EPID images obtained from the 3ddose files, using the division method. It reads the 3ddose file of the phantom (head, pelvic) then reads the 3ddose file of the calibration phantom and finally performs the calibration using the division methods.

```
======================================================================
close all

% AUTHOR: David Warne, mohd Al-roumi
% EMAIL: david.warne@qut.edu.au, m.al-roumi@student.qut.edu.au

[filename,pathname] = uigetfile({'*.3ddose'});
[dose,dose_error,vx,vy,vz] = read_3ddose([pathname,filename]);
nx = length(vx)-1;
ny = length(vy)-1;
nz = length(vz)-1;
%*******************************************************
%slice = 12;      %for PMMA 26.6 layer for FRANK division
 slice = 236;     % Frank phantom first experiment.

%slice = 396;      % for pelvic_phantom 1st beam filled Tissue.
%slice = 433;      % for Pelvic_phantom 2nd beam filled Tissue.
%slice = 381;      % for Pelvic_phantom 3rd beamfilled tissue.
%slice = 434;      % for pelvic_phantom 4th beamfilled Tissue.
%slice = 398;      % for Pelvic_phantom 5th beam filled Tissue.

%slice = 440;      % for Head_phantom 01 Beam filled Tissue.
%slice = 410;      % for Head_phantom 02 Beam filled Tissue.
%slice = 441;      % for Head_phantom 03 Beam filled Tissue.
%slice = 410;      % for Head_phantom 04 Beam filled Tissue.
%slice = 454;      % for Head_phantom 05 Beam filled Tissue.
```

Appendices

```matlab
%slice = 425;      % for Head_phantom 06 Beam filled Tissue.
%slice = 448;      % for Head_phantom 07 Beam filled Tissue.



%im_xy = dose(:,:,slice);
%error_xy = dose_error(:,:,slice);

%figure;
%im_xy = imrotate(im_xy,-90);
%imshow(im_xy',[]);
%title('PMMA combined 7th layer 26.6cm')

%figure;
%plot(im_xy(:,floor(ny/2)));
%title('X Profile PMMA');

%figure;
%plot(im_xy(floor(nx/2),:));
%title('Y Profile PMMA');

%result = mean(im_xy(125:135,125:135));
%result1 = std(im_xy(125:135,125:135));
%*****************************************

im_xzTissue = reshape(dose(:,slice,:),nx,nz);
im_xzTissue = im_xzTissue(:,end:-1:1);
error_xzTissue = reshape(dose_error(:,slice,:),nx,nz);
[name,path] = uiputfile();
if name ~= 0
    imwrite(im_xzTissue,[path,'/',name])
end
figure;
%rotate(im_xzTissue,-90);
imshow(im_xzTissue,[]);
title('Pelvic Filled Tissue');
figure;
plot(im_xzTissue(:,floor(nz/2)));
title('x profiles Tissue');
figure;
plot(im_xzTissue(floor(nx/2),:));
title('z Profiles Tissue');
result = mean(im_xzTissue(125:135,125:135));
result1 = std(im_xzTissue(125:135,125:135));
%****************************************************
fprintf('mean\n');
fprintf('======\n');
fprintf('%f\n',result);
fprintf('STD\n');
fprintf('======\n');
fprintf('%f\n',result1);
fprintf('Done\n');
[filename,pathname] = uigetfile({'*.3ddose'});
[dose,dose_error,vx,vy,vz] = read_3ddose([pathname,filename]);
nx = length(vx)-1;
ny = length(vy)-1;
nz = length(vz)-1;
slice = 236;        % FRANK Phantom first experiment.
```

```matlab
%slice = 434;      % for pelvic_phantom 4th beam.
%slice = 381;      % for Pelvic_phantom 3rd beam
%slice = 398;      % for Pelvic_phantom 5th beam
%slice = 396;      %for Pelvic_phantom 1st beam.
%slice = 433;      % for Pelvic_phantom 2nd beam

%slice = 440;      % for Head_phantom 01 beam.
%slice = 410;      % for Head_phantom 02 beam.
%slice = 441;      % for Head_phantom 03 beam.
%slice = 410;      % for Head_phantom 04 beam.
%slice = 454;      % for Head_phantom 05 beam.
%slice = 425;      % for Head_phantom 06 beam.
%slice = 448;      % for Head_phantom 07 beam.

im_xz = reshape(dose(:,slice,:),nx,nz);
im_xz = im_xz(:,end:-1:1);
error_xz = reshape(dose_error(:,slice,:),nx,nz);
figure;
%imrotate(im_xz',-90);
imshow(im_xz,[]);
title('Frank Simulated');
figure;
plot(im_xz(:,floor(nz/2)));
title('X Profile Frank');
figure;
plot(im_xz(floor(nx/2),:));
title('Z Profile Frank');
result = mean(im_xz(125:135,125:135));
result1 = std(im_xz(125:135,125:135));
fprintf('mean\n');
fprintf('======\n');
fprintf('%f\n',result);
fprintf('STD\n');
fprintf('======\n');
fprintf('%f\n',result1);
fprintf('Done\n');

%calibrated = im_xz ./ im_xy      %for FRANK division.

calibrated = im_xz ./ im_xzTissue
calibrated = imresize(calibrated,[256 256]);
%calibrated = imrotate(calibrated,90);
calmin =  min(calibrated(:))
calmax = max(calibrated(:))
cal_norm = (calibrated - calmin)/(calmax - calmin);
cal_image = uint8(floor(cal_norm*255));
[name,path] = uiputfile();
if name ~= 0
    imwrite(cal_image,[path,'/',name])
end
%imwrite(calibrated 'Head04.png')
figure;
imshow(cal_image);
title('calibrated image');

figure;
%plot(im_xy(:,floor(ny/2)));
plot(calibrated(:,floor(nz/2)));
title('X Profile calibrated');
```

```
imfilter(calibrated,[]);
imtool(calibrated,[]);
imshow(calibrated,[]);
title('filtered')
%imsave('filtered','.jpg');
figure;
%plot(im_xy(floor(nx/2),:));
plot(calibrated(floor(nx/2),:));
title('Y Profile calibrated');
result = mean(calibrated(125:135,125:135));
result1 = std(calibrated(125:135,125:135));
fprintf('mean\n');
fprintf('======\n');
fprintf('%f\n',result);
fprintf('STD\n');
fprintf('======\n');
fprintf('%f\n',result1);
fprintf('Done\n');
```

APPENDIX 6

This matlab code is used to modify the egsphant file resulting from the CTCombine code. This code reads the egsphant file with the EPID attached and replaces the non-air voxels with tissue excluding the EPID. Finally it writes the new modified egsphant file. This new egsphant file was used in the calibration phantom simulation.

==

```
function [egsphantData] =  readEGSPHANT(filename)
% EGSPHANTDATA = READEGSPHANT(FILENAME) reads a .egsphant file
%
% AUTHOR: David Warne, mohd Al-roumi
% EMAIL: david.warne@qut.edu.au, m.al-roumi@student.qut.edu.au
% DEPARTMENT: HPC & Research Support, Queensland University of Technology

% open the file for reading and test a valid handle was returned
fid = fopen(filename,'r');
if fid < 0
    error('ERROR: could not open file, might be invalid name.');
end

% read number of materials
numMaterials = fscanf(fid,'%d',[1 1]);

% read the material names
materialNames = cell(numMaterials,1);
for i=1:numMaterials
    materialNames(i) = textscan(fid,'%s',[1]);
end

% read the estepe
estepe = fscanf(fid,'%f',[numMaterials]);

% read volume dimensions
```

```
xdim = fscanf(fid,'%d',[1]);
ydim = fscanf(fid,'%d',[1]);
zdim = fscanf(fid,'%d',[1]);

% read coordinates
xCoords = fscanf(fid,'%f',[xdim+1]);
yCoords = fscanf(fid,'%f',[ydim+1]);
zCoords = fscanf(fid,'%f',[zdim+1]);
fscanf(fid,'\n');
% read material volume
matVolume = zeros(xdim,ydim,zdim);
for i=1:zdim
    for j=1:ydim
        slice = fscanf(fid,'%c',[xdim]);
        matVolume(:,j,i) = slice;
        fscanf(fid,'\n');
    end
    %matVolume(1:xdim,1:zdim,i) = slice(1:xdim,1:zdim);
end

% read density volume
densityVolume = zeros(xdim,zdim,ydim);
for i=1:zdim
    for j=1:ydim
        slice = fscanf(fid,'%f',[xdim]);
        densityVolume(:,j,i) = slice;
    end
    %densityVolume(1:xdim,1:zdim,i) = slice(1:xdim,1:zdim);
end

% close the file
fclose(fid);

% store results in a struct
egsphantData.numMaterials = numMaterials;
egsphantData.materialNames = materialNames;
egsphantData.estepe = estepe;
egsphantData.xdim = xdim;
egsphantData.ydim = ydim;
egsphantData.zdim = zdim;
egsphantData.xCoords = xCoords;
egsphantData.yCoords = yCoords;
egsphantData.zCoords = zCoords;
egsphantData.matVolume = matVolume;
egsphantData.densityVolume = densityVolume;
```

```
% copy old data to new location
egsNew = egsOld;
AirSymbol = 49;
% find the epid surface
i = 0;
while egsOld.matVolume(1,i+1,1) == '1'
    i = i + 1;
end

phant_end = i;

% for every slice
```

```
for k=1:egsOld.zdim
    for j=1:phant_end
        % grab the x-row
        row = egsOld.matVolume(:,j,k);
        % get the non-air locations
        I = find(row ~= AirSymbol);
        % update new egsphant
        egsNew.matVolume(I,j,k) = tissueSymbol;
        egsNew.densityVolume(I,j,k) = tissueDensity;
    end
end
```

```
function writeEGSPHANT(filename,egsphantData)
% WRITEEGSPHANT(FILENAME) writes phantom data to a .egsphant file
%
% open the file for writing and test a valid handle was returned
fid = fopen(filename,'w');
if fid < 0
    error('ERROR: could not open file for writing, might be an invalid
name.');
end

%write number of materials
fprintf(fid,' %d\n',egsphantData.numMaterials);

% write material names
for i=1:egsphantData.numMaterials
    str = egsphantData.materialNames{i};
    fprintf(fid,'%s\n',str[136]);
end

% write estepe
for i=1:egsphantData.numMaterials
    fprintf(fid,'%f ',egsphantData.estepe(i));
end
fprintf(fid,'\n');

% write volume dimensions
writeInteger(fid,egsphantData.xdim);
writeInteger(fid,egsphantData.ydim);
writeInteger(fid,egsphantData.zdim);
fprintf(fid,'\n');
% write coordinates
fprintf(fid,'%f %f %f %f %f\n',egsphantData.xCoords);
fprintf(fid,'\n');
fprintf(fid,'%f %f %f %f %f\n',egsphantData.yCoords);
fprintf(fid,'\n');
fprintf(fid,'%f %f %f %f %f\n',egsphantData.zCoords);
fprintf(fid,'\n');

% write material volume
vals = zeros(egsphantData.xdim,1);
for k=1:egsphantData.zdim
    for j=1:egsphantData.ydim
        for i=1:egsphantData.xdim
            vals(i) = egsphantData.matVolume(i,j,k);
        end

        fprintf(fid,'%c',vals);
```

```
            fprintf(fid,'\n');
        end
        fprintf(fid,'\n');
    end
end

% write density volume
for k=1:egsphantData.zdim
    for j=1:egsphantData.ydim
        for i=1:egsphantData.xdim
            vals(i) = egsphantData.densityVolume(i,j,k);
        end
        fprintf(fid,'%f %f %f %f\n',vals);
        fprintf(fid,'\n');
    end
    fprintf(fid,'\n');
end

fclose(fid);

function writeInteger(fid,num)

if num < 10
    fprintf(fid,'     %d',num);
elseif num < 100
    fprintf(fid,'    %d',num);
elseif num < 1000
    fprintf(fid,'   %d',num);
elseif num < 10000
    fprintf(fid,' %d',num);
end
```

```
[file,path] = uigetfile({'*.egsphant','egs phantom files
(*.egsphant)'},'Open input file');
inputfile = [path,'/',file];
 % read the .egsphant file
tic
egs_in = readEGSPHANT(inputfile);
toc
% make the phantom all tissue (51 is the ASCII code for the character 3)
tic
%egs_out = tissueFill(egs_in,51,0.979);
egs_out = tissueFill(egs_in,51,1.053);
toc
% write out the result
[file,path] = uiputfile({'*.egsphant','egs phantom files
(*.egsphant)'},'save output file');
outputfile = [path,'/',file];
tic
writeEGSPHANT(outputfile,egs_out);
toc
```

References

1. Webb, S., *Intensity – modulated radiation therapy*. 1993: Institute of Physics Publishing.

2. Munro, P.a.D.C.B., *X-ray quantum limited portal imaging using amorphous silicon flat-panel arrays*. Med. Phys, 1998. **25**(5): p. 0094-2405.

3. Fielding, A.L., Philip M. Evansa, and Catharine H. Clark, *Verification of patient position and delivery of IMRT by electronicportal imaging*. Radiotherapy and Oncology, 2004. **73**(3): p. 339-347.

4. Fielding, A., Philip M. Evans, and Cathrine H. Clark,, *The use of electronic portal imaging to verify patient position during intensity-modulated radiotherapy delivered by the dynamic MLC technique*. International Journal of Radiation Oncology*Biology*Physics, 2002. **54**(4): p. 1225-1234.

5. Kawrakow, I.a.D.W.O.R., *EGSnrcMP: the multi-platform environment for EGSnrc*. 2006, NRCC Report PIRS-877X.

6. Rogers, D.W.O., Walters B.,and Kawrakow I., *BEAMnrc Users Manual*, in *NRCC Report PIRS-0509(A)revK*. 2007, Ionizing Radiation Standards National Research Council of Canada, Ottawa, K1A OR6.

7. Walters, B., I. Kawrakow., and D.W.O. Rogers, *DOSXYZnrc Users Manual*, in *NRCC Report PIRS-794revB*. 2011, Ionizing Radiation Standards National Research Council of Canada, Ottawa K1A 0R6.

8. Morton, E.J., Swindell, W., Lewis DG., and Evans PM., *A linear array, scintillation crystal-photodiode detector for megavoltage imaging.* Medical Physics, 1991. **18**(4): p. 681-691.

9. National Institutes of Health (NHI). *Fact Sheet*. 2011.

10. Patel, J.K., M. S. Didolkar., J. W. Pickren., and R. H. Moore, *Metastatic pattern of malignant melanoma: A study of 216 autopsy cases.* The American Journal of Surgery, 1978. **135**(6): p. 807-810.

11. Talmadge, J.E., and I. J. Fidler, *AACR centennial series: The biology of cancer metastasis: Historical perspective.* Cancer Research, 2010. **70**(14): p. 5649-5669.

12. report, C.C.A., *Cancer Council Australia report*. 2009.

13. AIHW, C.C.A.A.A.A.o.C.R., *Cancer survival and prevalence in Australia: cancers diagnosed from 1982 to 2004*, in *Cancer Series*. 2008, AIHW, CA (Cancer Australia) & AACR (Australasian Association of Cancer Registries): Canberra.

14. (AIHW), A.I.o.H.a.W., *ACIM (Australian Cancer Incidence and Mortality) Books*. 2011.

15. (AIHW), A.I.o.H.a.W., *Cancer incidence projections: Australia, 2011 to 2020*, in *Cancer Series*, AIHW, Editor. 2012, AIHW: Canberra.

16. *Non-melanoma skin cancer: general practice consultations, hospitalisation and mortality*, in *Australian Institute of Health and Welfare & Cancer Australia (AIHW & CA) Cancer Series*. 2008: Canberra.

17. Webb, S., *The physics of three-dimensional radiation therapy, conformal radiotherapy radio surgery a treatment planning*. 1993: IOP Publishing Ltd.

18. Webb, S., *The physics of conformal radiotherapy.* 1997: Bisrol; IOPP.

References

19. Webb, S., Ph.D. , *Intensity-modulated radiation therapy*. Series in Medical Physics. 2001: Bristol: Institute of Physics Pub.

20. Khan, F.M., *The physics of radiation therapy*. 2010: Philadelphia, Pa: Lippincott Williams & Wilkins.

21. Murat Beyzadeoglu, Gokhan Ozyigit, and C. Ebruli, *Basic Radiation Oncology*. 2010.

22. Podgorsak, E.B., *Radiation oncology physics: a handbook for teachers and students*. 2005: International Atomic Energy Agency, Vienna.

23. Cherry, P., and Duxbury, Angela. , *Practical radiotherapy physics and equipment*. 2nd ed. 2009: Blackwell Publishing Ltd.

24. Fasso A., K.G., M. Höfert., J. Ranft., and G. Stevenson, *Shielding against high energy radiation*. 2006: Springer, Berlin.

25. Michael G. Herman , J.M.B., David A. Jaffray, Kiarin P. McGee, Peter Munro, Shlomo Shalev, Marcel Van Herk, John W. Wong, *Clinical use of electronic portal imaging*, in *Report of AAPM radiation Therapy committee task group 58*. 2001: .

26. Bethesda, M., *Determination of absorbed dose in a patient irradiated by beams of X-ray or Gamma Rays in radiotherapy procedures.* ICRU Report No. 24 ICRU, , 1976.

27. Thwaites, D.J., B. J. Mijnheer, and J. A. Mills, *Optically Stimulated Luminescence: Fundamentals and Applications*. 2005.

28. (IAEA), I.a.e.a., *Transition from 2-D radiotherapy to 3-D conformal and intensity modulated radiotherapy*, in *International atomic energy agency (IAEA)*, IAEA, Editor. 2008: IAEA, VIENNA, Austria.

29. M. Kara Bucci, M.A.B., MD, PhD; Mack Roach III, MD, *Advances in radiation therapy: conventional to 3D, to IMRT, to 4D, and beyond.* Cancer J Clin © American Cancer Society, Inc., 2005. **55**: p. 117–134.

30. Varadharajan, E., and Velayudham Ramasubramanian, *Analysis of low dose level volumes in intensity modulated radiotherapy and 3-D conformal radiotherapy.* Department of Radiation Oncology, Billroth Hospitals LTD, Chennai, India. Nuclear and Medical Physics Division, VIT University, Vellore, India. International Journal of Cancer Therapy and Oncology., 2014.

31. Webb, S., *Contemporay IMRT developing physics and clinical Implementation.* 2005: IOP Publishing Ltd.

32. Bin S. Teh., S.Y.W.a.E.B.B., *Intensity Modulated Radiation Therapy (IMRT): A new promising technology in radiation oncology.* The Oncologist,, 1999. **4**(Department of Radiology/Radiation Oncology, Baylor College of Medicine, Houston, Texas USA.): p. 433-442.

33. Bortfeld, T., Arthur L. Boyer., Darren L. Kahler., Timothy J. Waldron. , *Realization and verification of three-dimensional conformal radiotherapy with modulated fields.* International Journal of Radiation Oncology*Biology*Physics, 1994. **30**(4): p. 899-908.

34. Hellman, S., *A practical guide to intensity – modulated radiation therapy*. Medical Physics Publishing. 2003.

35. Bethesda, *International commissioning on radiation units, ICRU report 50 : prescribing, recording and reporting photon beam therapy*. 1993.

36. Bethesda, *International Commission on Radiation Units and Measurements : Prescribing, Recording, and Reporting Photon Beam Therapy Report 62 (Supplement to ICRU Report 50)* International Commission on Radiation Units and Measurements, 1999.

References

37.   Zizzari, A., *Automatic definition of planning target volume in computer-assisted radiotherapy.* Department of Cybernetics, School of Systems Engineering. The University of Reading, Whiteknights, PO Box 255. Reading, RG6 6AY, England.

38.   Barrett, A., Jane Dobbs., Stephen Morris., and Tom Roques., *Practical radiotherapy planning*. 4th. ed. 2009: Hodder Arnold, .

39.   Ann Barrett, et al., *Practical Radiotherapy Planning*. 4th. ed. 2009: Hodder Arnold, .

40.   Grégoire, V., E. Coche., G. Cosnard., M. Hamoir., and H. Reychler. , *Selection and delineation of lymph node target volumes in head and neck conformal radiotherapy. Proposal for standardizing terminology and procedure based on the surgical experience.* Radiotherapy and Oncology, 2000. **56**(2): p. 135-50.

41.   Taylor A., A.G.R., R. H. Reznek., and M. E. Powell *Mapping pelvic lymph nodes: guidelines for delineation in intensity-modulated radiotherapy.* Int. J. Radiation Oncology Biol. Phys.,, 2005. **63**(5): p. 1604-12.

42.   measurements, I.c.o.r.u.a., *Measurement of absorbed dose measured in a phantom irradiated by a single beam of X or gamma rays*, in
1973, Bethesda: Maryland, U.S.A.

43.   Benedick Fraass, M.H., Gerald Kutcher, George Starkschall, Robin Stern, and Jake Van Dyke, *Quality assurance for clinical radiotherapy treatment planning.* Medical Physics, 1998. **25**(10): p. 1773-1829.

44.   Bruinvis, I.A.D., et al., *Quality assurance of 3-D treatment planning systems for external photon and electron beams*, in *Practical guidelines for initial verification and periodic quality control of radiation therapy treatment planning systems*, N.C.o.R.D.S.T.P. Systems, Editor. 2005, Netherlands Commission on Radiation Dosimetry.

45.   Stroom, J.C., et al., *Inclusion of geometrical uncertainties in radiotherapy treatment planning by means of coverage probability.* International Journal of Radiation Oncology*Biology*Physics, 1999. **43**(4): p. 905-919.

46.   Alber, M., Sara Broggi., Carlos De Wagter., Ines Eichwurzel., Per Engström., Claudio Fiorino., Dietmar Georg., Günther Hartmann., et al. , *Guidelines for the verification of IMRT*. 1st ed. 2008: ESTRO Mounierlaan 83/12 − 1200 Brussels (Belgium).

47.   Brahme, A., *Optimization of stationary and moving beam radiation therapy techniques.* Radiotherapy and Oncology, 1988. **12**(2): p. 129-140.

48.   Brahme, A., *Optimized radiation therapy based on radiobiological objectives.* Seminars in Radiation Oncology, 1999. **9**(1): p. 35-47.

49.   Bortfeld, T., *Optimized planning using physical objectives and constraints.* Seminars in Radiation Oncology, 1999. **9**(1): p. 20-34.

50.   Ezzell, G.A., et al., *Guidance document on delivery, treatment planning, and clinical implementation of IMRT: Report of the IMRT subcommittee of the AAPM radiation therapy committee*. 2003, American Association of Physics and Medicine (AAPM). p. 2089-2115.

51.   Hellman, S., *A practical guide to intensity-modulated radiation therapy*. 2003: Madison, Wis: Medical Physics.

52.   Kazuo Hatano, H.A., Mitsuhiro Sakai,, N.T. Takashi Kodama, Tohru Kawachi,, and e.a. Masaharu Imazeki, *Current status of intensity-modulated radiation therapy (IMRT).* The Japan Society of Clinical Oncology, 2007. **12**(DOI 10.1007/s10147-007-0703-9): p. 408–415.

53.   Boyer, L., Ph.D., Butler, E., Brian M.D., DiPetrillo, Thomas A. M.D., Mark J. Engler, Ph.D., Benedick Fraass, Ph.D., Walter Grant, III, Ph.D., C. Clifton Ling, Ph.D., Daniel A. Low, Ph.D., et al., *Intensity-modulated radiotherapy : current*

status and issues of interest. International Journal of Radiation Oncology, Biology, Physics, 2001. **51**(4): p. 880-914.

54.   Gerald J. Kutcher, T.C., et al., *Comprehansive QA for radiation oncology, AAPM report No.46, Task group No. 40.* 1994, American Institute of Physics: USA.

55.   Maria M. Aspradakis, P.D., MIPEM, , Geoff D. Lambert, M.S. (FIPEM), and Alasdair Steele, M.S., IIPEM, *Elements of commissioning step-and-shoot IMRT: Delivery equipment and planning system issues posed by small segment dimensions and small monitor units.* Medical Dosimetry, 2005. **30**(4): p. 233-242.

56.   Mijnheer, G., *Guidelines for the verification of IMRT* ESTRO, 2008.

57.   Webb, S., *Contemporary IMRT developing physics and clinical implementation.* 2005: IOP Publishing Ltd.

58.   Wolff, D., F. Stieler., B. Hermann., et al. , *Clinical implementation of volumetric intensity-modulated arc therapy (VMAT) with ERGO++* Strahlenther Onkol. , 2010. **186**: p. 280-288.

59.   Stieler F, W.D., Schmid H, et al. , *A comparison of several modulated radiotherapy techniques for head and neck cancer and dosimetric validation of VMAT. .* Radiother Oncol. , 2011. **101**: p. 388-393.

60.   Otto, K., *Volumetric modulated arc therapy: IMRT in a single gantry arc. .* Medical Physics, 2007. **35**: p. 310-317.

61.   Gevaert T., B.E., C. Garibaldi., et al. , *Implementation of HybridArc treatment technique in preoperative radiotherapy of rectal cancer: Dose patterns in target lesions and organs at risk as compared to helical tomotherapy and RapidArc. .* Rad Oncol, 2012. **7**(120).

62.   Khan, F.M., *Treatment planning in radiation oncology.* 2nd ed ed. 2007: Philadelphia: Lippincott Williams & Wilkins.

63. The royal college of radiation, s.a.c.o.r., institute of physics and engineering in medicine. National patient agency, British Institute of radiology., *On target: ensuring geometric accuracy in radiotherapy.* , 2008.

64. Wambersie, A., and Torsten Landberg., *Report 62: Prescribing, recording and reporting photon beam therapy (supplement to ICRU report50), 1999.*

.

65. van Herk, M., P. Remeijer, and J.V. Lebesque, *Inclusion of geometric uncertainties in treatment plan evaluation.* International Journal of Radiation Oncology*Biology*Physics, 2002. **52**(5): p. 1407-1422.

66. Steenbakkers, R.J.H.M., *Optimizing target definition for radiotherapy*. 2007, University of Amsterdam (UvA): Amsterdam.

67. van Herk, M., et al., *The probability of correct target dosage: dose-population histograms for deriving treatment margins in radiotherapy.* International Journal of Radiation Oncology*Biology*Physics, 2000. **47**(4): p. 1121-1135.

68. de Boer, H.C.J., et al., *Electronic portal image assisted reduction of systematic set-up errors in head and neck irradiation.* Radiotherapy and Oncology, 2001. **61**(3): p. 299-308.

69. de Boer, H.C.J. and B.J.M. Heijmen, *A protocol for the reduction of systematic patient setup errors with minimal portal imaging workload.* International Journal of Radiation Oncology*Biology*Physics, 2001. **50**(5): p. 1350-1365.

70. Bel, A., et al., *A verification procedure to improve patient set-up accuracy using portal images.* Radiotherapy and Oncology. **29**(2): p. 253-260.

71. Langmack, K.A., *Portal imaging.* The British Journal of Radiology, 2001. **74**(885): p. 789-804.

References

72.   Burnet, N.G., et al., *A tool to measure radiotherapy complexity and workload: derivation from the basic treatment equivalent (BTE) concept.* Clin Oncol (R Coll Radiol), 2001. **13**(1): p. 14-23.

73.   Ludbrook, J.J.S., et al., *Correction of systematic setup errors in prostate radiation therapy: How many images to perform?* Medical Dosimetry. **30**(2): p. 76-84.

74.   Margie A. Hunt., M.A., Gerald J Kutcher., Chandra Burman., Daniel Fass., Louis Harrison., Steven Leibel., Zvi Fuks, MD. , *The effecct of setup uncertanties on the treatment of nasopharynx cancer.* Int. J. Radiation Oncology Biol. Phys.,, 1993. **27**: p. 437-447.

75.   Kwok Leung Lam, et al., *Automated determination of patient setup errors in radiation therapy using spherical radio-opaque markrs.* Med. Phys, 1993. **20**(4).

76.   Marcel Van Herk, P.D., et al., *Quantification of organ motion during conformal radiotherapy of the prostate by three dimensional image registration.* Int. J. Radiation Oncology Biol. Phys.,, 1995. **33**(5): p. 1311-1320.

77.   Meijer, G.J., and Coen Rasch., Peter Remeijer., Joos V. Lebesque, *Three-dimensional analysis of delineation errors, setup errors, and organ motion during radiotherapy of bladder cancer.* International Journal of Radiation Oncology*Biology*Physics, 2003. **55**(5): p. 1277-1287.

78.   Venselaar, J., Hans Welleweerd., and Ben Mijnheer, *Tolerances for the accuracy of photon beam dose calculations of treatment planning systems.* Radiotherapy and Oncology, 2001. **60**(2): p. 191-201.

79.   Mijnheer, B.J., J.J. Batterman., and A. Wambersie., *What degree of accuracy is required and can be achieved in photon and neutron therapy?* Radiotherapy and Oncology, 1987. **8**(3): p. 237-252.

80.   Van Herk, M., *Different styles of image-guided radiotherapy.* Semin Radiat Oncol 2007. **17**(25): p. 67.

81. De Los Santos, J., et al., *Image Guided Radiation Therapy (IGRT) Technologies for Radiation Therapy Localization and Delivery.* International Journal of Radiation Oncology*Biology*Physics, 2013. **87**(1): p. 33-45.

82. James Balter, et al., *The role of in-room kV X-ray imaging for patient setup and target localization, AAPM task group 104*. 2009, American Association of Physicists in Medicine. .

83. Dawson, L.A., and D. A. Jaffray *Advances in image-guided radiation therapy. .* Clinical Oncology, 2007. **25**: p. 938-46.

84. Gupta, T., and C Anand Narayan, *Image-guided radiation therapy: Physician's perspectives.* Medical Physics 2012. **Oct-Dec 37**(4): p. 174-182.

85. Antonuk, L.E., *Electronic portal imaging devices: a review and historical perspective of contemporary technologies and research.* phys. Med. Biol, 2001. **Vol. 47 92002 R31-R65.**

86. K A Langmack, D., *Portal imaging.* British Journal of Radiology 2001. **74**: p. 789-804.

87. Nzhde Agazaryan, K.M.F., Joerg Lehmann, *Image guided radiation therapy (IGRT) technologies for radiation therapy localization and delivery.* International Journal of Radiation Oncology Biology Physics, 2013. **87, No.1**(0360-3016/S): p. 33-45.

88. Langmack, K.A., *Portal imaging.* British Journal of Radiology 2001. **74**: p. 789-804.

89. Winkler Peter, A.H., and Dietmar Georg, *Dose-response characteristics of an amorphous silicon EPID.* Medical Physics, 2005. **32**(10): p. 0094-2405/2005/32,,10…/3095/11.

References

90.   McDermott, L.N., R. J. W. Louwe, J.J. Sonke, M. B. van Herk, and B. J. Mijnheer, *Dose–response and ghosting effects of an amorphous silicon electronic portal imaging device.* Med Phys, 2003. **31**(2): p. 0094-2405/2004/31(2)/285/11.

91.   Rogers, D.W.O., *Monte Carlo techniques in radiotherapy.* Physics in Canada, Medical Physics Special Issue, 2002. **58**(2): p. 63-70.

92.   Mesbahi, A., Andrew J. Reilly., and David I. Thwaites, *Development and commissioning of a Monte Carlo photon beam model for Varian Clinac 2100EX linear accelerator.* Applied Radiation and Isotopes, 2006. **64**(6): p. 656-662.

93.   Flampouri, S.P.M.E., F. Verhaegen., A. E. Nahum., E. Spezi., and M Partridge., *Optimization of accelerator target and detector for portal imaging using Monte Carlo simulation and experiment.* IOP Publishing Ltd, 2002. **47**: p. 3331–3349.

94.   Kruse, J.J., Michael G. Herman., Chris R. Hagness., Brian J. Davis., Yolanda I. Garces., Michael G. Haddock., Kenneth R. Oliver., et al. , *Electronic and film portal images : a comparison of landmark visibility and review accuracy.* International Journal of Radiation Oncology*Biology*Physics, 2002. **54**(2): p. 584-591.

95.   Crevoisier R. de D. Kuban, a.D.L., *Image-guided radiotherapy by in-room CT-linear accelerator combination.* Cancer/Radiotherapie, 2006. **10**(5): p. 245-251.

96.   Bissonnette, J.-P., et al., *Quality assurance for image-guided radiation therapy utilizing CT-based technologies: A report of the AAPM TG-179.* Medical Physics, 2012. **39**(4): p. 1946-1963.

97.   Aubin, M., et al., *The use of megavoltage cone-beam CT to complement CT for target definition in pelvic radiotherapy in the presence of hip replacement.* The British Journal of Radiology, 2006. **79**(947): p. 918-921.

98.   Munro, P., et al. *Therapy Imaging: Limitations Of Imaging With High Energy X-Ray Beams*. 1987.

99.   Court, L., et al., *Evaluation of mechanical precision and alignment uncertainties for an integrated CT/LINAC system.* Medical Physics, 2003. **30**(6): p. 1198-1210.

100.   Curtis, W., Y. Slav, and D. Jake Van, *Optimization of megavoltage CT scan registration settings for thoracic cases on helical tomotherapy.* Physics in Medicine and Biology, 2007. **52**(15): p. N345.

101.   Ruchala K. J. G. H. Olivera, E.A.S., and T. R. Mackie,, *Megavoltage CT on a tomotherapy system.* Physics inMedicine and Biology, 1999. **44**(10): p. 2597-2621.

102.   Jaffray, D.A., *Kilovoltage volumetric imaging in the treatment room.* Frontiers of Radiation Therapy and Oncology, , 2007. **40**: p. 116–131.

103.   McBain C. A. A. M. Henry, J.S.e.a., *X-ray volumetric imaging in image-guided radiotherapy: the new standard in ontreatment imaging.* International Journal of Radiation Oncology Biology, Physics, 2006. **64**(2,): p. 625–634.

104.   Morin O., A.G., J. Chen et al., *Megavoltage cone-beamCT: system description and clinical applications.* Medical Dosimetry, 2006. **31**(1): p. 51–61.

105.   Pouliot J. A. Bani-Hashemi, M.S.e.a., *Low-dose megavoltage cone-beam CT for radiation therapy.* International Journal of Radiation Oncology Biology Physics, 2005. **61**(2): p. 552–560.

106.   Adler Jr. J. R.   S. D. Chang, M.J.M., J. Doty, P. Geis, S. L.Hancock, , *The Cyberknife: a frameless robotic system for radiosurgery.* Stereotactic and Functional Neurosurgery, 1997. **69**(1-4): p. 124-128.

107.   Antypas C. and E. Pantelis, P.e.o.a., *Performance evaluation of a CyberKnife G4 image-guided robotic stereotactic radiosurgery system.* Physics in Medicine and Biology, 2008. **53**(17): p. 4697-4718.

108.   Shirato, H.S.S., K. Kitamura et al., ","   vol. 48, no. 2, pp. 435–442, 2000., *Four-dimensional treatment planning and fluoroscopic real-time tumor tracking*

radiotherapy for moving tumor. International Journal of Radiation Oncology, Biology,Physics, 2000. **48**(2): p. 435-442.

109.   Shirato H. , S.S., T. Kunieda et al., *Physical aspects of a real-time tumor-tracking system for gated radiotherapy.* International Journal of Radiation Oncology Biology Physics,, 2000. **48**(4): p. 1187-1195.

110.   Kamino Y. K. Takayama, M.K.e.a., *Development of a four-dimensional image-guided radiotherapy system with a gimbaled X-ray head.* International Journal of Radiation Oncology, Biology, Physics, . **66**(1): p. 271-278.

111.   Chang Z. Z. Wang, Q.J.W.e.a., *Dosimetric characteristics of Novalis Tx system with high definition multileaf collimator.* Medical Physics, 2008. **35**(10).

112.   Jin J.-Y. F.-F. Yin, S.E.T., P. M. Medin, and T. D. Solberg,, *Use of the BrainLAB ExacTrac X-Ray 6D System in Image-Guided Radiotherapy.* Medical Dosimetry,, 2008. **33**(2): p. 124-134.

113.   Fuss, M., et al., *Daily ultrasound-based image-guided targeting for radiotherapy of upper abdominal malignancies.* International Journal of Radiation Oncology • Biology • Physics. **59**(4): p. 1245-1256.

114.   D'Ambrosio, D.J., et al., *Continuous localization technologies for radiotherapy delivery: Report of the American Society for Radiation Oncology Emerging Technology Committee.* Practical Radiation Oncology, 2012. **2**(2): p. 145-150.

115.   Ezz A, e.a., *Daily monitoring and correction of radiation field placement using a video-based portal imaging system.* International Journal of Radiation Oncology Biology, Physics, 1992. **22**: p. 159-165.

116.   Gildersleve J, e.a., *A randomised trial of patient repositioning during radiotherapy using megavoltage imaging system.* Radiotherapy and Oncology,, 1994. **31**: p. 161-168.

117.	Kirby M. C. and P.C. Williams, *The use of an electronic portal imaging device for exit dosimetry and quality control measurements.* International Journal of Radiation Oncology Biology, Physics, 1995. **31**: p. 593-603.

118.	Vieira, S., *Dosimetric verification of intensity modulated radiotherapy with an electronic portal imaging device*, in *Department of Radiation Oncology, Division of Medical Physics, Division of Medical Physics, Erasmus MC/Daniel den Hoed Cancer Center, Rotterdam, The Netherlands.* 2002: Rotterdam.

119.	Chang, J., Gikas S. Mageras., Chen S. Chui., Clifton C. Ling., and Wendell Lutz., *Relative profile and dose verification of intensity-modulated radiation therapy.* International Journal of Radiation Oncology*Biology*Physics, 2000. **47**(1): p. 231-240.

120.	Van Elmpt, W., Leah Dermott., Sabastiaan Nijisten., Markus Wending., Philippe Lambie., and Ben Mijnheer. , *A literature review of electronic portal imaging for radiotherapy dosimetry.* Radiotherapy and Oncology, 2008. **88**(3): p. 289-309.

121.	ICRU Report No. 24 ICRU, B., MD, *Determination of absorbed dose in a patient irradiated by beams of X-ray or Gamma Rays in radiotherapy procedures.* 1976.

122.	Brahme, A., *Accuracy requirements and quality assurance of external beam therapy with photons and electrons*. 1988: Foundation Acta Radiologica.

123.	Łukasz Szczurek, et al., *Evaluation of set-up verification with the analysis of systematic and random errors in radiotherapy – a study of the Great Poland Cancer Centre.* NUKLEONIKA, 2008. **4**(53): p. 167-171.

124.	Mechalakos, J.G., et al., *Measurement of setup deviation in IMRT head and neck patients using an on-board kilovoltage imager*. 2007. Vol. 8. 2007.

125.	Naiyanet, N., et al., *Measurements of patient's setup variation in intensity-modulated radiation therapy of head and neck cancer using electronic portal imaging device.* Biomedical Imaging and Intervention Journal, 2007. **3**(1): p. e30.

References

126. Pehlivan, B., et al., *Interfractional set-up errors evaluation by daily electronic portal imaging of IMRT in head and neck cancer patients.* Acta Oncologica, 2009. **48**(3): p. 440-445.

127. Kang, H., et al., *Accurate positioning for head and neck cancer patients using 2D and 3D image guidance.* 2010. Vol. 12. 2010.

128. Nithya Kanakavelu, J.J.S., *Determination of patient set-up error and optimal treatment margin for intensity modulated radiotherapy using image guidance system.* JBUON, 2016. **2**(21): p. 505-511.

129. Infusino, E., et al., *Estimation of patient setup uncertainty using BrainLAB Exatrac X-Ray 6D system in image-guided radiotherapy.* 2015. Vol. 16. 2015.

130. Zhang, X., et al., *Margin evaluation of translational and rotational set-up errors in intensity modulated radiotherapy for cervical cancer.* SpringerPlus, 2016. **5**(1): p. 1-9.

131. Carrier, J.F., L. Beaulieu., and R. Rooy, *Validtion of GEANT4, an object-orientated Monte Carlo toolkit for simulations in medical physics.* Phys. Med. Biol, 2004. **31**(484-492).

132. Hendricks, J.S., *A monte Carlo code for particle transport.* Los Alamos Scientefic Labaratory Report, 1994.

133. Hartmann Siantar, C.L., W. P. Chandler., J. A. Rathkopf., M. M. Svatos., and R. M. White.,, *Peregrine : an all-particle Monte Carlo code for radiation therapy*, in *International Conference on Mathematics and Computations, Reactor Physics, and Environmental Analyses.* 1994, Lawrence Livermore National Laboratory, University of California, P.O. Box 808, Livermore, California 94550: Portland, Oregon.

134. Nelson, W.R., H Hirayama., and D. W. O. Rogers.,, *The EGS4 code system.* 1985, Stanford Linear Accelerator Centre Report: SLAC-265, Stanford, CA: SLCA.

135. Ford, R.L.a.W.R.N., *The EGS code system : computer programs for the monte carlo simulation of electromagnetic cascade showers (version 3)* 1978, Science Applications, Inc and Stanford Linear Accelerator Centre, SLAC-210, UC-3 (I).

136. Khaled Aljarrah1, G.C.S., Toni Neicu2, and Steve B. Jiang2, *Determination of the initial beam parameters in Monte Carlo linac simulation.* Medical Physics, 2006. **33**(4): p. 9 pages.

137. Kairn T, C.D., Sandford PM, and Fielding AL, *Radiotherapy treatment verification using radiological thickness measured with an amorphous silicon electronic portal imaging device: Monte Carlo simulation and experiment.* Physics in Medicine and Biology, 2008. **53**(14): p. 3903-19.

138. Al-Roumi, M.d., *Prediction of portal dose images using Monte-Carlo techniques*, in *Faculty of Science and Engineering*. 2006, Queensland University of Technology: Brisbane.

139. Aljarrah Khaled., G.C.S., Toni Neicu, and Steve B. Jiang, *Determination of the initial beam parameters in Monte Carlo linac simulation.* Medical Physics, 2006. **33**(4): p. 850-858.

140. Rogers, K.I.a.D.W.O., *Monte Carlo techniques in radiotherapy.* Ionizing Radiation Standards National Research of Canada, Ottawa, 2002. **33**(4): p. 94-2405, 850.

141. Kairn, T., M. Dwyer., D. Warne., T. S. Markwell., J. V. Trapp., and A. L. Fielding, *CT Combine: Rotating and combining CT data with an accurate detector model, to simulate radiotherapy portal imaging at non-zero beam angles*, in *Engineering and Physical Sciences in Medicine and the Australian Biomedical engineering College Conference. Canberra, Australia*. 2009.

142. Morton EJ, S.W., Lewis DG, Evans PM, *A linear array, scintillation crystal-photodiode detector for megavoltage imaging.* Medical Physics, 1991. **18**(4): p. 681-691.

References

143. Kawrakow, I., D.W.O. Rogers, and B.R.B. Walters, *Large efficiency improvements in BEAMnrc using directional bremsstrahlung splitting.* Med. Phys, 2004. **31**(10).

144. Joao Seco, F.V., ed. *Monte Carlo techniques in radiation therapy.* Imaging in medical diagnosis and therapy., ed. F.V. Joao Seco. 2013, CRC/Taylor & Francis.

145. Rogers D.W.O., B.A.F., G. X. Ding, C.-M. Mai, J. We, and T. R. Mackie, *BEAM: A Monte Carlo code to simulate radiotherapy treatment units.* Ionizing Radiation Standards, Institute for National Measurement Standards, National Research Council Canada, Ottawa K1A 0R6, Canada 1995.

146. Daryoush Sheikh-Bagheri, et al., *Monte Carlo Simulations:Efficiency Improvement Techniques and Statistical Considerations*, in *Med. Phys*. 2006. p. 71-91.

147. D.W.O. Rogers, B.W., I. Kawrakow, *BEAMnrc Users Manual*, in *NRCC Report PIRS-0509(A)revK*. 2007, Ionizing Radiation Standards National Research Council of Canada, Ottawa, K1A OR6.

148. Crowe, B.S., *The development of Monte Carlo techniques for the verification of radiotherapy treatments*, in *Faculty of science and technology, Queensland University of Technology*. 2011.

149. Kairn, T., et al., *Contrast enhancement of EPID images via difference imaging: a feasibility study.* Physics in Medicine and Biology, 2010. **55**(22): p. N533.

150. Von Wittenau, A.E.S., Logan, C. M., Aufderheide Iii, M. B., and Slone, D. M., *Blurring artifacts in megavoltage radiography with a flat-panel imaging system: Comparison of Monte Carlo simulations with measurements.* Medical Physics, 2002. **29**(11): p. 2559-2570.

151. Imad Ali, S.A., *Evaluation of the effects of sagging shifts on isocentre accuracy and image quality of cone-beam CT from KV on-board imagers.* Jurnal of applied clinical medical physics, 2009. **10**(3).

152. Weiliang Du, S.G., Xiaochun Wang, and Rajat J. Kudchadker, *Quantifying the gantry sag on linear accelerators and introducing an MLC-based compensation strategy.* Med. Phys., 2012. **39**(4): p. 2156-2162.

153. Siebers, J.V.P.D., Paul J. KEALL, PH.D., W. U. Qiuwen, PH.D., Jeffery F. Willliamson, PH.D. and Rupert K. Schmidt-Ullrich, M.D., *Effect of patient setup errors on simulanteously integrated boost head and neck imrt treatment plans* Int. J. Radiation Oncology Biol. Phys.,, 2005. **63**(2): p. 422-433.

154. *Geometric Uncertainties in Radiotherapy. Defining the Planning.* The Bristish Institute of Radiology, 2003. **Target Volume**.

155. Radcliffe T, Rajapakshe R, and S. S, *Pseudocorrection: a fast, robust, absolute, grey-level image alignmentalgorithm.* Med. Phys, 1994. **21**(761-769).

156. Li, W., et al., *Accuracy of automatic couch corrections with on-line volumetric imaging.* 2009. Vol. 10. 2009.

157. Siebers. Jeffery V., J.O.K., Lung Ko, and Paul J. Keall,, *Monte Carlo computation of dosimetric amorphous silicon electronic portal images.* Medical Physics, 2004. **31**(7): p. 2135-2146.

158. De Vlamynck, K., H Palmans., F. Verhaegen., C. De Wagter., W. De Neve., H. Thierens, *Dose measurements compared with Monte Carlo simulations of narrow 6 MV multileaf collimator shaped photon beams.* Medical Physics, 1999. **26**(9): p. 1874-1882.

159. Daryoush Sheikh-Bagheri, D., D. W. O. Rogers., Carl K. Ross., and Jan P. Seuntjens, *Comparison of measured and Monte Carlo calculated dose distributions from the NRC linac.* Medical Physics, 2000. **27**(10): p. 2256-2266.

160. Mullins, J.P., and Michael G. Herman *Systematic offset of kV and MV localization systems as a function of gantry angle.* Department of Radiation Oncology, Division of Medical Physics, Mayo Clinic, Rochester, MN 55905, USA 2010. **12**(1).

References

161.   Mhatre V, P.P., Dandekar P *Sensitivity of ArcCheck system to setup error using Perfect Pitch 6D couch.*, in *ESTRO*. 2016.